DESIGN OF A NEUTRON CALIBRATION SOURCE FOR THE SNO+ EXPERIMENT

by

Ingrida Semenec

A thesis submitted in partial fulfillment
of the requirements for the degree of
Master of Science in Physics

The Faculty of Graduate Studies
Laurentian University
Sudbury, Ontario, Canada

THESIS DEFENCE COMMITTEE/COMITÉ DE SOUTENANCE DE THÈSE
Laurentian Université/Université Laurentienne
Faculty of Graduate Studies/Faculté des études supérieures

Title of Thesis
Titre de la thèse: DESIGN OF A NEUTRON CALIBRATION SOURCE FOR THE SNO+ EXPERIMENT

Name of Candidate
Nom du candidat: Semenec, Ingrida

Degree
Diplôme: Master of Science

Department/Program
Département/Programme: Physics

Date of Defence
Date de la soutenance November 13, 2017

APPROVED/APPROUVÉ

Thesis Examiners/Examinateurs de thèse:

Dr. Christine Kraus
(Supervisor/Directeur(trice) de thèse)

Dr. Clarence Virtue
(Committee member/Membre du comité)

Dr. Erica Caden
(Committee member/Membre du comité)

Dr. Mark Boulay
(External Examiner/Examinateur externe)

Approved for the Faculty of Graduate Studies
Approuvé pour la Faculté des études supérieures
Dr. David Lesbarrères
Monsieur David Lesbarrères
Dean, Faculty of Graduate Studies
Doyen, Faculté des études supérieures

ACCESSIBILITY CLAUSE AND PERMISSION TO USE

Abstract

SNO+ is a multipurpose detector situated at the SNOLAB facility located at Creighton mine 2 km deep. The SNO+ experiment will have three phases: water, pure scintillator and Te-loaded scintillator. With the detector filled with scintillator, solar neutrinos, geo and reactor anti-neutrinos, and supernova neutrinos can be studied. To analyze the data collected by the detector, it is important to have detailed knowledge of the detector response. This is why calibration is a crucial part of the experiment. The detector response to neutrons will allow us to study the anti-neutrino flux coming from reactors in Canada. Anti-neutrinos can be detected via the inverse beta decay reaction which can be tagged using the neutrons it produces.

This thesis will discuss the radioactive calibration source Americium Beryllium (AmBe) which produces neutrons and gammas. The existing AmBe source - inherited from the SNO experiment - that will be used in water phase has to be modified for the scintillator and loaded scintillator phases. Simulations were carried out to determine the optimal additional shielding required for the scintillator phase. The optimal shielding was determined to be 2 mm of lead surrounded by 1 mm of stainless steel for the encapsulation. The new design for the AmBe source was finalised. The estimated neutron capture event detection efficiency is 74.22%. The analysis of the source deployment at various positions within the detector and the shadowing effects are discussed as well.

Acknowledgments

First and foremost, I would like to thank my supervisor, Dr. Christine Kraus for accepting me into her group and giving me this opportunity to work on one of the most amazing experiments in the world, SNO+. Additionally, I would like to thank my committee members Dr. Erica Caden and Dr. Clarence Virtue for all of the constructive advice and for setting a work standard of high quality, which shaped me into a better physicist.

I would also like to extend my gratitude to all the amazing people at SNOLAB and in the SNO+ collaboration. I truly felt like part of a community, which was uplifting and encouraging. I am particularly grateful for Dr. Christopher Grant's assistance. Your prompt answers to my questions and enthusiastic conversations about various physics topics kept me motivated.

In my daily Canadian life, I have been blessed by an amazing group of friends, who always stood by my side. A huge thank you goes to my BNF Steve, to Caitlyn, Janet, Colin, Chris, Rachel, Pooja, Matt and Jaz for being part of some amazing adventures and board game nights. I'd also like to thank Stephane Venne, my soulmate. Thank you for always being there for me, even if it is 5am in a hospital emergency room.

I cannot forget to thank my best friend, Christopher Woodhead. Your kind heart always restores my faith in humanity.

Finally, I'd like to thank the most important person in my life, my mother, Lolita Semenec.

Ačiū mama už tai, kad per pastaruosius metus tu man parodei, kokia stipri gali būti moters dvasia. Noriu tau padėkoti už tai kad myli mane ir tiki manimi. Myliu tave.

Contents

List of Figures

List of Tables

Chapter 1

Physics

1.1 The brief history of the neutrino

While investigating radioactive beta decay of ^{14}N and ^{6}Li, Wolfgang Pauli noticed that energy was missing from the outgoing electron. What he observed was a continuous spectrum of electron energies, which violated the conservation of energy. Two body decay implies a fixed energy line for electrons. The fact that the measured spectrum was continuous suggested that part of the energy was carried out by a third particle. As a desperate remedy, Pauli penned a letter to physicists in Germany on December 4, 1930. In this letter he proposed the existence of a neutral, spin 1/2 particle also emitted in beta decay [1].

This sparked the interest of Enrico Fermi, who later named the particle "neutrino", meaning "neutral little one" [2]. Around this time, Fermi had developed the theory of beta decay. In his theory the principles of relativity were applied to the creation of particles and anti-particles in the following fashion:

$$(Z, A) \rightarrow (Z + 1, A) + e^{-} + \bar{\nu}_e \tag{1.1}$$

$$(Z, A) \rightarrow (Z - 1, A) + e^{+} + \nu_e \tag{1.2}$$

Equation 1.1 and Equation 1.2 represent what are called "beta minus decay" and "beta plus decay", respectively.

In 1953, two determined physicists Frederic Reines and Clyde Cowan started making plans to detect the neutrino. Their first proposal was to use a nuclear bomb as a neutrino source, but after careful consideration they decided on a nuclear reactor instead. In 1959, they built a detector 12 m underground near a nuclear reactor in Savannah River, South Carolina. The detector consisted of two tanks filled with $\approx$ 400 liters of water loaded with 40 kg cadmium chloride, used as a target material. The antineutrino created inside the nuclear reactor interacted with a proton in the target material, giving a positron and neutron, shown in Figure 1.1. The prompt light signal created from positron annihilation and the delayed signal from neutron capture on cadmium was observed by 55 photomultiplier tubes (PMTs). This was a first measurement of a free neutrino event [3]. This result was awarded Nobel Prize 40 years later in 1995 [4].

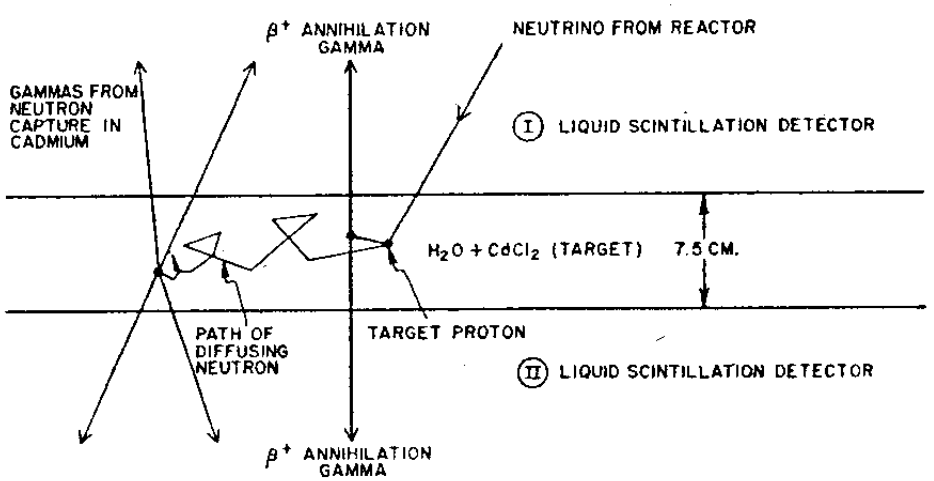

Figure 1.1: The schematic diagram of neutrino detector by Frederivc Reines and Clyde Cowan [5].

1.2 Neutrinos in the Standard Model of Particle Physics

The Standard Model of Particle Physics (SM) (Figure 1.2) gives a description of the electromagnetic, weak and strong interactions between the known elementary particles. It consists of the basic components of matter (quarks and leptons) and the force carriers (bosons). Quarks and leptons are fermions with spin 1/2 and are classified into three distinct families (flavours). In the original formulation of the SM, neutrinos are massless. Leptons are described as SU(2) weak-isospin doublets consisting of a neutrino and its flavour-coupled charged lepton partner. Weak-isospin is a

quantum number, that relates to weak interaction and SU(2) represents the weak isospin symmetry group. It is assumed that the neutrino fields contained in these doublets are left-handed chirality. The right-handed components of the other leptons are represented as singlets in the hypercharge symmetry group U(1). Each left-handed doublet is accompanied by a right-handed charged singlet. The left-handed doublets and right-handed singlets form the basis of the symmetry group SU(2)×U(1), which describes the electroweak interactions of neutrinos. That shows that weak interactions couple only to ν_{L} and $\bar{\nu}_{\mathrm{R}}$.

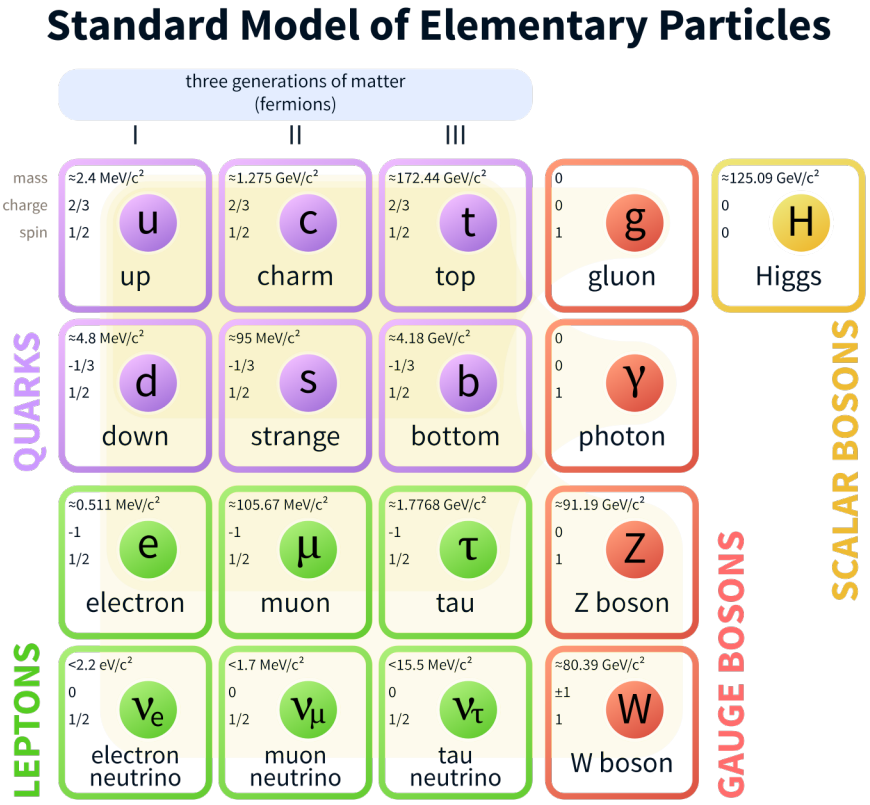

Figure 1.2: The illustration of the basic components of the standard model [6].

Of the three flavours of neutrinos, the electron flavour was detected by Reines and Cowan. The muon flavour was discovered by Melvin Schwartz, Leon Lederman and Jack Steinberger using the Alternating Gradient Synchrotron (AGS) at Brookhaven National Laboratory in 1962 [7]. They collided protons onto a Beryllium target to produce pions. Then they looked for decay into muons and muon neutrinos:

$$\pi^{\pm} \rightarrow \mu^{\pm} + (\nu/\bar{\nu}) \tag{1.3}$$

Then the resulting neutrino beam hit a thick iron shield wall at a distance of 21 m from the Beryllium target. Behind the iron shield there was a 10 t aluminium spark chamber, which observed neutrino interactions. Detailed cross sections were calculated for the following interactions:

$$\nu_{\mu} + n \rightarrow e^{-} + p \tag{1.4}$$

$$\bar{\nu}_{\mu} + p \rightarrow e^{+} + n \tag{1.5}$$

$$\nu_{\mu} + n \rightarrow \mu^{-} + p \tag{1.6}$$

$$\bar{\nu}_{\mu} + p \rightarrow \mu^{+} + n \tag{1.7}$$

$$\tag{1.8}$$

If neutrinos associated with muons are the same as with electrons, then neutrino interactions should produce muons and electrons in equal abundance. However, they have observed 34 single muon events and only 6 electron showers. Furthermore, these electron events are more consistent with the expected background. This determined that the muon neutrino is a separate particle from the electron neutrino.

A while after in 2000 the tau neutrino (ν_{τ}) was discovered by the DONUT experiment at Fermilab [8]. It was predicted for the conservation of the lepton number during tau decays. Because lepton number is additive quantum number, the sum of leptons and antileptons must be preserved in interactions. The DONUT experiment observed charged current interactions of the ν_{τ} by looking for τ lepton to be created at the neutrino interaction vertex. They used an accelerated proton beam to produce ν_{τ} via decay of charmed mesons. In the set of 203 neutrino interactions, they observed four τ lepton inetractions. The probability that those four events came from the background was estimated to be 4×10^{-4}, which concluded that ν_{τ} events were observed [8].

1.2.1 Neutrinoless double beta decay

Neutrinoless double beta decay ($\beta\beta0\nu$) is a nuclear transition that occurs if neutrinos are their own antiparticles. The main feature of this decay mode is that it violates lepton number conservation, which is part of the standard model. Another possible transition is two-neutrino double beta decay ($\beta\beta2\nu$) which does not violate the number of leptons and occurs whether or not neutrinos are their own antiparticles.

Figure 1.3 shows the Feynman diagrams of both of these transitions.

$$\beta\beta0\nu : (Z, A) \rightarrow (Z + 2, A) + e_1^- + e_2^- \qquad \Delta\mathrm{L} = 2$$

$$\beta\beta2\nu : (Z, A) \rightarrow (Z + 2, A) + e_1^- + e_2^- + 2\bar{\nu}_e \qquad \Delta\mathrm{L} = 0$$

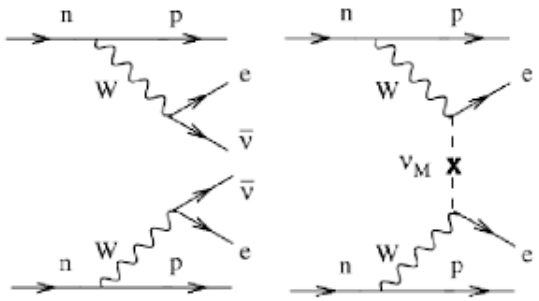

Figure 1.3: Feynman diagrams for $\beta\beta2\nu$ (left) and $\beta\beta0\nu$ (right).[9]

Double beta decay was proposed in 1935 by Maria Goepper-Mayer [10]. She derived the expression for the decay $(Z, A) \rightarrow (Z + 2, A) + e_1^- + e_2^- + 2\bar{\nu}_e$ and estimated the halflife to be 10^{17} years. Two years later a theory where neutrinos are their own antiparticles was formulated by Ettore Majorana [11]. A way to test Majorana's theory, through the observation of neutrinoless double beta decay mode, was proposed by Wendell H Furry in 1939 [12].

Observation of the neutrinoless double beta decay implies that instead of a normal decay the nucleons exchange a virtual neutrino. This violates lepton number conservation by two units $\Delta L = 2$. Lepton number violation implies that the lepton number is not symmetrical, which could explain the matter-antimatter asymmetry in the universe. If the neutrino is a Majorana particle, neutrinos and antineutrinos are the same. This would imply that it is possible for matter to

transform to antimatter and vice-versa, thus creating an imbalance between matter and antimatter in the early universe. This effect is also known as "leptogenesis".

The neutrino being a Majorana particle could lead to determining the absolute mass of the neutrino. If neutrinos are Majorana particles, that implies two additional Majorana phases responsible for lepton number violating processes such as neutrinoless double beta decay. The effective Majorana neutrino mass from neutrinoless double beta decay depends on these phases, which then can cause cancellations among the contributions of the neutrino masses [13]. The effective majorana mass in $\beta\beta0\nu$ decay can be written as Equation 1.9 [14], using the Pontecorvo-Maki-Nakagawa-Sakata matrix Equation 1.17, which will be discussed in detail in Section 1.3.

$$|m_{\beta\beta}| = |c_{13}^2 c_{12}^2 e^{2i\alpha_1} m_1 + c_{13}^2 s_{12}^2 e^{2i\alpha_2} m_2 + s_{13}^2 m_3| \tag{1.9}$$

Therefore, if neutrinoless double beta decay is detected it is possible to compute the absolute mass for neutrinos by taking into account the already known experimental values of neutrino mass splittings provided by neutrino oscillation measurements and combining it with the results of the lowest neutrino mass.

1.3 Neutrino oscillations

The solar neutrino experiments revealed the phenomenon of the adiabatic flavour conversion of neutrinos in the sun. This led to the discovery of neutrino oscillations. The Homestake experiment was the experiment led by astrophysicist Raymond Davis, who used the theoretical calculations made by John N. Bahcall in the late 1960s [15]. The purpose of this experiment was to detect neutrinos emitted by nuclear fusion reactions in the Sun. The detector was located 1.5 km underground. As a target the 6 m diameter and 15 m long tank held about 400 tons of perchloroethylene. The experiment involved neutrino capture on chlorine to form argon (Equation 1.10) which has good cross section for observation of neutrinos coming from ^{7}Be, ^{13}N and ^{15}O decays and the proton-proton (p-p) reaction [16].

$$\nu + {}^{37}\mathrm{Cl} \underset{decay}{\overset{capture}{\rightleftharpoons}} {}^{37}\mathrm{Ar} + e^- \tag{1.10}$$

Even though the Homestake experiment was first to detect solar neutrinos, the measured rate

of the neutrinos was only one third of what was expected from the solar models at the time. This raised many speculations and questions about the quality of the experiment and the theoretical predictions. This deficit in neutrino signal was also called the solar neutrino problem.

The Homestake experiment was then followed by others: Kamiokande, GALLEX and SAGE. Kamiokande used a large water Cherenkov detector and looked for neutrino scattering with an electron [17]. While SAGE and GALLEX looked at $^{71}\mathrm{Ga}(\nu_e, e)^{71}\mathrm{Ge}$ reaction in gallium. SAGE used 50-57 tonnes of liquid gallium as a target for the reaction at the Baksan Neutrino Observatory in Caucasus mountains. GALLEX was another large gallium-germanium experiment. It used 101 t of gallium trichloride-hydrochloric acid solution, which also contained 30.3 t of gallium and was located in the Laboratori Nazionali del Gran Sasso in Italy [18]. The Figure 1.4 shows that all of the following experiments have seen the deficit in the rate of solar neutrinos compared to the standard solar model predictions. Important to note that the deficit is different for different ranges of solar neutrinos. This could be explained by the Mikheyev-Smirnov-Wolfenstein (MSW) effect, discussed in greater detail in subsection 1.3.1.

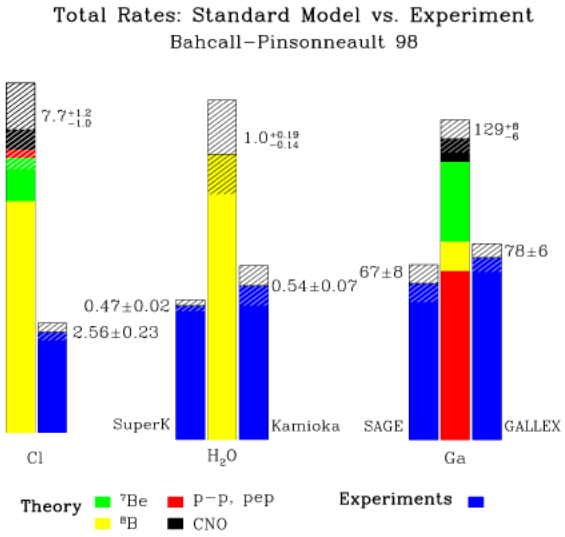

Figure 1.4: The comparison between the predictions of the standard solar model with the measured rates in the solar neutrino experiments [19].

Bruno Pontecorvo postulated that if neutrinos have mass, then it would be possible for neutrinos to oscillate between states [20]. In the paper both $\nu \rightleftharpoons \overline{\nu}$ and $\nu_e \rightleftharpoons \nu_\mu$ oscillations were mentioned. Robert Ehrlich suggested that Pontecorvo's theory could solve the solar neutrino problem. If it

was possible for ν_e and ν_μ to oscillate between themselves, a fraction of electron neutrinos coming from the sun would transform into muon or even tau neutrinos, before they get detected on Earth. This could explain why while detecting electron neutrinos, fewer of them are seen than expected [21].

On June 18, 2001 Sudbury Neutrino Observatory (SNO, subsection 2.1.1) announced their first solar neutrino results that solved the solar neutrino mystery [22]. SNO used 1000 tonnes of heavy water (D_2O) to study higher energy solar neutrinos than the SAGE or GALLEX experiments. The electron neutrino measurements from SNO were compared to the ones from Super-Kamiokande [17]. According to the theory at the time, the measured fractions should have been the same for the same type of neutrino. However, the fractions were different. This implied that the theoretical models were incorrect. SNO was sensitive to not only charged current (CC, Equation 1.12), but also neutral current (NC, Equation 1.13) interactions and elastic scattering (ES, Equation 1.11), which can provide information about other flavours of neutrinos.

$$\text{ES:} \quad \nu_{e,\mu,\tau} + e^- \rightarrow \nu_{e,\mu,\tau} + e^- \tag{1.11}$$

$$\text{CC:} \quad \nu_e + d \rightarrow e^- + p + p \tag{1.12}$$

$$\text{NC:} \quad \nu_{e,\mu,\tau} + d \rightarrow \nu_{e,\mu,\tau} + n + p \tag{1.13}$$

The combined measurements from SNO and the Super-Kamiokande determined the total flux of solar neutrinos of all types. The number for the total flux agreed with the standard solar model. This proved that the missing neutrino signal was not actually missing. It showed that the rest of the flux was muon and tau neutrinos, which were not detected by the previous experiments. The SNO experiment determined the ratio between CC and NC rates [23]:

$$\frac{\phi_{CC}^{SNO}}{\phi_{NC}^{SNO}} = 0.301 \pm 0.033 \tag{1.14}$$

About two thirds of the electron neutrinos oscillate or change into other flavours by the time they are detected, Equation 1.14. Even though the adiabatic change in flavour observed by SNO is due to the MSW effect (subsection 1.3.1), these combined results from SNO and Super-Kamiokande

provided proof for the Pontecorvo theory about neutrino oscillations.

Neutrino oscillations can be described using quantum mechanical superposition of states. Every flavour eigenstate is superposition of mass eigenstates (Equation 1.15). In other words, every neutrino is a superposition of all three neutrino flavours. In Equation 1.15 the $|\nu_\alpha\rangle$ is a flavour state (where $\alpha = e,\mu,\tau$), the $U^*_{\alpha k}$ is the weight term from unitary mixing matrix and the $|\nu_k\rangle$ ($k = 1,2,3$) is the mass state. The flavour and mass states are orthonormal, Equation 1.16.

$$|\nu_\alpha\rangle = \sum_k U^*_{\alpha k}|\nu_k\rangle \tag{1.15}$$

$$\langle\nu_k|\nu_j\rangle = \delta_{kj}, \quad \langle\nu_\alpha|\nu_\beta\rangle = \delta_{\alpha\beta} \tag{1.16}$$

The mixing between different eigenbases can be described using the Pontecorvo-Maki-Nakagawa-Sakata (PMNS) matrix (Equation 1.17). The PNMS matrix is a representation of a $SO(3)$ group of unitary rotations in space using Euler angles. It can be described by three Euler angles between each combination of mass eigenstates $\theta_{12}, \theta_{23}, \theta_{13}$, the Dirac CP-phase (charge conjugation and parity), δ. If non-zero, this would confirm the CP-violation for leptons. The Majorana phase would imply that neutrinos are their own antiparticle, thus interactions could have occured making more matter than antimatter in the early universe.

$$U = \begin{pmatrix} U_{e1} & U_{e2} & U_{e3} \\ U_{\mu 1} & U_{\mu 2} & U_{\mu 3} \\ U_{\tau 1} & U_{\tau 2} & U_{\tau 3} \end{pmatrix} \tag{1.17}$$

$$= \begin{pmatrix} 1 & 0 & 0 \\ 0 & c_{23} & s_{23} \\ 0 & -s_{23} & c_{23} \end{pmatrix} \begin{pmatrix} c_{13} & 0 & s_{13}e^{-i\delta} \\ 0 & 1 & 0 \\ -s_{13}e^{i\delta} & 0 & c_{13} \end{pmatrix} \begin{pmatrix} c_{12} & s_{12} & 0 \\ -s_{12} & c_{12} & 0 \\ 0 & 0 & 1 \end{pmatrix} \tag{1.18}$$

$$\text{where} \quad U^\dagger U = \mathbb{1} \quad \text{and} \quad c_{ij} = cos\theta_{ij}, \quad s_{ij} = sin\theta_{ij} \tag{1.19}$$

The neutrino flavour eigenstates are used to describe weak interactions, however the mass eigenstates propagate through space via the Schrödinger equation (Equation 1.20) with eigenvalues

$E_k = \sqrt{\vec{p}^2 + m_k^2}$.

$$H|\nu_\alpha\rangle = E_k|\nu_k\rangle \tag{1.20}$$

To see how neutrino flavour changes over time we need to solve the time-dependent Schrödinger equation (Equation 1.21) using a plane wave solution (Equation 1.22).

$$i\frac{\mathrm{d}}{\mathrm{d}t}|\nu_k(t)\rangle = H|\nu_k(t)\rangle \tag{1.21}$$

$$|\nu_k(t)\rangle = e^{-iE_k t}|\nu_k\rangle \tag{1.22}$$

$$\implies |\nu_\alpha(t)\rangle = \sum_k U^*_{\alpha k} e^{-iE_k t}|\nu_k\rangle \tag{1.23}$$

Equation 1.23 shows the evolution of flavour states in terms of mass states. However we want to know the change of flavour states in terms of other flavour states. Therefore the mass state can be written as superposition of flavour states $|\nu_k\rangle = \sum_\beta U_{\beta k}|\nu_\beta\rangle$ and substituted back to Equation 1.23.

$$|\nu_\alpha(t)\rangle = \sum_{\beta,k} U^*_{\alpha k} e^{-iE_k t} U_{\beta k}|\nu_\beta\rangle \tag{1.24}$$

The amplitude (Equation 1.26) is then used to calculate the transition probability (Equation 1.27).

$$P_{\nu_\alpha \to \nu_\beta} = |A_{\nu_\alpha \to \nu_\beta}(t)|^2 \tag{1.25}$$

$$A_{\nu_\alpha \to \nu_\beta}(t) \equiv \langle \nu_\beta|\nu_\alpha(t)\rangle = \sum_k U^*_{\alpha k} U_{\beta k} e^{-iE_k t} \tag{1.26}$$

$$\implies P_{\nu_\alpha \to \nu_\beta} = \sum_{k,j} U^*_{\alpha k} U_{\beta k} U_{\alpha j} U^*_{\beta j} e^{-i(E_k - E_j)t} \tag{1.27}$$

Now from the relativistic equation $E^2 = m^2 + p^2$, because neutrinos are ultra-relativistic $E = |\vec{p}|$:

$$p = \sqrt{E^2 - m_k^2} = E\sqrt{1 - \frac{m_k^2}{E^2}} \approx E - \frac{m_k^2}{2E} \tag{1.28}$$

$$\implies E_k - E_j = \frac{(m_k^2 - m_k^2)}{2E} = \frac{\Delta m_{kj}^2}{2E} \tag{1.29}$$

Substituting Equation 1.29 to Equation 1.27 and $t \simeq L$, where L is the distance from the source to the detector, gives Equation 1.30 which then can be applied to two or three flavour oscillation case.

$$P_{\nu_\alpha \to \nu_\beta} = \sum_{k,j} U_{\alpha k}^* U_{\beta k} U_{\alpha j} U_{\beta j}^* e^{-i\frac{\Delta m_{kj}^2 L}{2E}} \tag{1.30}$$

For the simple two flavour case can use the simple rotational matrix, Equation 1.31:

$$\begin{pmatrix} \nu_\alpha \\ \nu_\beta \end{pmatrix} = \begin{pmatrix} \cos\theta & \sin\theta \\ -\sin\theta & \cos\theta \end{pmatrix} \begin{pmatrix} \nu_1 \\ \nu_2 \end{pmatrix} \tag{1.31}$$

Then from the Equation 1.31 we can find the time evolution of flavour state from Hamiltonian:

$$|\nu_\alpha(t)\rangle = \cos\theta e^{-iE_1 t}|\nu_1\rangle + \sin\theta e^{-iE_2 t}|\nu_2\rangle \tag{1.32}$$

$$\text{,where} \quad |\nu_1\rangle = \cos\theta|\nu_\alpha\rangle - \sin\theta|\nu_\beta\rangle \tag{1.33}$$

$$|\nu_2\rangle = \sin\theta|\nu_\alpha\rangle + \cos\theta|\nu_\beta\rangle \tag{1.34}$$

$$\tag{1.35}$$

After some manipulation the flavour states in terms of flavour and not mass states can be expressed as:

$$|\nu_\alpha(t)\rangle = (\cos^2\theta e^{-iE_1 t} + \sin^2\theta e^{-iE_2 t})|\nu_\alpha\rangle - \cos\theta\sin\theta(e^{-iE_1} - e^{-iE_2 t})|\nu_\beta\rangle \tag{1.36}$$

Substituting back to Equation 1.27:

$$P_{\nu_\alpha \to \nu_\beta}(t) = |\langle \nu_\beta | \nu_\alpha(t) \rangle|^2 \tag{1.37}$$

$$= (\cos\theta \sin\theta)^2 (e^{-iE_2 t} - e^{-iE_1 t})(e^{iE_2} - e^{iE_1 t}) \tag{1.38}$$

$$= \left(\frac{\sin 2\theta}{2}\right)^2 (1 - e^{i(E_2 - E_1)t} - e^{-i(E_2 - E_1)t} + 1) \tag{1.39}$$

$$= \frac{\sin^2 2\theta}{4}(2 - 2cos((e_2 - E_1))t) \tag{1.40}$$

$$= \sin^2 2\theta \sin^2\left(\frac{E_2 - E_1}{2} t\right) \tag{1.41}$$

$$\implies P_{\nu_\alpha \to \nu_\beta} = \sin^2 2\theta \sin^2\left(\frac{\Delta m^2_{21}}{4E} L\right) \tag{1.42}$$

Equation 1.42 is the probability that the neutrino oscillated into another flavour, for two flavour case. However, this 2 flavour probability is only a good approximation to the exact probability, because all three flavours should be considered. Equation 1.43 shows the conventional case using SI units with L in km, E in GeV and the mass squared difference in eV^2, which is more convenient to use during an experiment.

$$P_{\nu_\alpha \to \nu_\beta} = \sin^2 2\theta \sin^2\left(1.27 \frac{\Delta m^2 L}{E} \frac{[\text{eV}^2][\text{km}]}{[\text{GeV}]}\right) \tag{1.43}$$

Figure 1.5 compares the constraints on the Δm^2_{21} and $\sin^2\theta_{12}$ oscillation parameters. The SNO measurement of the mixing angle $\left(\sin^2\theta_{12} = 0.299^{+0.023}_{-0.020}\right)$ are more precise than Super Kamiokande $\left(\sin^2\theta_{12} = 0.334^{+0.027}_{-0.023}\right)$. However, the Δm^2_{21} constraints are worse for SNO $\left(\Delta m^2_{21} = 5.6^{+1.9}_{-1.4} \times 10^{-5}\text{eV}^2\right)$ compared to Super Kamiokande's $\left(\Delta m^2_{21} = 4.8^{+1.5}_{-0.8} \times 10^{-5}\text{eV}^2\right)$ [24]. The SNO+ is sensitive to measuring reactor neutrinos (further discussed on subsection 1.5.1). SNO+ is expected to provide independent measurement of Δm^2_{21} with sensitivity of $0.2 \times 10^{-5}\text{eV}^2$, in about 7 years worth of data [25].

The Figure 1.6 illustrates the survival probability of $\bar{\nu}_e$ dependence on the distance L form the reactor for E_ν =3 MeV.

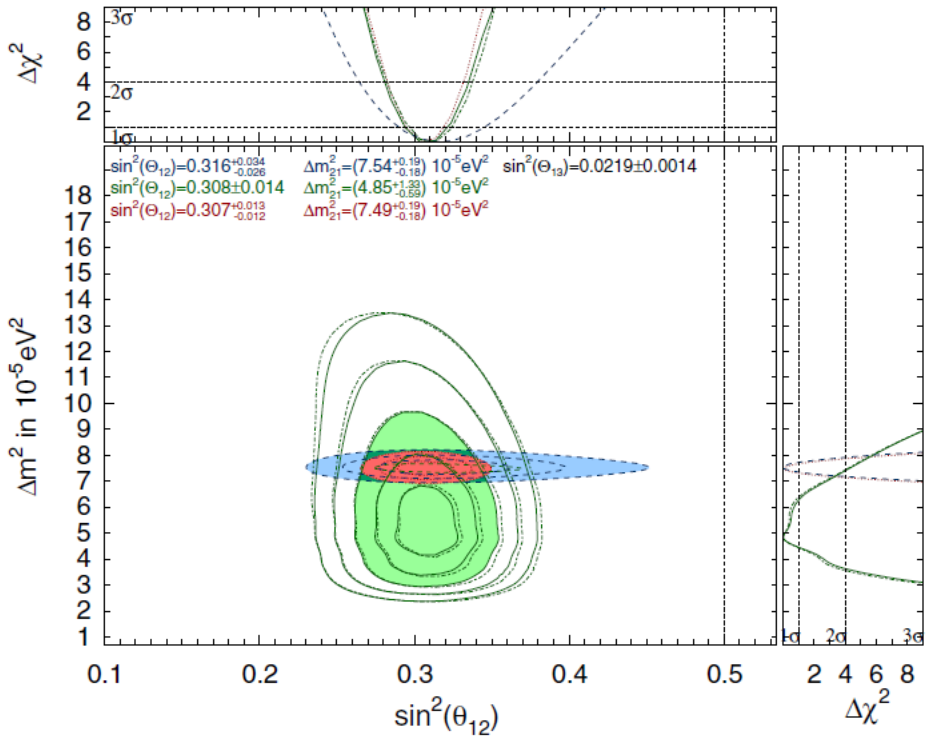

Figure 1.5: The confidence regions of the $\sin^2\theta_{12}$ and Δm^2_{21} measurements from Super-K, SNO and KamLAND experiments. The regions and values are marked as follows: KamLAND in blue, combined SK+SNO+KamLAND in red and combined SK+SNO in green [24].

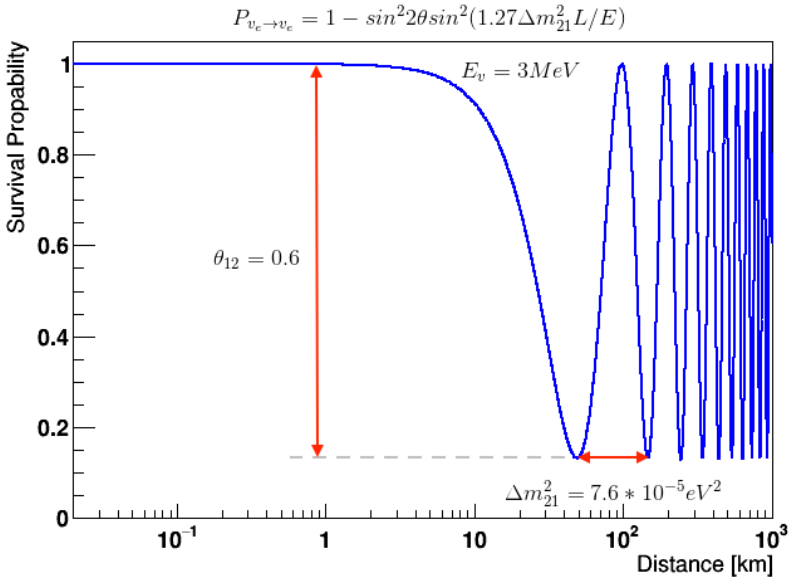

Figure 1.6: The reactor $\bar{\nu}_e$ survival probability versus the distance from the reactor for the $E_\nu = 3$ MeV.

1.3.1 The MSW effect

The flavour specific neutrino interactions must be taken into account when considering neutrino propagation through matter. In general all neutrinos may interact with matter via charged current (CC) or neutral current (NC) interactions. In addition to NC interactions via Z bosons, the electron neutrinos at solar neutrino energies interact through CC channel via W bosons, whereas muon and tau neutrinos are bellow energy threshold for CC interactions. Therefore electron neutrinos experience an additional potential energy $V_{CC} = \sqrt{2}G_F N_e$, where N_e is the electron density in matter and $G_F = 1.166 \times 10^{-5}\text{GeV}^{-2}$ is the Fermi constant. Because the effect of NC interactions with matter is equal for all types of neutrino it only adds a certain constant to the oscillations.

The neutrino oscillation in matter derivation is shown in Appendix A. The new matter neutrino oscillation parameters get defined as Δm^2_M and $\sin^2 2\theta_M$ in terms of Δm^2 and $\sin^2 2\theta$ from Equation 1.42, as shown in Equation 1.44 and Equation 1.45 respectively, where $A_{CC} = 2\sqrt{2}G_F N_e E/\Delta m^2_{21}$.

$$\Delta m^2_M \equiv \Delta m^2_{21}\sqrt{\sin^2 2\theta + (\cos 2\theta - A_{CC})^2} \tag{1.44}$$

$$\sin^2 2\theta_M \equiv \frac{\sin^2 2\theta}{\sin^2 2\theta + (\cos 2\theta - A_{CC})^2} \tag{1.45}$$

Then the oscillation probability in matter becomes:

$$P^M_{\nu_\alpha \to \nu_\beta} = \sin^2 2\theta_M \sin^2\left(\frac{\Delta m^2_M}{4E} L\right) \tag{1.46}$$

After the measurement the materials that neutrinos passed through must be taken into account to correct the measured mass difference and mixing angles. Looking at Equation 1.45 it is visible that, if $A_{CC} = \cos 2\theta$, then $\sin^2 2\theta_M = 1$ and $\theta_M = 45\,\text{deg}$, the mixing matter can be maximal. This specific case, when the electron density and neutrino energy are at the right values for the maximum mixing is called Mikheyev-Smirnov-Wolfenstein (MSW) effect.

1.4 Neutrino mass

The Section 1.3 showed that neutrino oscillations have dependence on neutrino mass. Even though the absolute mass of the lightest neutrino is still unknown, the mass-squared differences can be extrapolated from the neutrino osccillation experiments. These allow two possible arrangements of different mass levels (Figure 1.7). The normal hierarchy, where $m_1 \ll m_2 \ll m_3$, would mean that $\Delta m^2_{23} \equiv m^2_3 - m^2_2 > 0$. For the inverted hierarchy, where $m_1 \simeq m_2 \gg m_3$, solar oscillation is between heavier levels, therefore $\Delta m^2_{23} \equiv m^2_3 - m^2_2 < 0$.

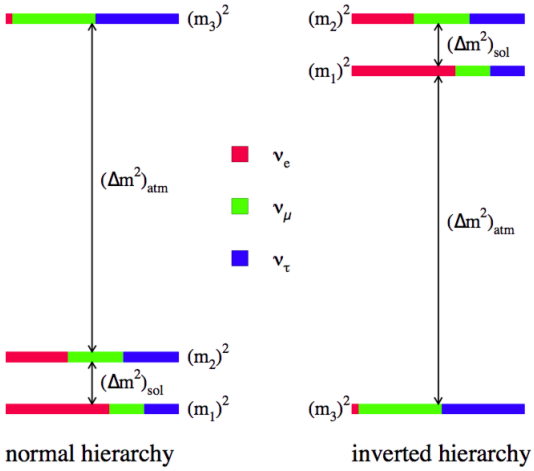

Figure 1.7: The two possible neutrino mass hierarchies [26].

It is important to establish the order of the neutrino mass states. Knowing the mass hierarchy would determine the future of the neutrinoless double beta decay experiments, and would limit the area of interest for the signal of this process. This would help to obtain the absolute mass of neutrinos.

1.5 Anti-neutrino physics

The detection of the electron anti-neutrinos in scintillator plays one of the most crucial roles in the exploration of neutrino physics. Not only does it provide us insight into neutrino oscillation parameters, by measuring reactor neutrinos, but also into astrophysics events such as supernovae, and the interior of the Earth (i.e. geoneutrinos).

Inverse beta decay

Inverse beta decay (Equation 1.47) is the crucial reaction for the detection of reactor anti-neutrinos inside the detector. It is also useful for the detection of supernova neutrinos. Using the angular distribution of the reaction, the directionality of the anti-neutrino source can be posibly distinguished.

$$\bar{\nu}_e + \mathrm{p} \rightarrow \mathrm{n} + \mathrm{e}^+ \tag{1.47}$$

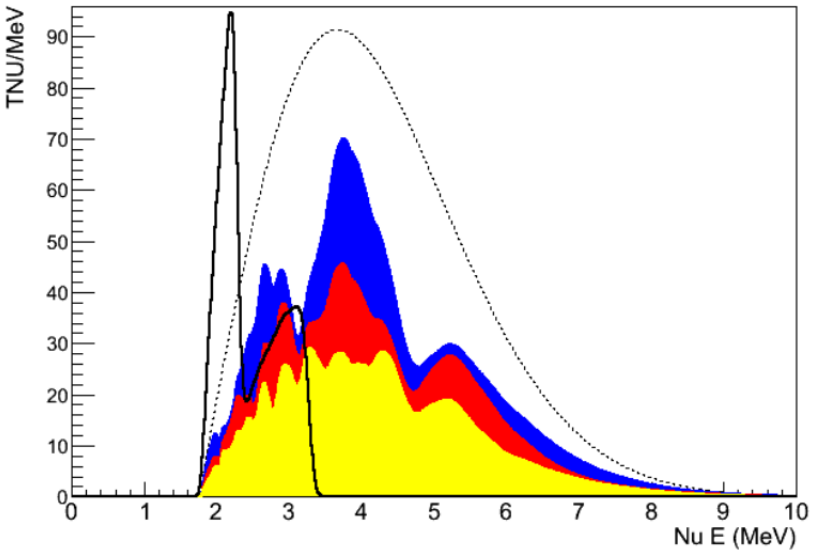

Figure 1.8: The expected anti-neutrino energy spectrum in SNO+ [25]. The geo neutrino spectrum is shown in solid black line. The oscillated reactor neutrino spectrum is shown in colours according to reactors: Bruce (240 km) in blue, Pickering and Darlington (350 km) in red, others in yellow.

The anti-neutrino energy can be reconstructed from the scintillation light emitted by positron annihilation (Equation 1.48).

$$E_{\bar{\nu}_e} \simeq E_{prompt} + (M_n - M_p) - m_e \simeq E_{prompt} + 0.8\,\mathrm{MeV} \tag{1.48}$$

Here M_n, M_p and m_e are the masses of the neutron, proton and electron. The neutron thermalises and gets capured within the scintillator and produces 2.2 MeV gamma capture peak. The prompt positron and delayed neutron capture signal allows us to tag the anti-neutrino event. Even though positron gives us measure of energy, it does not give the information about the track and the direction of the incoming anti-neutrino in the scintilator. In the reaction (Equation 1.47) the

outgoing neutrons tend to be forward-peaked [27]. In other words, the positron, because of being very light, gets scattered more than the much heavier neutron. Therefore the separation between positron and neutron directions can be measured. Understanding the neutron event detection efficiency and reconstruction would lead to better reconstruction of anti-neutrino direction and track. This can be either used for rejecting backgrounds or locating the source of the anti-neutrinos.

1.5.1 Reactor neutrinos

SNO+ is sensitive to the $\bar{\nu}_e$ flux created by fission reactions inside nuclear reactors. The reactors create neutrinos via beta decay of the unstable daughter products of the nuclear reactions. Unlike the other decay products that end up deposited as heat, the anti-neutrinos escape and then can be detected by the SNO+ detector. The flux of electron anti-neutrinos can be accurately calculated because it is closely related to the thermal power of the reactor itself. The energy spectrum can be estimated knowing the composition of nuclear fuel and the way it decays within the reactor. SNO+ expects to see approximately 90 anti-neutrino events per year [25]. 40% comes from a reactor complex 240 km away from the detector, 20% comes from two other complexes 350 km away, and 40% is total from other reactors elsewhere. The measurement from two different baseline distances will give a clear anti-neutrino oscillation spectrum Figure 1.8.

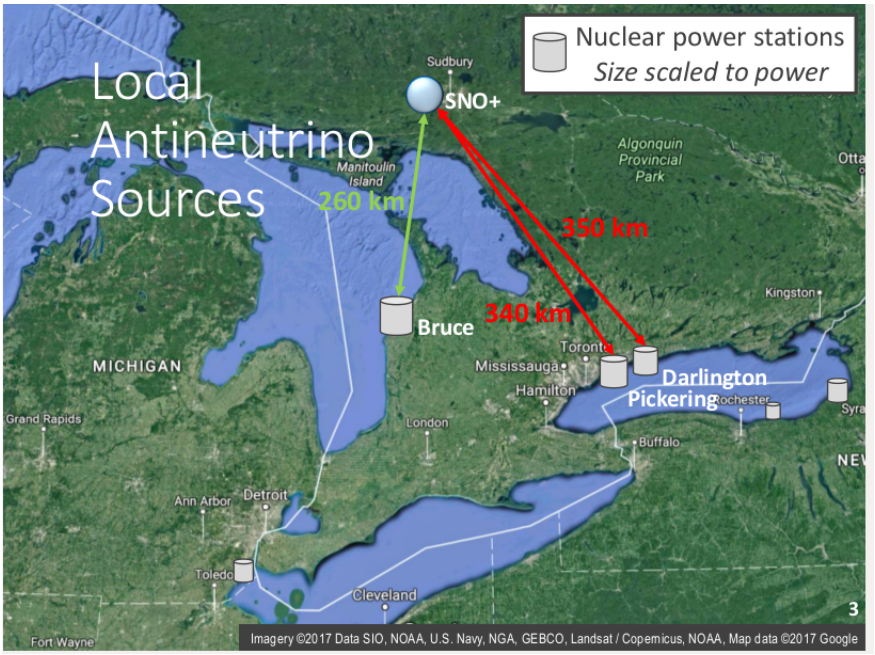

Figure 1.9: The map of nearby nuclear reactors and their distances to SNO+.

Typically 99% of reactor anti-neutrinos are produced by beta decay of unstable daughter fragments: ^{235}U, ^{238}U, ^{239}Pu, ^{241}Pu [28].

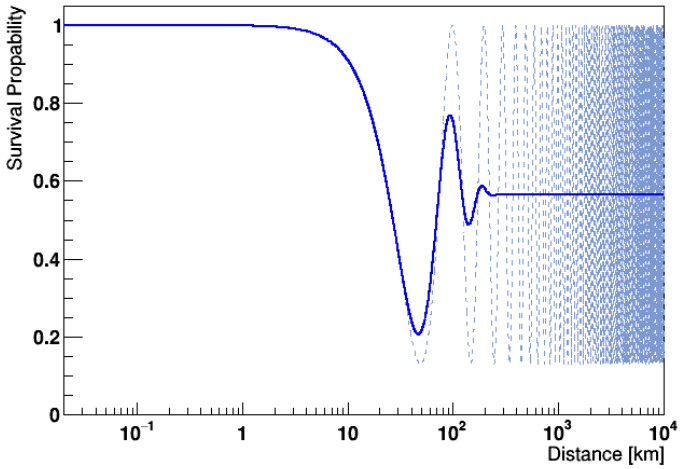

Figure 1.10: The illustration of neutrino oscillation probability smearing due to the finite energy resolution of the detector (blue line). The reactor $\bar{\nu}_e$ survival probability versus the distance from the reactor for the $E_\nu = 3$MeV, as was shown in Figure 1.6.

As seen previously from Figure 1.6, the anti-neutrino oscillation probability depends on the distance of the detector from the reactor and the energy of the anti-neutrino produced. However, the oscillations in survival probability also occur over larger energy intervals than the uncertainty in the energy measurement of the detector. Therefore the energy resolution is a dominant factor in smearing of the neutrino oscillations. The Figure 1.10 demonstrates the way the oscillation spectrum gets smeared in the real life experiments, depending on the distance and also number of surrounding nuclear reactors. Because SNO+ has two distinct close proximity baselines from nearby reactors, such that the second oscillation minimum from Bruce reactor coincides with the third oscillation minimum from Pickering and Darlington reactor oscillation spectra producing a distinctive pattern, as shown in Figure 1.8. SNO+ should be able to see few distinct peaks of the neutrino oscillation ($\approx$ 3.2, 4.8 MeV), coming from oscillation dependence on Δm^2_{12}. This obvious sensitivity to the mass splitting gives SNO+ an oppotunity to measure the oscillation mass parameter to high precision (Figure 1.11).

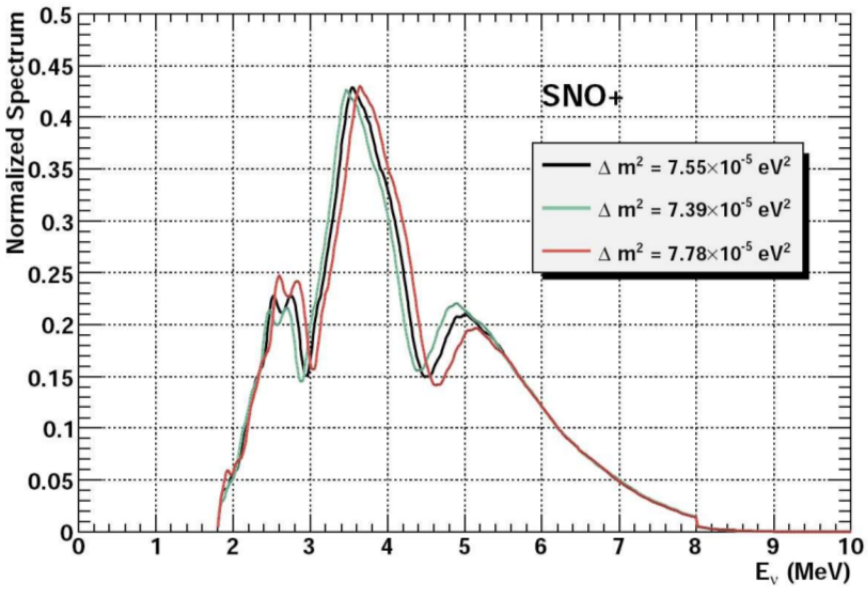

Figure 1.11: The expected spectrum of reactor anti-neutrino signal for different values of Δm^2_{12} for the SNO+ experiment [29].

1.5.2 Geo-neutrinos

The long lived isotopes in the Earth's crust and mantle undergo nuclear decay processes. Each nuclear decay process includes beta decays, which produce electron anti-neutrinos. These electron anti-neutrinos are also called "geo-neutrinos". Figure 1.12 shows a worldwide $\bar{\nu}_e$ flux map combining geoneutrinos from natural ^{238}U and ^{232}Th decays, with the ones emmited from the nuclear reactors around the world [30].

The main heat producing decay chains are:

$$^{238}\mathrm{U} \rightarrow {}^{206}\mathrm{Pb} + 8\alpha + 8e^- + 6\bar{\nu}_e + 51.7 \quad \mathrm{MeV} \tag{1.49}$$

$$^{232}\mathrm{Th} \rightarrow {}^{208}\mathrm{Pb} + 6\alpha + 4e^- + 4\bar{\nu}_e + 42.7 \quad \mathrm{MeV} \tag{1.50}$$

$$^{40}\mathrm{K} \rightarrow {}^{40}\mathrm{Ca} + e^- + \bar{\nu}_e + 1.31 \quad \mathrm{MeV} \tag{1.51}$$

The anti-neutrino spectrum coming from these decays is shown in Figure 1.13. The kinematic threshold for inverse beta decay is 1.806 MeV. Therefore the anti-neutrinos coming from ^{40}K decay chain cannot be detected. However a fraction of geo-neutrinos produced in ^{232}Th and ^{238}U can be detected via the inverse beta decay reaction, shown in Equation 1.47. The energy of geoneutrinos

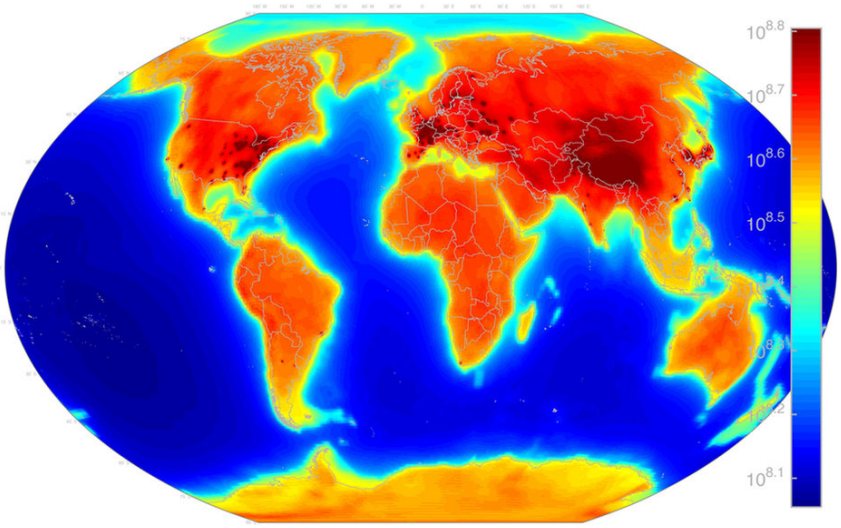

Figure 1.12: A worldwide $\bar{\nu}_e$ flux map combining geoneutrinos from natural ^{238}U and ^{232}Th decays, with the ones emited from the nuclear reactors around the world [30].

ranges up to about 3.3 MeV, and the expected rate is $45.5^{+7.5}_{-6.3}$TNU (Terrestrial Neutrino Unit) [31].

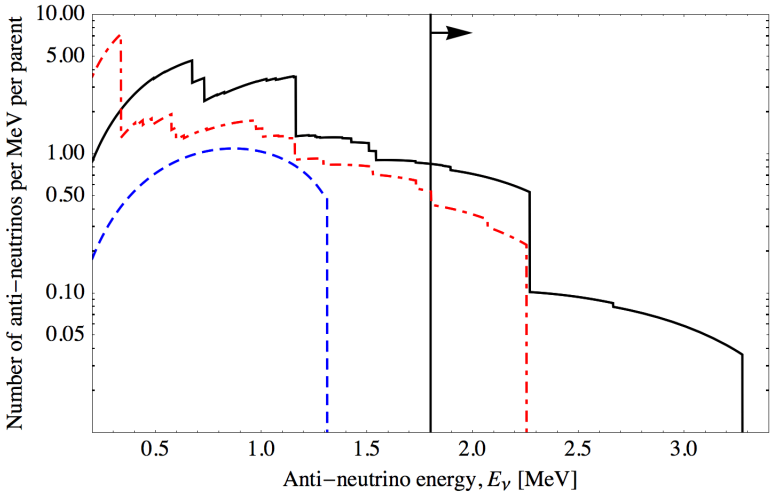

Figure 1.13: The energy spectra of the geo neutrinos produced from the Equation 1.49 (^{238}U chain, solid black line), Equation 1.50 (^{232}Th chain, red dashed-dotted red line) and Equation 1.51 (^{40}K chain, blue dashed blue line). The kinematic threshold of the inverse beta decay is shown as a vertical black line showing the direction of the allowed energies ($\approx$ 1.806 MeV) [32].

The measurement of geo-neutrinos would give insight to the thermal history of the Earth. The mantle is inaccesible to take any direct samples. However, geo-neutrinos can give us information about the chemical composition of deep mantle. It is important to understand the radiogenic heat,

as it contributes to the movement of plate tectonics and relates to the Earth's magnetic field.

1.5.3 Supernova neutrinos

Ever since the observation of the 24 $\bar{\nu}_e$ events from the collapse of supernova SN 1987A, a new interest in neutrino astrophysics was born [33]. For core-collapse supernovae neutrino emission represents $\approx 99\%$ of the gravitational binding energy. Based on SN 1987A events the neutrinos coming from supernova are high energy (12 MeV to 18 MeV). For the $\bar{\nu}_e$ specifically, the mean predicted energy is 15 MeV. However, the predictions are completely model dependent and the energy of neutrinos produced can vary depending on the type of supernova.
The measured relationship between $\bar{\nu}_e$ and other flavours of neutrinos could reveal the pattern of flavour changes. This could shed light to the neutrino mixing parameters and the mass hierarchy. Neutrinos from supernova arrive earlier than light, because neutrinos escape the dense core before photons. Therefore SNO+ will also participate in the Supernova Neutrinos Early Warning System (SNEWS) [34]. SNEWS is an international project of various experiments worldwide that can see the early neutrino signal and and prompt the alert for a supernova event.

This thesis is focused on the SNO+ experiment and the detection of anti-neutrinos using the SNO+ detector. The purpose of this thesis is the design of the AmBe neutron source used for the neutron capture efficiency calibration for the detector in the scintillator phase. The following chapters will discuss the SNO+ detector, calibration systems and the AmBe source design and importance for the success of the experiment. Chapter 2 gives an overview of the SNO+ experiment and the different phases of the experiment for various physics goals. Chapter 3 discusses the detector calibration systems, hardware and optical and radioactive calibration sources. Chapter 4 gives an intoduction to the AmBe neutron source, includes the improvements made to the source design and discusses the new proposed design for the AmBe source for the SNO+ scintillator phase. The new introduced design requires some analysis on shadowing and the deployment simulations with the new and improved source, these are all studied in the Chapter 5. Finally, Chapter 6 summarises the work, establishes the work needed to be done for the successful neutron capture effciency calibration and draws conclusions about the importance of this calibration for the possible anti-neutrino physics data, which would lead to insight on wide range of different neutrino physics topics such as neutrino oscillation parameters, supernova events, and the interior of the Earth.

Chapter 2

The SNO+ experiment

2.1 The SNO+ Detector

SNO+ is a multipurpose scintillator detector located in SNOLAB, a 2070 m underground, 10000 sq ft, Class-2000 clean room in Vale's Creighton mine near Sudbury, Ontario, Canada. The main objective of SNO+ is the search of the neutrinoless double beta decay ($\beta\beta0\nu$) in order to determine if neutrinos are Majorana or Dirac particles and to gain knowledge about the absolute mass of the neutrino. Other topics of interest are reactor neutrino oscillations, supernova neutrinos, geo-neutrinos, and some exotic searches, such as nucleon decay. Given its multipurpose nature, the experiment has three phases. In the first phase, the detector is filled with water. In the second phase, the acrylic vessel is filled with 780 tons of liquid scintillator. Finally, in the third phase, the scintillator is loaded with tellurium.

Figure 2.1 shows an illustration of the SNO+ detector. Approximately 2 km of rock shields the detector from the cosmic ray backgrounds (ex.: cosmic muons). At this depth, the total muon flux is reduced to less than $10^{-9}\,\mathrm{cm}^{-2}\,\mathrm{s}^{-1}$(Figure 2.2) [35]. Seven kilotonnes of ultra pure water fills the rock cavity, where the detector is located, giving the detector some additional shielding from backgrounds. The detector uses a 12 m diameter and 5 cm thick acrylic vessel (AV), which is going to be filled with scintillator. The scintillation light is detected by $\approx$ 9400 photomultiplier tubes (PMTs) located on the PMT support structure (PSUP) surrounding the AV. They cover about 54% of the solid angle of the target volume. There is also an array of PMTs facing away from the

target volume. These detect events that happen outside the AV and provides a veto to identify backgrounds and incoming muons.

The AV can be accessed through its neck, which has been surrounded by the deck clean room (DCR). The DCR is cleaner than the SNOLAB environment. This minimizes contamination of the AV during calibrations or maintenance.

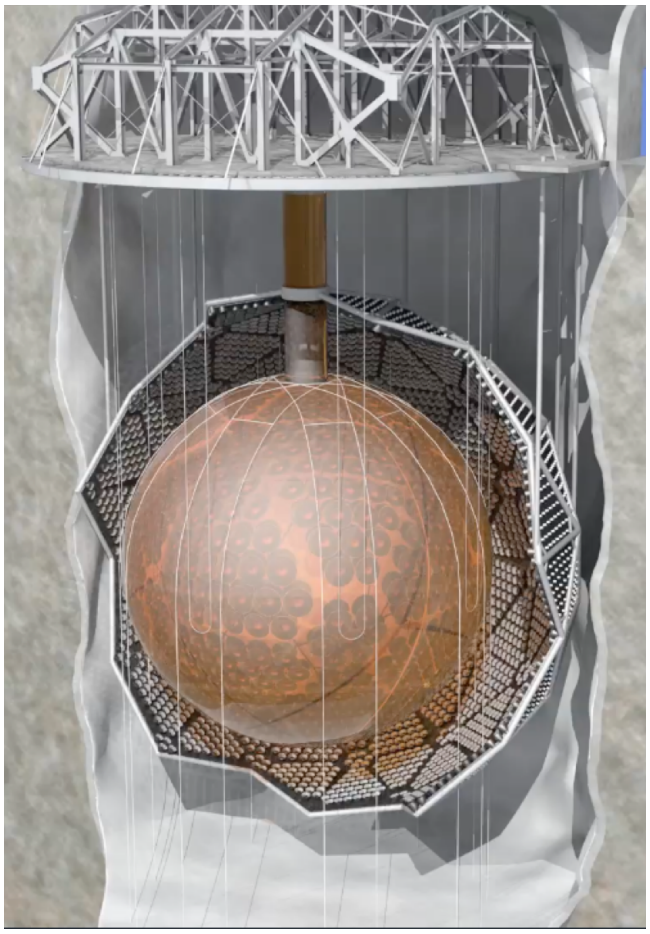

Figure 2.1: Artist illustration of SNO+ detector.

2.1.1 SNO

SNO+ is the successor to the Sudbury Neutrino Observatory (SNO) experiment. SNO was a heavy water Cherenkov detector able to measure the flux of solar neutrinos using neutral current interactions and the electron neutrino flux using charge current interactions. The experiment reached its goal to demonstrate that neutrinos indeed change flavour and confirmed the predicted

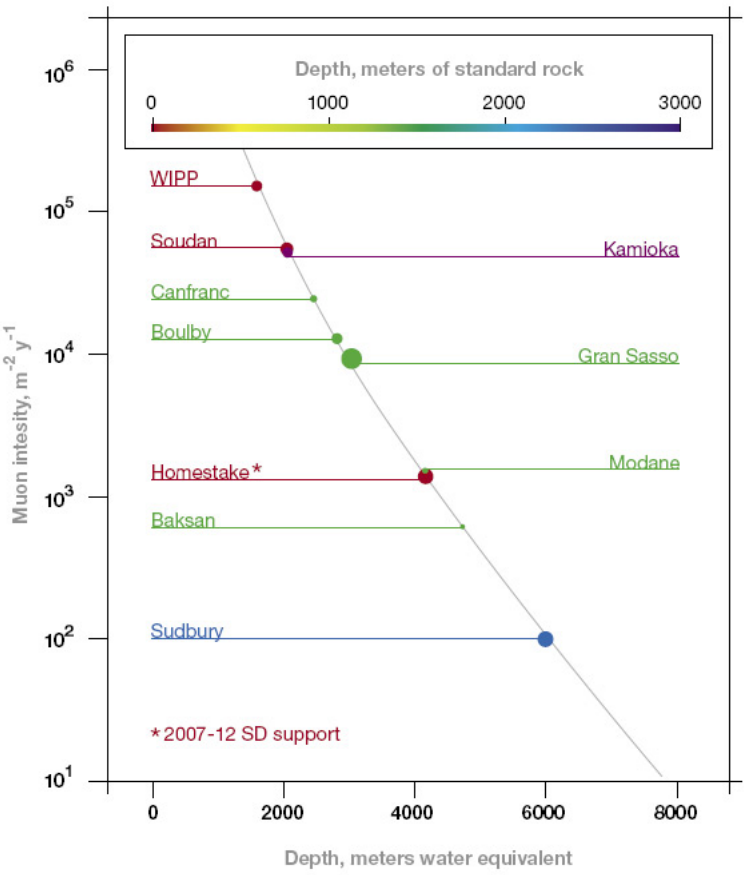

Figure 2.2: The muon flux dependency on the depth of the various underground laboratories.

solar models. This confirmation lead to the Nobel Prize in Physics awarded to Dr. Arthur B. McDonald jointly with Dr. Takaaki Kajita in 2015, for the discovery of neutrino oscillations, which shows that neutrinos have mass [36].

The neutrinos can interact with matter via charged or neutral current interactions and elastic scattering interactions as metioned previously in subsection 1.3.1, illustrated in Figure 2.3.

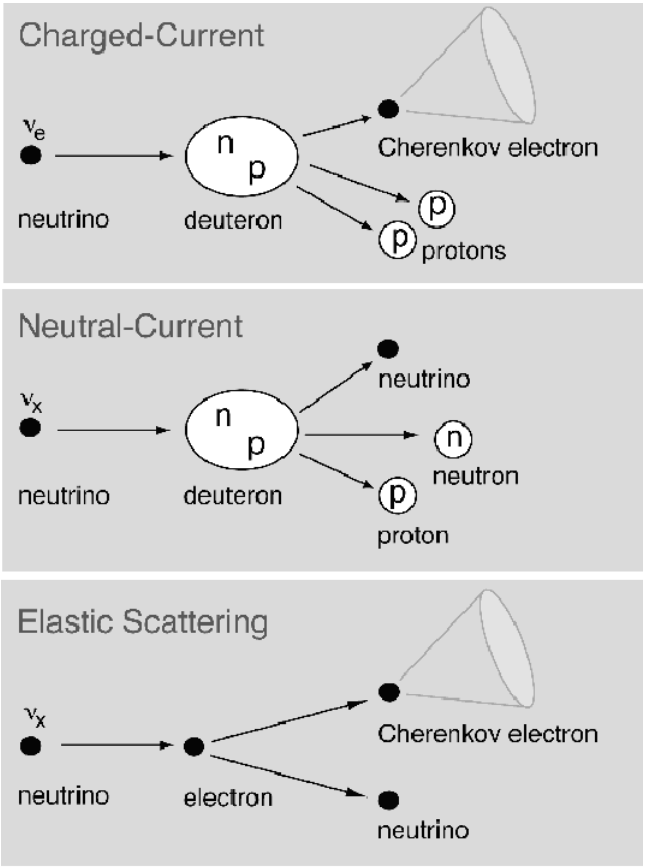

Figure 2.3: The charged current (CC), neutral current (NC) and elastic scattering interactions seen in SNO [37].

The separation between charged and neutral current interactions inside the detector involves separating the Cherenkov signals of the produced CC interactions from the secondary NC interaction signals. For this reason the experiment had three different phases, each one of them had different way of separating these interactions.

First phase involved the AV being filled with pure heavy water (D_2O). The NC interaction produces neutrons, which get captured onto deuterium nuclei. The capture produced 6.3 MeV γ-rays that scattered and produces electrons. Those electrons then produce Cherenkov light that has

a different energy range than the signal from charged current interaction. The difference in energy spectrum and multiple applied fits and analysis helped to distinguish the NC from CC interactions.

However, in order to fit the energy spectra the solar neutrino spectral shape had to be assumed, which is not ideal. Therefore, the second phase on SNO experiment had 2 t of NaCl disolved into the heavy water. Chlorine has large neutron capture cross section which produced several γ-rays. The light produced by several compton electrons following neutron capture was more isotropic than single electron CC interaction. From this the difference between these interactions could be defined by an isotropical parameter, which did not depend on energy. This gave additional information to distinguish between charged and neutral current neutrino interactions.

The third phase deployed an array of neutral current detectors (NCDs). These detectors were ^{3}He counters and provided separate neutral current measurement that was uncorrelated to charged current signals. NCDs detected the number of neutrons coming from neutral current interactions of coming solar neutrinos.This provided the total flux of ^{8}B solar neutrinos.

After the SNO experiment the existing SNO detector infrastructure was repurposed for SNO+. The existing detector cavity and AV volume with the surrounding PMT array matched the features required for large liquid scintillator detector. The upgrades from SNO to SNO+ are described in the following subsection.

2.1.2 Upgrades

SNO+ is using most of the already existing infrastructure from the SNO detector. Changing from heavy water Cherenkov to a liquid scintillator detector required a lot of changes to the infrastructure, electronics and software of the experiment.

The first major upgrade was the addition of a new rope system. When the AV was filled with D_2O for SNO, it was held up by the hold-up rope system since heavy water is denser than the surrounding ultra pure water (UPW). Since liquid scintillator (LAB-PPO) has a lower density than UPW ($\rho = 0.86 g/cm^3$ for LAB-PPO at T=12 °C), the AV becomes boyant and has to be restrained from floating up. This is done by the new hold-down rope net, anchored to the cavity floor, shown in Figure 2.4. The net is made with high purity, 38 mm diameter, Tensylon ropes. The original hold-up ropes were also replaced by Tensylon counter-parts to reduce radioactive contamination. Rope testing was done by filling the cavity to a level above the AV water level, thus simulating a

buoyancy effect, shown in Figure 2.5.

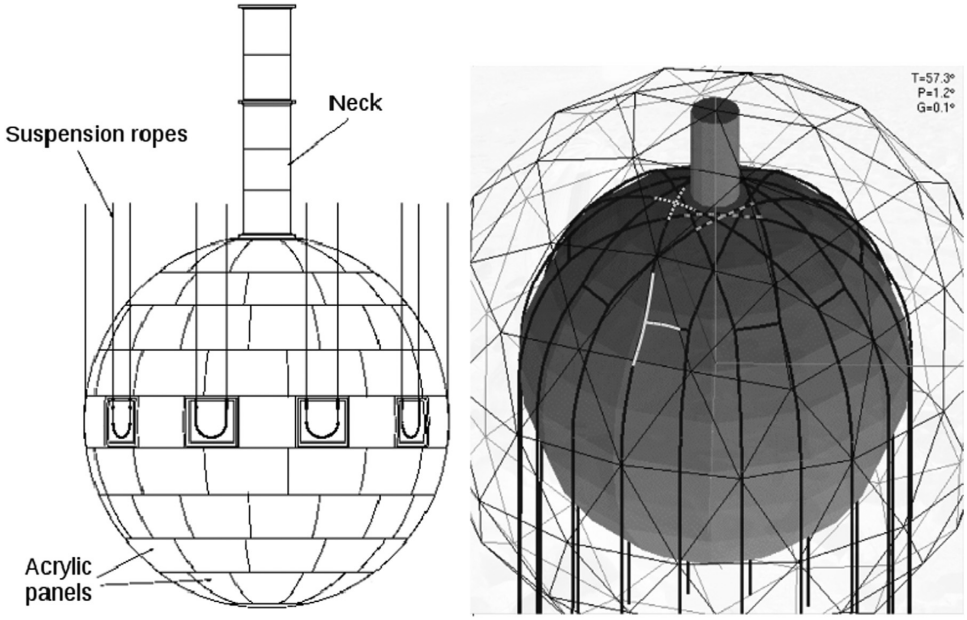

Figure 2.4: Left: Suspension ropes of the SNO AV. Right: SNO+ hold-down rope net [38].

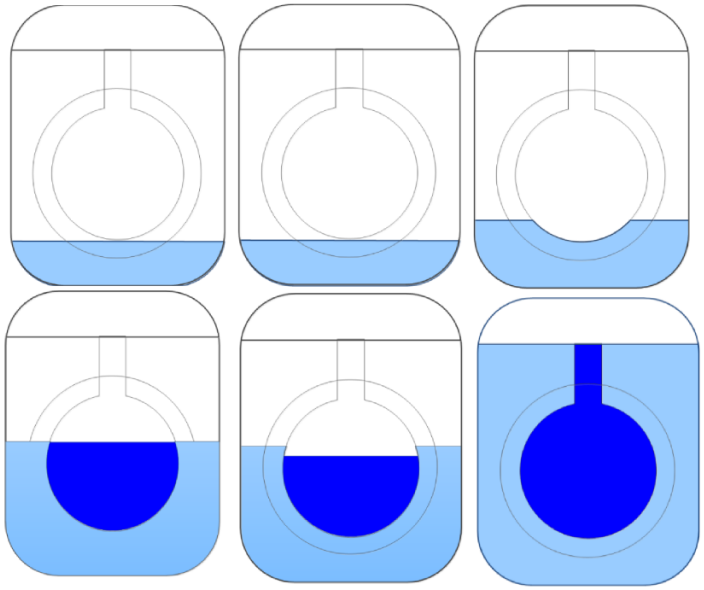

Figure 2.5: The stages of "Float The Boat" test, to test the rope strength, while simulating buoyancy of the acrylic vessel.

The data acquisition (DAQ) and trigger systems were upgraded to cope with the high light yield of scintillator compared to the Cherenkov radiation in SNO. Online monitoring tools have

been developed to be able to display data at 20 kHz. Also, a remote detector monitoring feature was added, a new alarm GUI was implemented to monitor any changes in operation, and the overall user interface was highly improved. Features such as extra crate voltage and current readouts allows operators to check changes from channel to channel. Because of the increased trigger rate from scintillation light, the grid based processing and the storage channels have been updated as well. The anticipated increased trigger rate also led to upgrades of the electronic hardware such as the addition of new XL3 readout cards and MTC/A+ trigger cards.

A new cover gas system was introduced to limit radon ingress into the detector. As radon decay chain daughters are a large part of the background for the experiment. The closed system with high purity nitrogen gas acts as a barrier between the detector and the radon in the outside air. There are also upgrades to the calibration system, discussed in more detail in Chapter 3).

Amidst these changes, the photomultiplier tubes will remain unchanged. SNO+ is using the 8 inch Hamamatrsu R1408 photomultiplier tubes from SNO [39]. Large numbers of malfunctioning PMTs, that failed over SNO lifetime, have been repaired and installed back into the detector.

2.2 Phases of experiment

The SNO+ experiment will have three main phases: the water phase, the pure scintillator phase, and the tellurium-loaded scintillator phase. Currently the detector is in the water phase, taking data. From water data we will gain knowledge of the internal and external backgrounds for the experiment. The detector is to be filled with scintillator in start of 2018.

2.2.1 Water Phase

In this phase, the acrylic vessel is filled with ultra-pure water. The main physics goals are the exotic searches. These include the search for invisible nucleon decay, axion-like particles, and supernova neutrinos. Also, reactor anti-neutrinos with an energy higher than 1.8 MeV can be detected. This phase will provide information about the DAQ characteristics, the PMT response, and overall de-

Goal/Phase	Water	Pure LAB	Te-loaded LAB
Neutrinoless double beta decay	-	-	✓
^{8}B solar neutrinos	-	✓	✓
CNO, pep solar neutrinos	-	✓	-
Reactor and Geo-neutrinos	-	✓	✓
Exotic searches	✓	✓	✓
Calibration goals	PMT response, electronics	Optical parameters, energy resolution, event efficiency	Optical parameters, energy resolution, event efficiency

Table 2.1: The main physics and calibration goals for the three SNO+ experiment phases.

tector performance since the upgrades were installed. This phase will allow the impurities, such as ^{210}Po and ^{210}Pb, embedded in the acrylic vessel to partially leach-out, which is important for the background studies. During the calibration of the water phase, the new fibre-based calibration system will also be tested. Good calibration and background understanding is critical for the quality data physics runs.

SNO+ will is looking for nucleon decay via ^{16}O decay to either ^{15}N or ^{15}O excited states. The signal will be observed via the emission of 6 MeV to 7 MeV gammas (45% of the time) from the deexitation of the daughter nuclei. Presently, the best limits set for invisible nucleon decay are 5.8×10^{29} years for neutron disappearance by KamLAND [40] and 2.1×10^{29} years for proton disappearance [41]. SNO+ should provide better measurements for nucleon decay as it will be more efficient. KamLAND looked at ^{12}C, while SNO+ will study this decay using ^{16}O. When a neutron decays the resulting ^{15}O is put into the excited state, it promptly deexcites 44% of the time emitting a 6.18 MeV gamma. In case of proton decay, the resulting nucleus will be ^{15}N. 41% of the time while deexciting ^{15}N will emit a 6.32 MeV gamma. Figure 2.6 shows the expected energy spectrum for water phase backgrounds within a 5.5 m fiducial volume cut and a cut on $\cos\theta_{sun} > -0.8$ applied [25]. θ_{sun} is the angle between the scattered electron and the position of the sun. The $\cos\theta_{sun}$ cut relative to the solar direction, reduces the dominant solar background.

2.2.2 Pure Scintillator Phase

The detector will be filled with $\sim$ 780 tonnes of pure liquid scintillator (LAB-PPO). The SNO+ scintillator is composed of linear alkylbenzene (LAB) $+2g/L$ of the fluor $2,5$ - diphenyloxazole

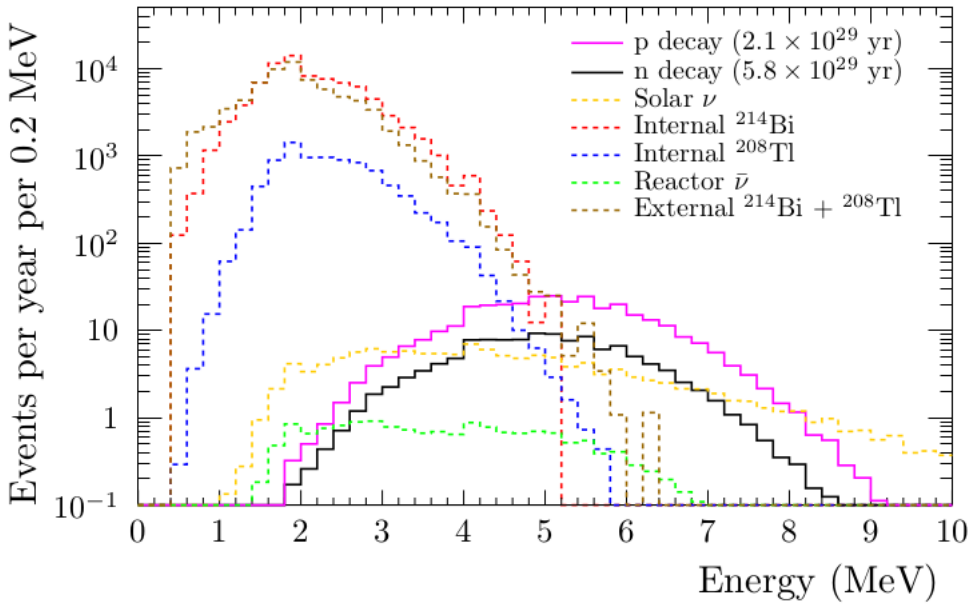

Figure 2.6: Expected energy spectrum for water phase backgrounds within a 5.5 m fiducial volume cut and a cut on $\cos\theta_{sun} > -0.8$ applied [25].

(PPO). LAB was selected because of its stability, compatability with acrylic, and high purity. It also has a long attenuation length with high light yield and linear response in energy, which makes it easy for the accurate reconstrucion of deposited energy. A new processing plant was constructed to purify the scintillator and reduce the backgrounds from the contaminants in the scintillator. The LAB fill is scheduled to start in late 2017 and to be completed by 2018. During this phase, the scintillator calibrations will take place (including the AmBe neutron source deployment discussed in this thesis). After the calibrations, the reactor and geo anti-neutrino studies alongside low energy solar neutrino signals will be measured.

2.2.3 Te-loaded Scintillator Phase

The tellurium-loaded phase is important for the $\beta\beta0\nu$-decay search. Telluric acid, $Te(OH)_6$ is loaded into the scintillator and then a secondary wavelength shifter will also be added, to better match the PMT quantum efficiency. ^{130}Te was chosen due to its large natural abundance (34%) and its long $\beta\beta2\nu$ half-life. $\beta\beta2\nu$ is a large background for $\beta\beta0\nu$ events. Therefore long $\beta\beta2\nu$ half-life minimises the background events coming from this decay. For the $\beta\beta0\nu$ decay ^{130}Te has a Q-value of 2.53 MeV. During this phase, the detector is expected to be operated with a loading of 0.5%

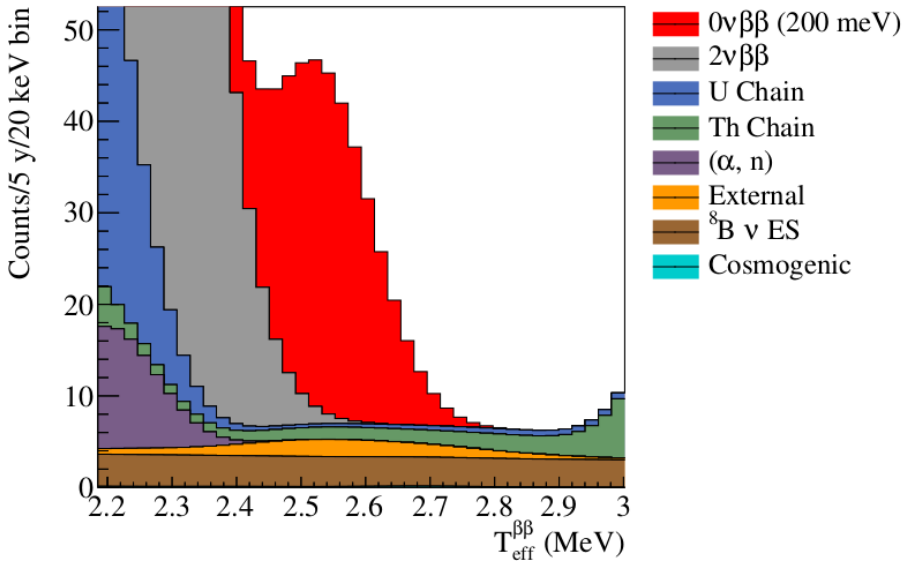

Figure 2.7: The expected $\beta\beta0\nu$-decay signal and its backgrounds for 5% Te-loading. The counts are estimated over 5 years of data taking.

natural tellurium in LAB. The expected $\beta\beta0\nu$-decay with its backgrounds can be seen in Figure 2.7 for the future phase with 5% loading. It shows the counts for the case of the m_ν =200 MeV, over 5 years worth of measurement. The proposed scintillator "cocktail" is LAB+PPO ($2\,\mathrm{g\,l^{-1}}$) + bisMSB ($15\,\mathrm{mg\,l^{-1}}$) loaded using the Te-Diol method (0.5%). The assumed light yield of the cocktail is 390 hits/MeV. Figure 2.8 shows the different background contributions in the region of inetrest for neutrinoless double beta decay event for one year of Te-Diol "cocktail" dicussed above.

2.3 Anti-neutrino Detection

Electron neutrinos most commonly interact via elastic scattering with electrons because of the large cross section of this interaction (Equation 2.1).

$$\nu_e + e^- \rightarrow \nu_e + e^- \tag{2.1}$$

These interactions induce excitations in the scintillator, which then produce photons that get detected by the PMTs. The electron antineutinos are detected via the inverse beta decay interaction,

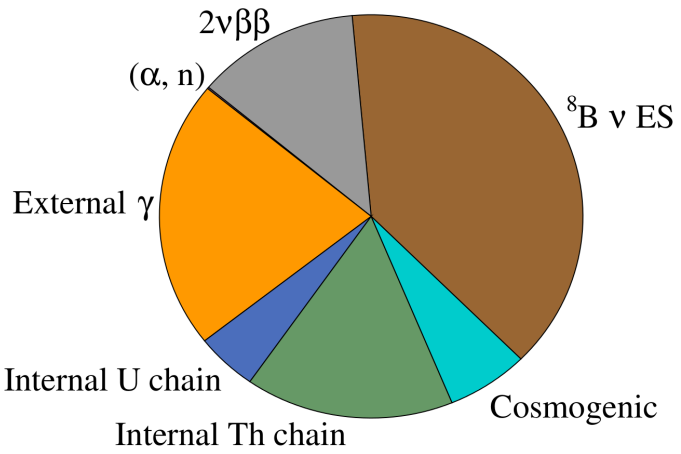

Figure 2.8: Pie chart for the different background contributions in the region of interest for neutrinoless double beta decay events for one year of Te-Diol scenario.

shown in Equation 2.2 and explained in more detail in Section 1.5.

$$\bar{\nu}_e + p \rightarrow e^+ + n \tag{2.2}$$

As illustrated in Figure 2.9, the incoming anti-neutrino hits a proton which creates a positron and a neutron. Compared to the neutron, the positron quickly annihilates with an electron releasing two gammas and creating a prompt signal. The neutron takes time to thermalise and gets captured within the scintillator onto another proton (mean lifetime $\approx 220\mu s$), this produces 2.2 MeV gamma. This 2.2 MeV gamma peak is the delayed neutron capture peak. These two signals serve as a tag for electron anti-neutrino interaction in scintillator. Therefore, an understanding of the neutron detection efficiency of the SNO+ detector is extremely important. The neutron capture efficiency calibration is the main focus of this thesis.

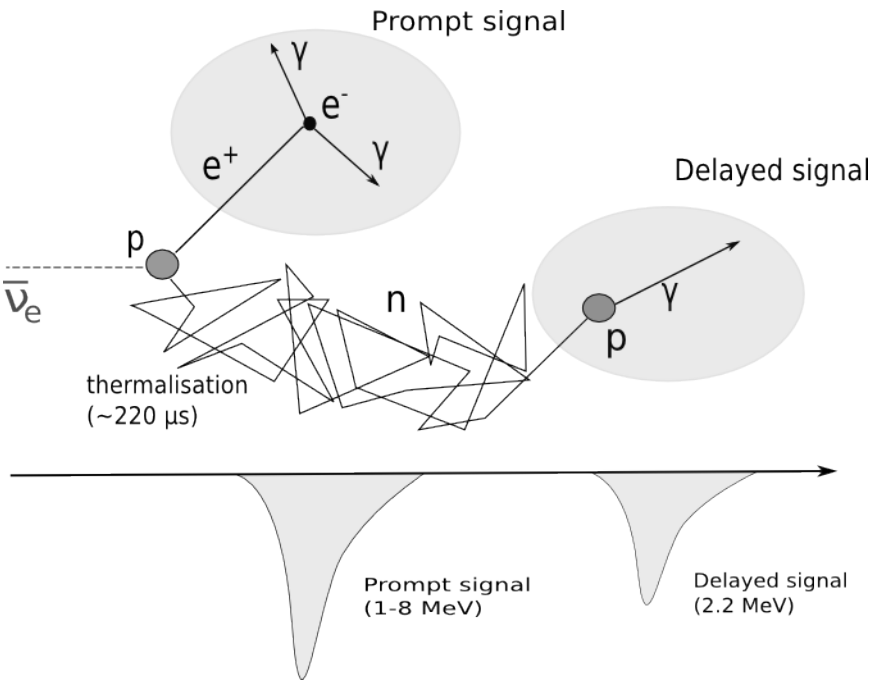

Figure 2.9: Illustration of the inverse beta decay reaction inside the scintillator for electron anti-neutrinos.

Chapter 3

Detector calibration

Calibration is necessary for understanding the detector response over the full energy range (0.1-10MeV). In particular, it is necessary to understand the performance of the detector in reconstruction of particle type, energy, and position. Calibration is required to determine the uncertainties on these reconstructed values.

The three different phases of SNO+ have different calibration goals that will end up complementing each other. In the water phase, the main goal is to characterise the electronics, the response of the PMTs and light reflectors and to take data for water physics discussed in subsection 2.2.1. Furthermore, in the pure scintillator phase, the most important parameters to understand are the scintillator optical absorption, reemission, and scattering as well as the energy resolution and neutron event efficiency. Moving into the Te-loaded phase, the parameters determined in previous phases will have to be modified because tellurium will change the properties of the scintillator.

Various optical sources (LEDs and lasers coupled to optical fibres) and radioactive sources (γ,n) are used to calibrate the detector. The optical sources are used to calibrate the PMTs and the optical properties of the target (water, scintillator). The radioactive sources are used to measure energy scale, resolution and detection efficiency of various particles. Comprehensive Monte Carlo simulations are done for each source in order to compare the expected detector response to the actual calibration data. A calibration analysis plan was developed to ensure that all properties in the detector model can be measured to the necessary accuracy for physics data runs. An estimation of the background rates and of the detection efficiency can be determined during the calibration. From the calibration analysis work, the required uncertainties can be added to the reconstruction

of physics events.

3.1 Calibration hardware

Sources are connected to an umbilical and lowered down into the detector through the neck, as shown in Figure 3.1. The umbilical provides all the necessary feeding lines to the source such as high voltage or output cables. The Umbilical Retreval Mechanism (URM) stores the umbilical and contains motors that control it. A glove box, located on the top of the detector provides temporary storage for the sources that are not in use. A central rope supports the weight of the source, while side ropes are used to move the source inside the detector, for positional analysis. The ropes are controlled by the rope motors.

With the help of the side ropes, the detector can be scanned off the central axis in two orthogonal planes. A system of cameras inside the detector is used to monitor the position of the AV and the ropes. Also, it will provide information about the deployed source position by detecting an LED light attached to the source container.

Deployment of the sources is done through a new universal interface (UI) that was designed for SNO+. The UI also provides sensor information from the water level sensor and the veto PMTs.

All of the materials used in the calibration hardware are designed to match the purity requirements of SNO+ and need to be compatible with LAB.

3.2 Optical calibration sources

The optical calibration sources inject light pulses into the detector through optical fibres mounted on the PSUP Figure 3.2. The injected light is in the 375 nm to 510 nm range.

These optical sources were first used to calibrate the PMT timing and gains. The calibration used 92 sets of fibres which covered the entire set of PMTs [42]. The position reconstruction is highly dependent on the timing calibration of the entire detector. The time response depends on the decay time of the scintillator signal and overall synchronisation of the PMT array. The PMT gain calibration is important for the energy reconstruction. Time and charge information are measured for each PMT pulse. The required dynamic range of PMT gain is between 1 to 4 photoelectrons.

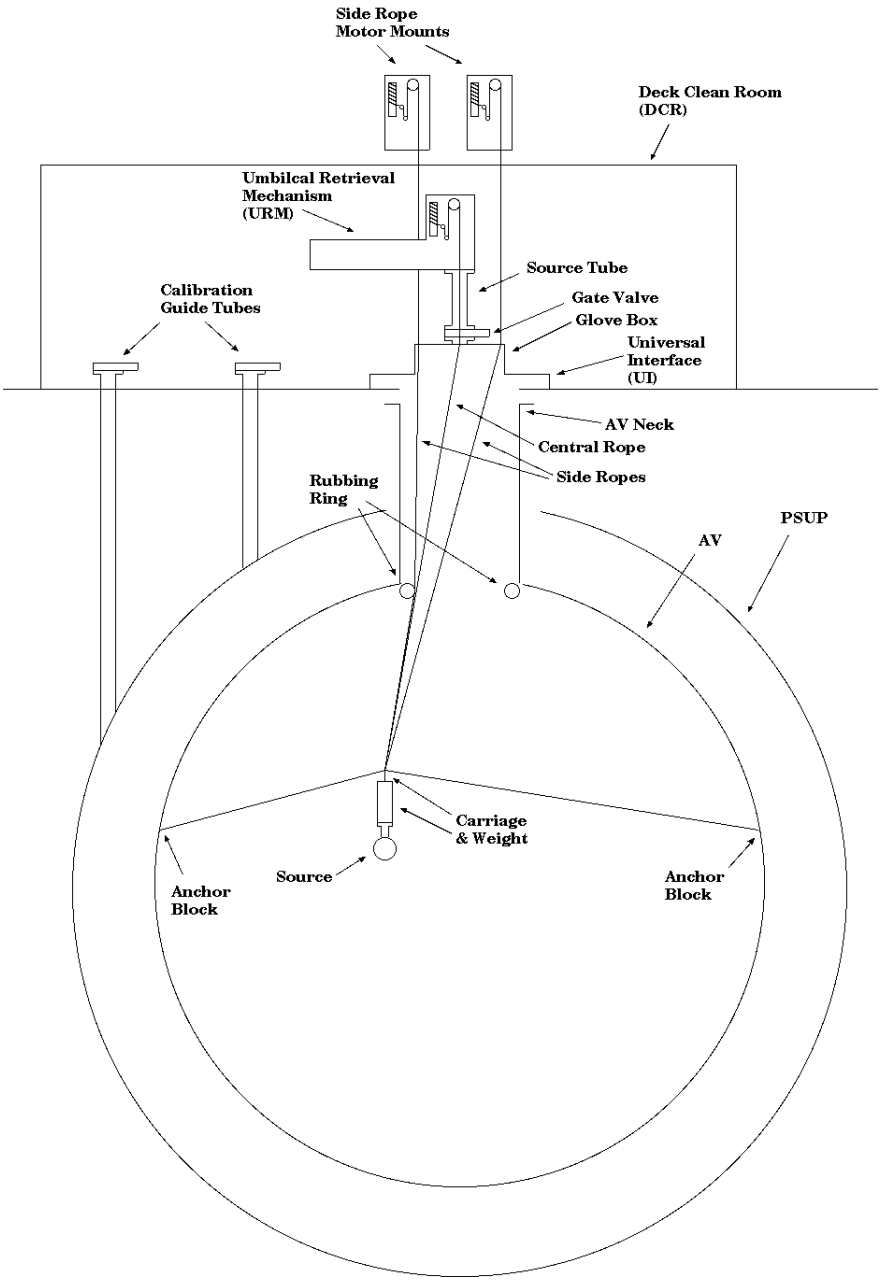

Figure 3.1: Illustration of the calibration source deployment mechanisms.

The second part measures scattering properties of the scintillator using four pencil beams from a multi-wavelength laser source [43]. If a photon scatters before reaching a PMT, the reconstruction becomes harder. Therefore, the understanding of scintillator scattering is very important. The laser beams with different wavelengths were aligned with samples of scintillator and the PMT counts were recorded. Then from the series of calculations dicussed in [43], corrections and fitters can be applied to the data to include the scintillator scattering effects. Finally, the optical attenuation was measured by injecting four narrow light beams from LEDs, with different wavelengths.

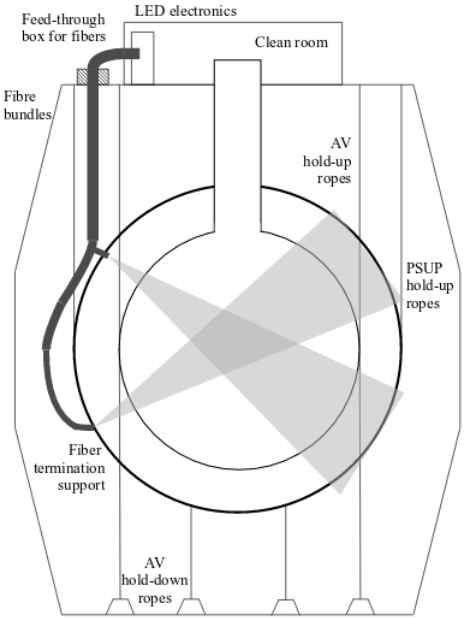

Figure 3.2: Sketch showing an example of the light injection points [42].

3.3 Radioactive calibration sources

In the transition from SNO to SNO+, a substantial amount of work has gone into updating and creating new radioactive calibration sources. These are needed because of the different energy thresholds for scintillator and water, and because of the increased cleanliness requirements. Table 3.1 shows the deployed radioactive calibration sources that will be used over the SNO+ calibration phases. A variety of neutron and gamma sources will be used during the calibration.

In addition, α and β sources were also considered but due to the high risk of contamination of the detector, they have not been deemed appropriate for SNO+. However, similar calibration

information can be obtained from internal radioactive sources. Some naturally occuring radiation comes from ^{238}U and ^{232}U chains inside the liquid scintillator. The ^{210}Po-α, ^{14}C-β, delayed ^{214}Bi-Po and ^{212}Bi-Po coincidences are typical calibration references for alpha and beta signals [25].

Source	Particle	Energy	Tag
AmBe	n,γ	2.2, 4.4 MeV	coinc.
^{16}N	γ	6.1 MeV	yes
^{48}Sc	γ	1.0, 1.2, 1.3 MeV	no
^{57}Co	γ	122 keV	no
^{46}Sc	γ	0.89, 1.12 MeV	yes

Table 3.1: The radioactive calibration sources for SNO+

The ^{57}Co source with a low energy of 122 keV is going to be used to check the detector response at the trigger threshold. The ^{16}N source is designed in a way that its signal can be tagged inside its container. Therefore, they are great for analysis of detector pulse shape, energy and position calibration. Finally, the neutron calibration is done using the AmBe source and is tagged using the coincidence between neutrons and gammas in the decays. The AmBe source is the focus of this thesis and will be discussed in greater detail in the Chapter 4.

Chapter 4

Neutron source design

AmBe is a neutron source, which consists of a mixture of ^{241}Am and ^{9}Be. The ^{241}Am produces α particles. The alpha particles then react with beryllium. The two dominant processes are shown in Equation 4.1 and Equation 4.2.

$$\alpha + {}^{9}\mathrm{Be} \rightarrow {}^{1}\mathrm{n} + {}^{12}\mathrm{C} \quad Q = 5.701\mathrm{MeV} \tag{4.1}$$

$$\alpha + {}^{9}\mathrm{Be} \rightarrow {}^{1}\mathrm{n} + {}^{12}\mathrm{C}^{*} \xrightarrow{\text{deexcites}} {}^{12}\mathrm{C} + \gamma + 4.44\mathrm{MeV} \quad Q = 1.261\mathrm{MeV} \tag{4.2}$$

The cross sections for Equation 4.1 and Equation 4.2 reactions depend on the alpha energy. The source activity is dependent on the arrangement of the ^{241}Am and ^{9}Be within the source itself. The minimum spacing between the isotopes creates larger contact are for the actinide to induce the (α, n) reaction. The AmBe sources can be "foil sources" or "powder sources". The SNO experiment had one of each type: "AmBe med" and "AmBe high" (foil and powder respectively). However, SNO+ is using the powder type AmBe source ("AmBe high"). The powder source has a higher activity than its foil type counterpart, as the powder has a larger interfacial area.

Depending on the energy of the produced alpha, the neutron and the coresponding ^{12}C excitation level changes. Therefore, the produced gamma energy and neutron energy are co-dependent. The deexcitation levels of carbon with corresponding gamma energies are shown in Figure 4.1 and listed below. Important to note that π next to excitation energy of 7.654 MeV does not stand for pion, it

represents the special case called Hoyle state, which deexites through pair production (e^+,e^-) [44].

- $E_n > 6\,\text{MeV}$, ground state, no gamma emitted.
- $1.9 < E_n < 6\,\text{MeV}$, 1st excited state, $4.438\,\text{MeV}$ γ emitted.
- $0.5 < E_n < 1.8\,\text{MeV}$, 2nd excited state, $3.215\,\text{MeV}$ γ emitted when decays into 1st excited state, then $4.438\,\text{MeV}$ γ emitted when going to ground state.
- $E_n < 0.5\,\text{MeV}$, no gamma

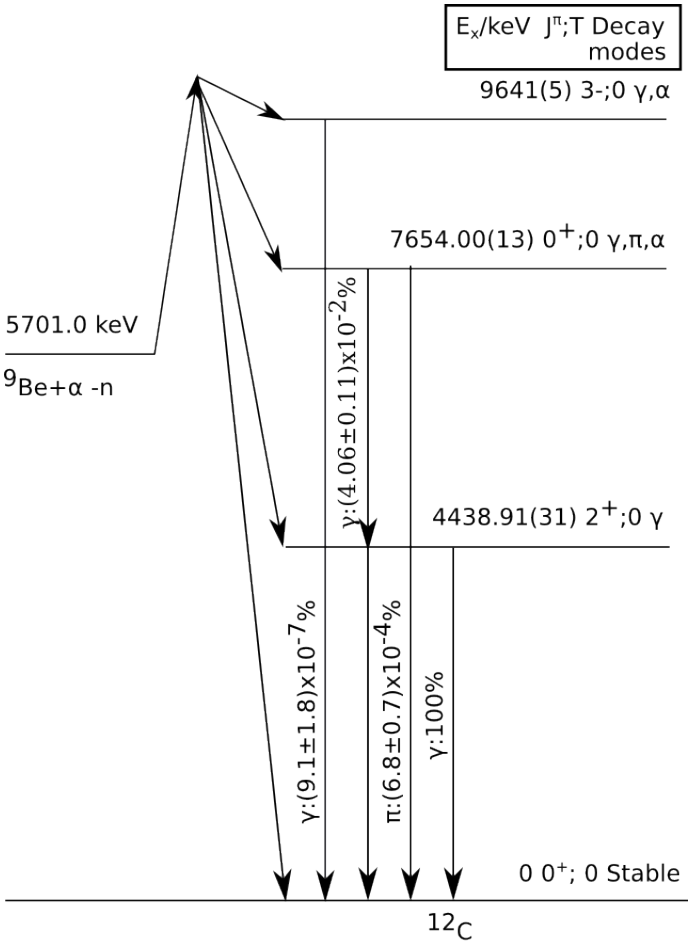

Figure 4.1: The deexcitation modes of ^{12}C in the $^9\text{Be}(\alpha, n)^{12}\text{C}$ reaction (values taken from [45]).

The activities of the AmBe sources used in SNO were: 23.63 ± 0.27 n s^{-1} for "AmBe med" and 68.70 ± 0.74 n s^{-1} for "AmBe high" [46]. The SNO schematics for both of these sources can be

seen in Figure 4.2.

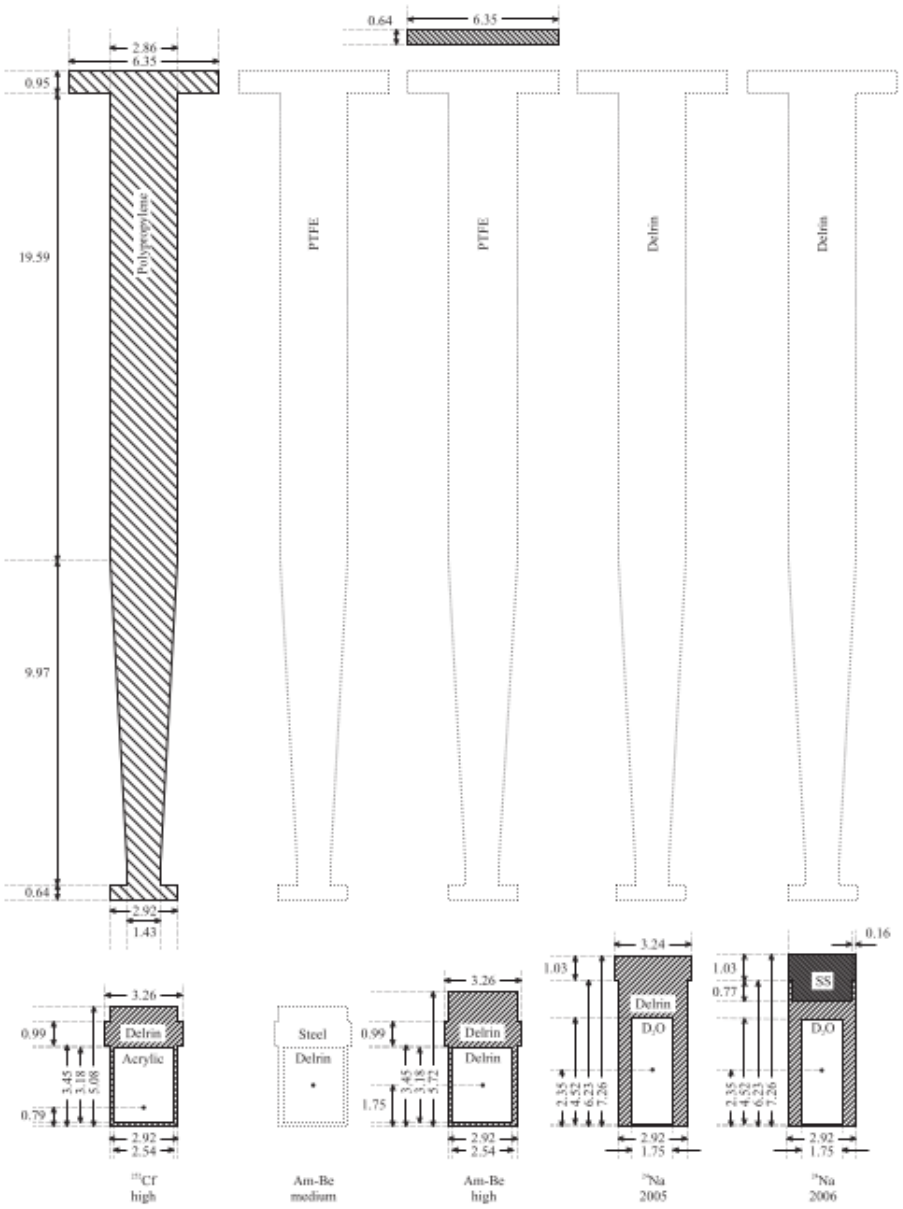

Figure 4.2: The schematics of SNO NCD phase neutron calibration sources. The AmBe source discussed in this thesis is denoted as "Am-Be High" [46].

4.1 Source simulation software

Reactor Analysis Tool (RAT) is the simulation software that combines Monte Carlo (MC) simulations with event-based analysis tasks. This software is integrated into the GEANT4 software, which

is used by numerous physics collaborations for particles going through matter MC simulations [47] [48] [49]. All of the macros for RAT are written in C++. The analysis for this thesis was done with GEANT4.10.0.p02, RAT version 5.3.2 and all the output files were analysed using ROOT 5.34.34. The C++ macro files were used to extract information from created ROOT output files. By doing so, the processing power is used more efficiently on tools such as function generators and data cuts.

The SNO+ collaboration is constantly updating and developing RAT for better use of the physics needed for the experiment. The geometry of the detector and its components are stored in a dedicated database. The geometry of different calibration sources and materials can be added. Part of the discussion later in this thesis will be the different geometry files of AmBe source and additional materials that were added to the materials files in the database (subsection 4.1.1).

After the simulation of the detector response is completed, the data is stored in the EV and MC branches of the output ROOT file's TTree. The EV branch stores the information that would be accessible after an actual measurement within the detector. The MC branch has detailed information of the simulated particles and their tracks. Using the information from both branches makes it easy to do a detailed analysis of advantages and disadvantages of different source geometries.

4.1.1 AmBe source geometry

The geometry of the AmBe source inherited from SNO is composed of the source container and a source holder. In the geometry file, these source parts are defined as polycones. This allows the use cylindrical coordinates to define the dimension of the layer volumes. The particles produced by the source are simulated as a point source inside the most inner volume of the source container. Generators at the end of the macro files can generate: individual particles, particles in coincidence, or the full spectrum of source particles. The old generator for the AmBe source generates neutrons and gammas in coincidence. Improvements made to this generator will be further discussed in subsection 4.1.2.

The Figure 4.3 shows the illustration of the main AmBe source geometry parts that were manipulated. The geometry has the original source encapsulation made out of derlin denoted as "`G4_POLYOXYMETHYLENE`" within the source geometry file. The original encapsulation of the source is going to stay untouched, as the source is already double encapsulated and the activity is known. Leaving the original encapsulation intact makes the source extra safe from the potential

faults. Breaking the original seal is not desired due to the possible contamination from the source. Cleaning the existing AmBe source encapsulation and adding extra can will make it cleaner and safer for future use. The detailed schematics for the original encapsulation of the AmBe source can be seen in Figure A.1.

The parts that are added and manipulated are the source shielding and the new encapsulation. The optimisation of the shielding material is shown in detail in Section 4.2. The shielding material will be optimised to prepare the AmBe source for the scintillator phase, several different materials are explored for the shielding. The new encapsulation layer is made out of a thin layer of stainless steel to separate the shielding material from the LAB in case that the chosen shielding material is not compatible with scintillator. For the source shielding layer high atomic number materials were considered since the shielding of photons is important. The cleanliness of the materials also has to be considered, these are discussed in subsection 4.2.1.

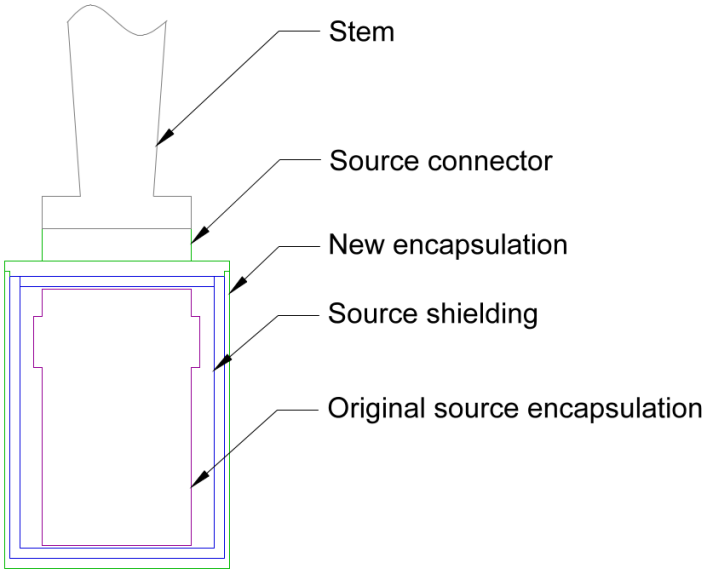

Figure 4.3: The schematic of the main AmBe source geometry parts for illustration. The shielding and new encapsulation layers were manipulated and optimised.

Since Teflon does not contain hydrogen, it is a very weak absorber of neutrons, which makes it a good material choice for the stem. The stem separates the source container from the source manipulator. The manipulator provides the additional weight needed for the movement of the

source inside the LAB. It is made out of stainless steel which is a material that is good at absorbing neutrons. Therefore, having a stem to separate the source form the manipulator decreases the amount of neutrons reabsorbed by the source deployment system.

The source connector connects the source capsule to the stem. The original source connector was made out of Derlin as well. However, delrin is not compatible with LAB, and for the refurbishment the material for the connector was changed to stainless steel to match the new source encapsulation. Even though stainless steel is good at absorbing neutrons, having thin layer closer to the source does not affect the neutron count significantly, as demonstrated in Section 4.2.

4.1.2 AmBe source event generator

As explained in Chapter 4, the AmBe source produces neutrons via (α, n) reactions. The AmBe event generator code for the MC simulations was inherited from the DEAP-1 experiment [46]. The spectrum creates the separate neutron spectrum in coincidence with 4.4 MeV gammas 60% of the time and 10 keV gammas 40%. These low energy 10 keV gammas were below the energy threshold for detection for the water phase. However, the SNO+ scintillator phase is sensitive to lower event energies, therefore having the actual energies and ratios for the produced low energy gammas is desired. Also as shown in the Figure 4.1, there is a correlation between the neutron spectrum and the produced gamma energies, which was not implemented in the DEAP-1 AmBe generator. The AmBe spectrum from this generator can be seen in Figure 4.4.

DEAP-1 AmBe generator was modified to include the correlations between the neutron and gamma energies. Work performed in this thesis tests the new and improved generator for the scintillator phase. Multiple simulations were done to test the features of the SNO+ AmBe generator to include the correct deexitation modes, applications of the generator are shown in Chapter 5. The Figure 4.5 shows the NHit spectrum produced using the new AmBe generator, which includes the correlation between neutrons and gammas with the appropriate deexcitation modes of ^{12}C. The sharp neutron capture peak lies around 1200 NHits, which equates to approximately 2.2 MeV. The 4.4 MeV γ peak is more spreadout and lies in between 2200 $\rightarrow$ 3000 Nhits. The effect of the ^{12}C going into a second excited state and producing 3.213 MeV γ shortly followed by 4.4 MeV γ is seen at approximately 3600 NHit which would corresponds to the energy of the sum of both gammas.

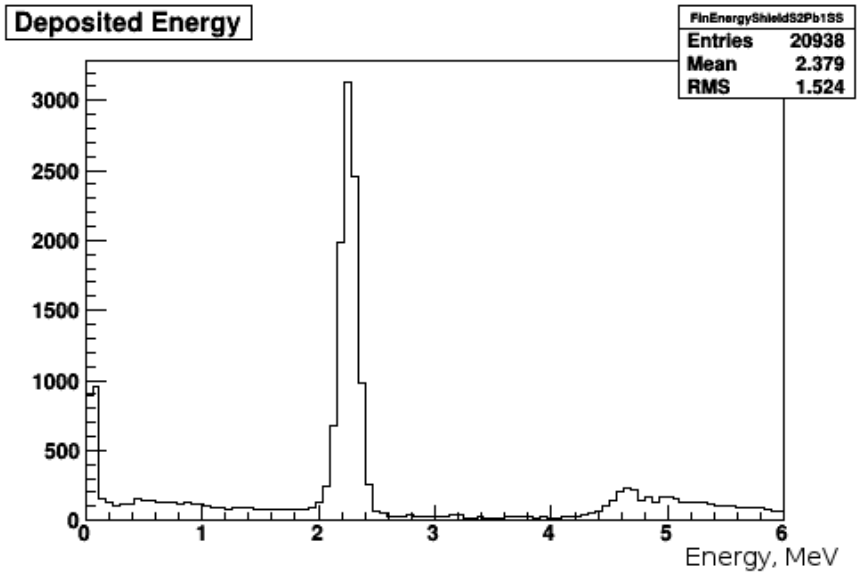

Figure 4.4: The energy fit of the DEAP-1 AmBe generator. Neutrons and gammas in coincidence. The gamma spectrum simulates the branching fraction by generating 60% of 4.4 MeV and 40% of 10 keV gammas.

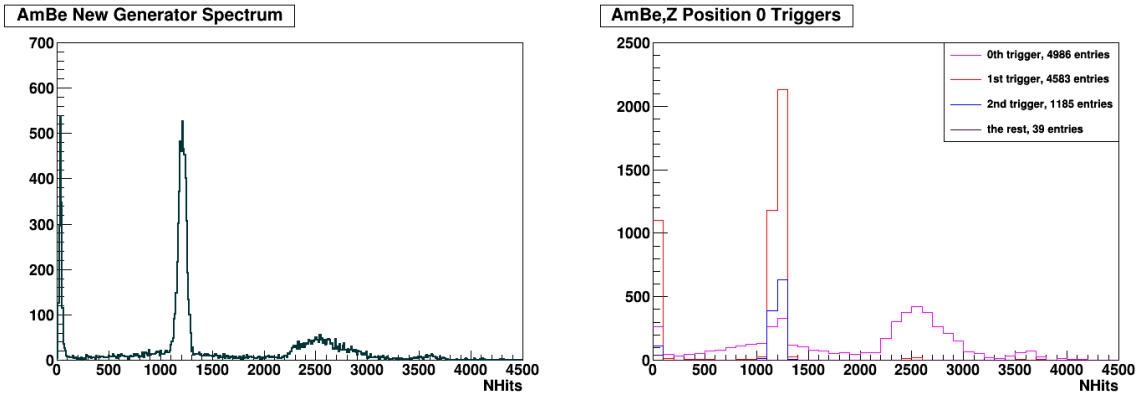

(a) The NHit plot produced using the new AmBe generator (5000 events).

(b) The breakdown of the separate NHit triggers. The 0th trigger represents the first reconstructed event associated with a simulated particle.

Figure 4.5: The NHit spectrum produced using the SNO+ AmBe generator, which includes the correlation between neutrons and gammas with the appropriate deexcitation modes of ^{12}C in the $^{9}\mathrm{Be}(\alpha, n)^{12}\mathrm{C}$ reaction, shown in Figure 4.1.

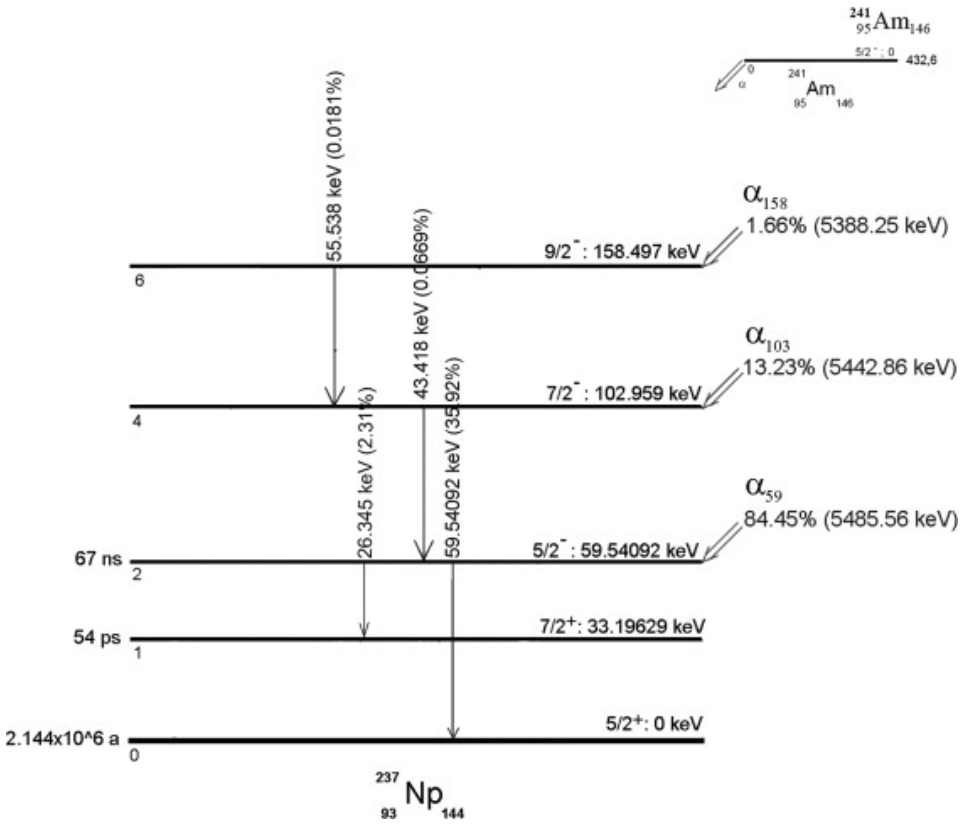

Figure 4.6: ^{241}Am decay scheme [50]

4.2 Shielding simulations

^{241}Am decays by alpha transitions to ^{237}Np. Most of the decays (84.6%) populate the excited state of ^{237}Np with energy of 59.54 keV. The deexitations of the created ^{237}Np excited states emit large numbers of low energy gammas. Most commonly, 35.92% of the time, the energy for these low energy gammas is 59.5 keV, shown in Figure 4.6 [50]. With each produced neutron, the source emits approximately 10^6 59.5 keV gammas. In water Cherenkov detectors, the low energy rays were not a problem, because of the higher energy threshold of ∼260 keV. For scintillator, the energy threshold is much lower, making these 59.5 keV gammas a significant background for the neutron detection.

A new AmBe source shielding has to be constructed for the SNO+ scintillator phase, such that the low energy rays would be filtered out without stopping too many of the 4.4 MeV gammas, which are used as a neutron tag.

4.2.1 Shielding materials

High atomic number materials are considered since the shielding of photons is important. Lead is commonly used for radiation shielding because of its density (ρ =11.3 g cm^{-3}), but it is not considered a "clean" material. If exposed to the LAB, it would contaminate the detector. Therefore, to consider lead, it has to be encased within an outside container, that is compatible with LAB. Tungsten, being an excellent but expensive shielding material, was also considered for the AmBe source. It has a high density (ρ =19.3 g cm^{-3}) and a high melting temperature (3410 °C), which makes it a commonly used material for photon shields and beam collimators within science experiments. Hevimet (a tungsten alloy) was considered for the AmBe source shielding as well. It consists of 90% tungsten, $\sim$ 7% nickel and $\sim$ 3% copper (depending on the manufacturer, the ratios might vary). The typical density of Hevimet is ρ =16.9 g cm^{-3} to 17.2 g cm^{-3} [51].

Stainless steel is another material widely used in radiation shielding. It has relatively high density (ρ =7.87 g cm^{-3}) and is composed of 71% iron, 19% chromium, and 1% nickel. It has good resistance to corrosion and is a non-magnetic material, which makes it commonly used in many accelerator components.

The original source container from SNO is made out of polyoxymethylene ($(CH_2O)_n$, ρ =1.41 g cm^{-3}). Due to it's hydrogen content, it can easily absorb neutrons. It is thus a poor choice of material for the encapsulation of a neutron source. Thermal neutrons get captured through a ^{1}H$(n,\gamma)^2$H reaction and emits 2.2 MeV gamma.

These materials were carefully considered and multiple simulations were performed to optimise a suitable shielding for the AmBe source.

4.2.2 Simulating gammas

The selection of the appropriate shielding material was done in two steps. First the most promising shielding material was identified. Then additional simulations were performed to fine-tune the selection. First, separate simulations of 59.5 keV and 4.4 MeV gamma particles (10000 events each) emitted from a point source were performed using a range of thicknesses for different shielding materials Table 4.1. All shieldings have an extra 1 mm of stainless steel around them, because lead and hevimet are not compatible with LAB. Compared to lead and hevimet, stainless steel appeared

to be a poor shielding choice. A large thickness of it would be required to shield an acceptable fraction of the 59.5 keV gamma particles but a large portion of 4.4 MeV gammas would also be blocked, which would make the neutron tagging less efficient. On the other hand, both lead and hevimet shielded all the 59.5 keV gammas (at thicknesses of 2 mm and greater) but since hevimet shielded more 4.4 MeV gammas, lead was chosen to be investigated in more detail.

Material	Lead		Stainless steel		Hevimet	
Thickness	59.5 keV	4.4 MeV	59.5 keV	4.4 MeV	59.5 keV	4.4 MeV
1 mm	0.03%	84.68%	6.25%	87.44%	0.06%	82.86%
2 mm	0%	80.34%	2.1%	84.74%	0%	75.22%
3 mm	0%	73.70%	0.69%	82.74%	0%	70.09%
5 mm	0%	71.63%	0.37%	80.51%	0%	62.68%
7 mm	0%	63.84%	0.06%	76.04%	0%	52.82%
8 mm	0%	60.81%	0.02%	74.78%	0%	49.21%

Table 4.1: The % of gammas let through the different thicknesses of lead, stainless steel and hevimet. The NHit distribution plots for samples of 10000 events with each thickness can be seen in Appendix B.

Larger simulations with more statistics were performed within the range of 1 mm to 3 mm of lead to explore the material in more detail. 10^6 events of 59.5 keV gamma were simulated, because that is the number of gammas per neutron we approximately expect to see from the source. Figure 4.7 shows the Nhit distribution of 59.5 keV γ. With 2 mm of lead shielding only one 59.5 keV γ event triggers the detector, which would make the background to be 1 59.5 keV γ per 1 neutron event. Figure 4.8 shows 10^4 events of 4.4 MeV gamma simulated inside the lead shielding. The number of 4.4 MeV γ penetrating the shielding declines by approximately 4% with every milimeter. It is desirable to keep the number of 4.4 MeV γ above 80% for the better neutron tagging efficiency.

4.2.3 Simulating neutrons

Figure 4.9 shows an energy peak at 2.2 MeV, which is exactly where we expect the neutron capture peak to be. The plot was derived by running a scintillator fitter when simulating events and then getting the deposited energy information from the fitter. The number of hits in the legend is integrated from the peak but it is important to note that it also includes the secondary triggers. Hence, the number of hits seen in the peak is larger than the number of gammas generated inside the source.

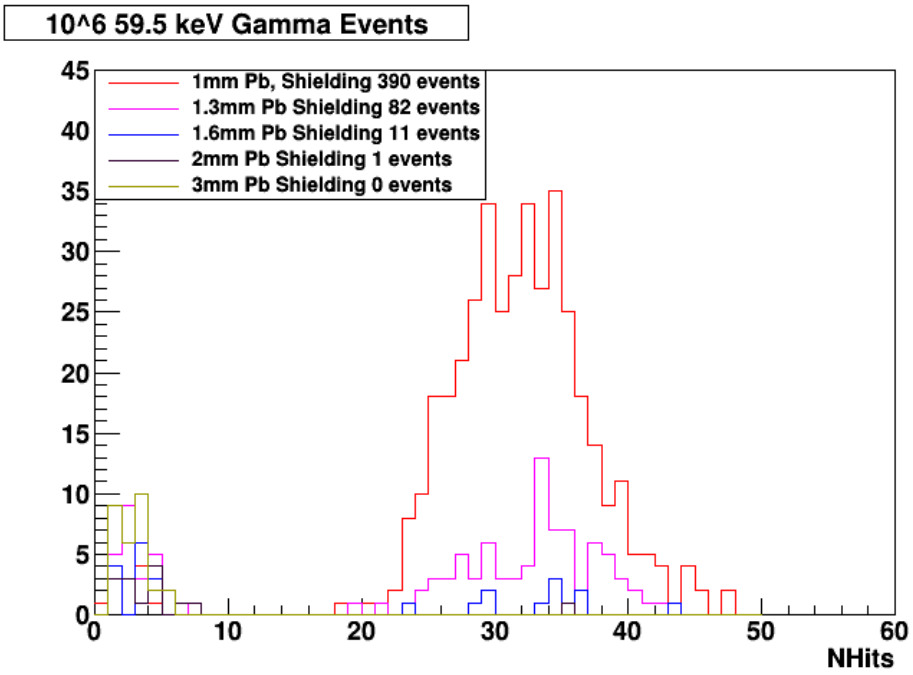

Figure 4.7: The Nhit plot of 10^6 events of 59.5 keV γ generated. With different thicknesses of lead shielding around the source. The legend shows the number of triggers within the range of $10 \rightarrow 50$ NHits.

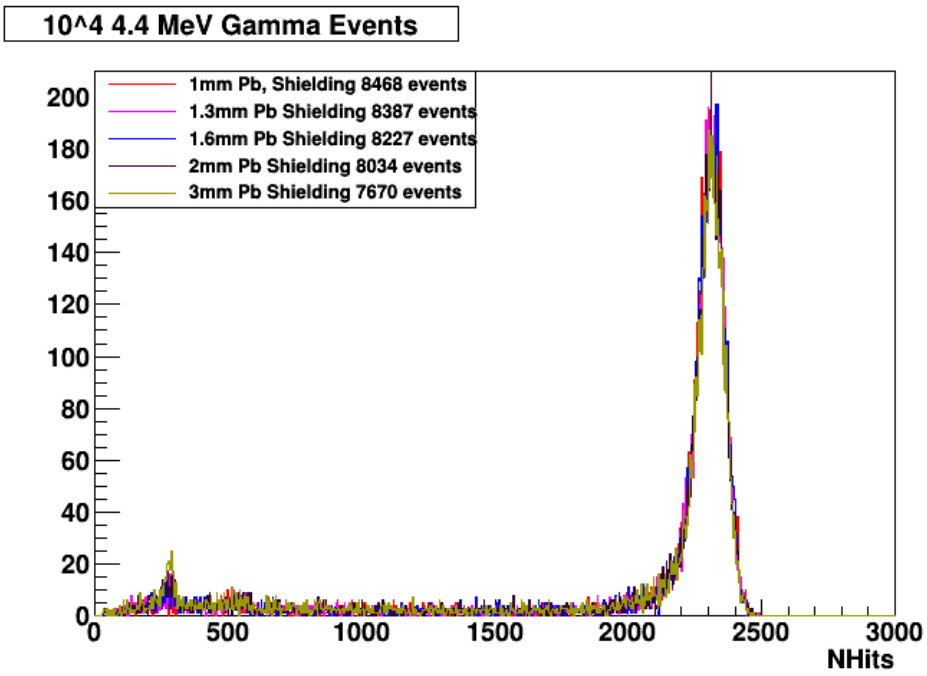

Figure 4.8: 10^4 events of 4.4 MeV γ for 1, 1.3, 1.6, 2, 3 mm of lead shielding. The legend shows number of triggers within the range of $1900 \rightarrow 2500$ NHits.

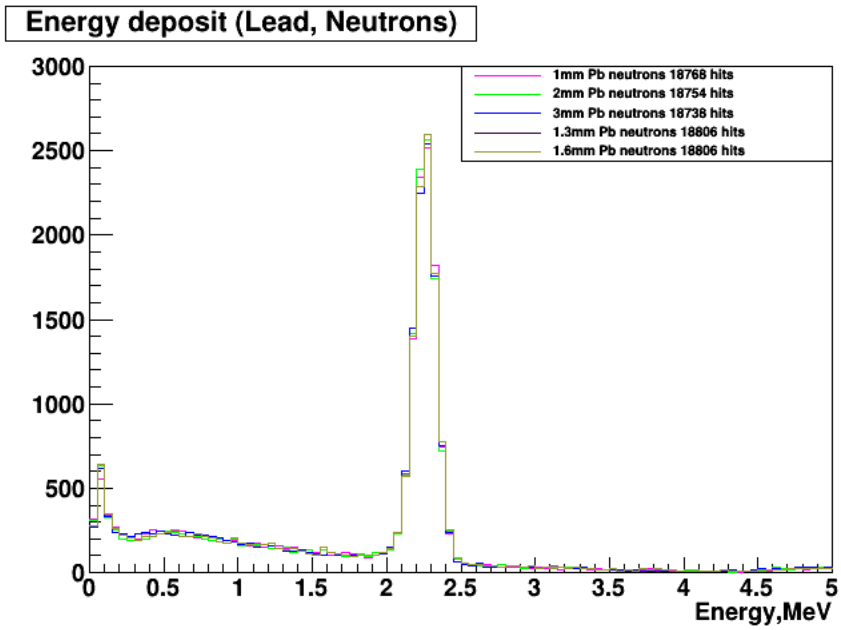

Figure 4.9: The energy fit using scintillator fitter for 1, 1.3, 1.6, 2 and 3 mm of lead shielding.

All of the shielding conclusions are going to be based on the Nhit distribution plots, such as Figure 4.9, because the scintillator fitter is still being developed. This is discussed later in Section 5.1.

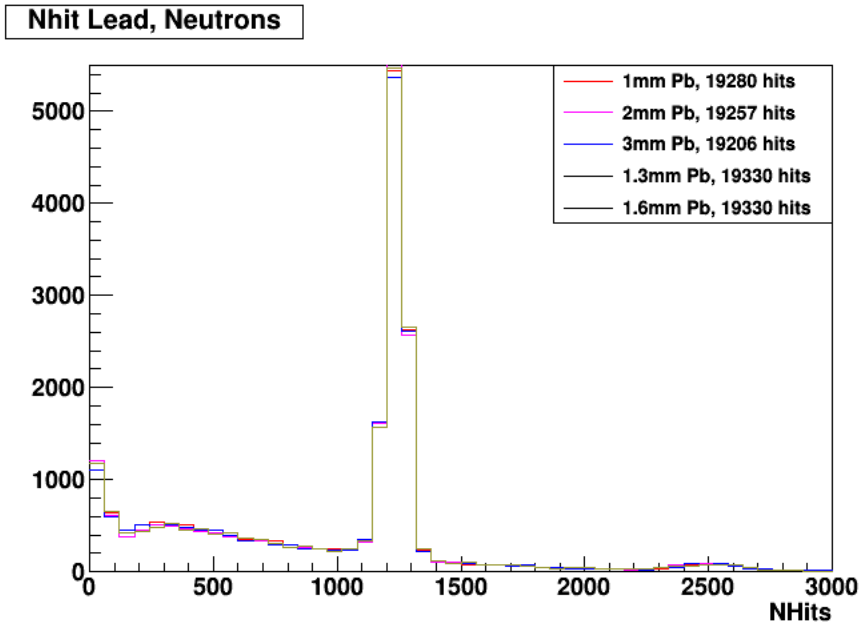

Figure 4.10: The NHit for 1,2,3 mm of lead shielding.

Figure 4.11 shows the breakdown of the separate NHit "triggers" of 10000 neutron events going

through 1mm of lead. The 0th trigger represents the first reconstructed event associated with a simulated particle. The 0th trigger shows the thermalisation of neutron before it gets captured along with some captures of some lower energy neutrons. The 1st trigger is the main neutron capture event peak. The 2nd and "the rest" shows some secondary triggers.

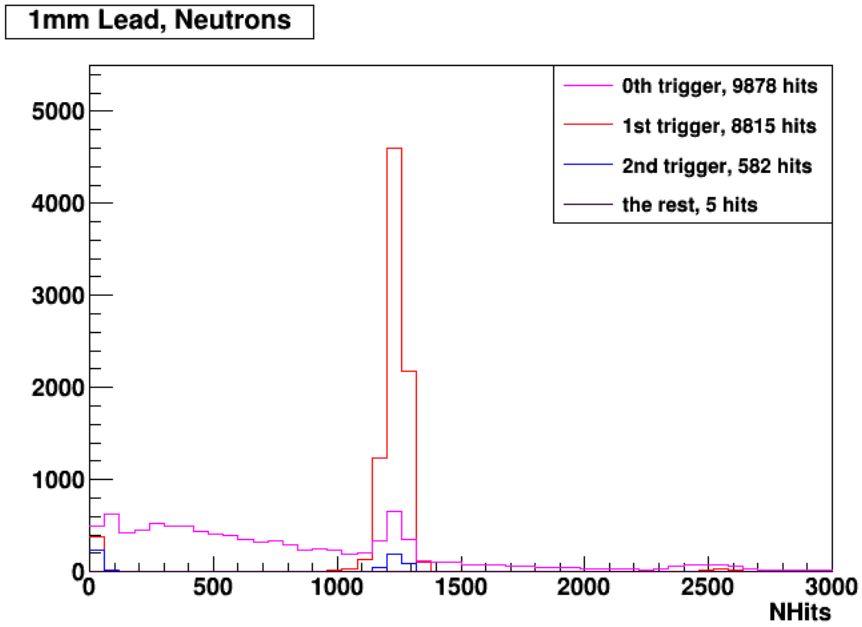

Figure 4.11: The breakdown of the separate NHit "triggers" of 10000 neutron events going through 1mm of lead. The 0th trigger represents the first reconstructed event associated with a simulated particle. Here, the 0th trigger corresponds to the thermalisation of a neutron before it gets captured. The 1st trigger is the neutron capture event peak.

4.2.4 Results

The plots for the $1 \rightarrow 3$ mm thicknesses of lead are summarised in the table Table 4.2. It shows the percentage of gammas and neutrons that are going through the different thicknesses of lead. For the determination of the amount of shielding against 59.5 keV gamma events, the probability of the low energy γ to coincide with the neutron event at the same acquisition window was estimated. As it is visible from Figure 4.7 with the 2 mm of lead shielding, only one 59.5 keV γ penetrates the shielding out of the 10^6 simulated events. This gives the rate of low energy γ to be approximately 1 for every neutron produced as with every neutron there is 10^6 59.5 keV γ without the shielding. These two events are uncorrelated as the low energy gammas come from the ^{241}Am decays into α and the neutron comes from the ^{9}Be(α,n)^{12}C reaction. While seeing a neutron event, if the very

generous 400 ns trigger window is opened having the average time interval between events of about 10 ms , the probability to have 59.5 keV event inside the neutron trigger window is:

$$P = \frac{0.4\mu\text{s}}{10000\mu\text{s}} = 0.4 \times 10^{-4} \tag{4.3}$$

The probability being this low shows that the 2 mm of lead provides good enough shielding for the detector to no longer be blinded as well as for the low energy γ not to interpose onto the neutron event.

Thickness	59 keV	4.4 MeV	Neutrons
1 mm	0.039%	84.68%	88.15%
1.3 mm	0.0082%	83.87%	88.21%
1.6 mm	0.0011%	82.27%	88.21%
2 mm	0.0001%	80.34%	87.83%
3 mm	0.0000%	76.70%	87.37%

Table 4.2: The % of gammas and neutrons penetrating the different thicknesses of lead.

The finalised schematics for the new AmBe source shielding geometry are shown in Figure 4.12, Figure 4.13 and Figure 4.14. The original AmBe source container (purple) is surrounded by 2 mm of lead shielding (blue), leaving some space on the sides for the screws that extend out of the original source containment. The source is encapsulated in additional layer of stainless steel (green), because lead is not a compatible material with LAB. The top of the container has a thicker layer of lead accounting for the screws needed to attach the source to the source connector. The source connector is made out of stainless steel and will attach to the teflon stem using three stainless steel screws. The screws and screw holes are left out if the simulation geometry for simplification, as they are same material as the connector and would not make a big difference for the analysis simulations.

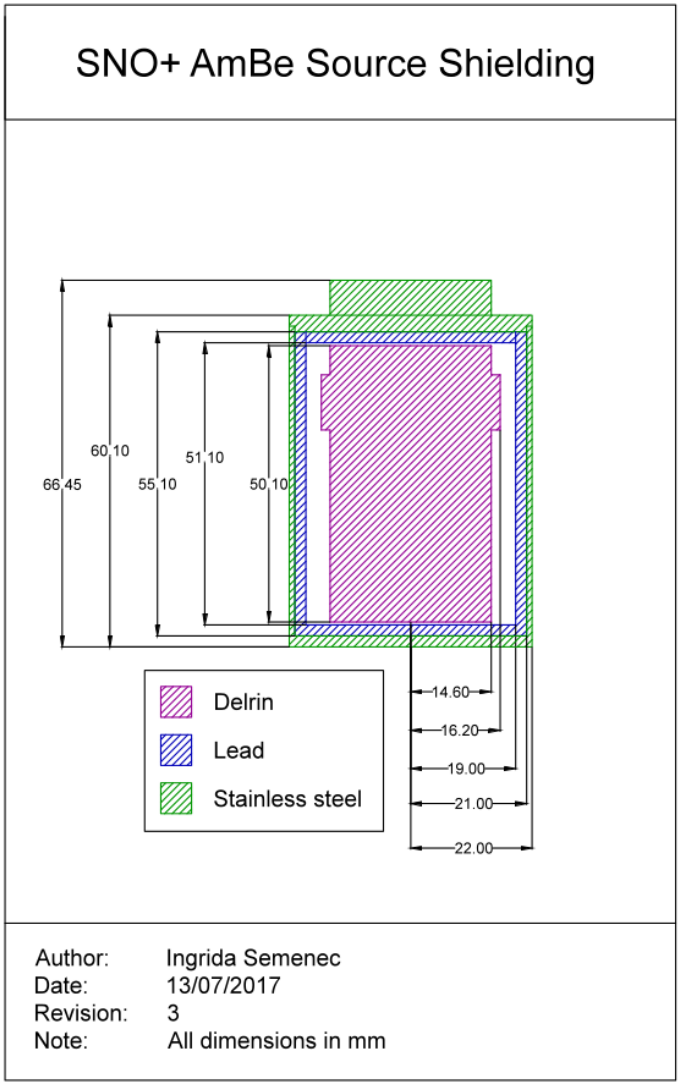

Figure 4.12: The third revision of the AmBe source shielding cross-section. Layers account for the spacing of screws and connections for the stem attachment and the original source screw placement. The purple depicts the original AmBe source container, with the 2 mm of lead shielding in blue and the additional stainless steel encapsulation (green). The additional millimeter of stainless steel added to the bottom of container for the structual integrity. The source connector to the stem is also made out of stainless steel.

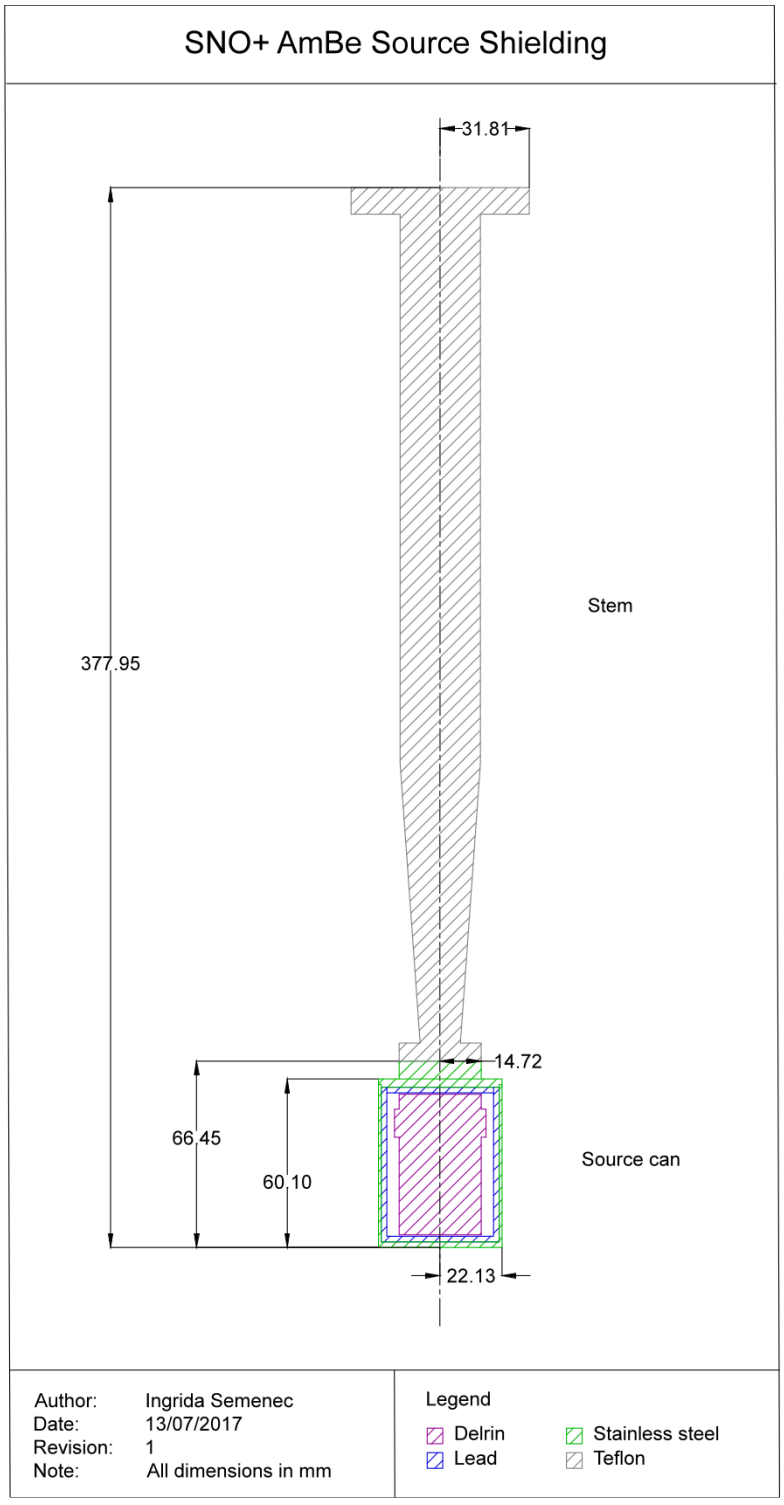

Figure 4.13: The finalised schematic of the AmBe source geometry including the stem. The measurements and layers are shown as in the latest geometry file for the AmBe source simulations.

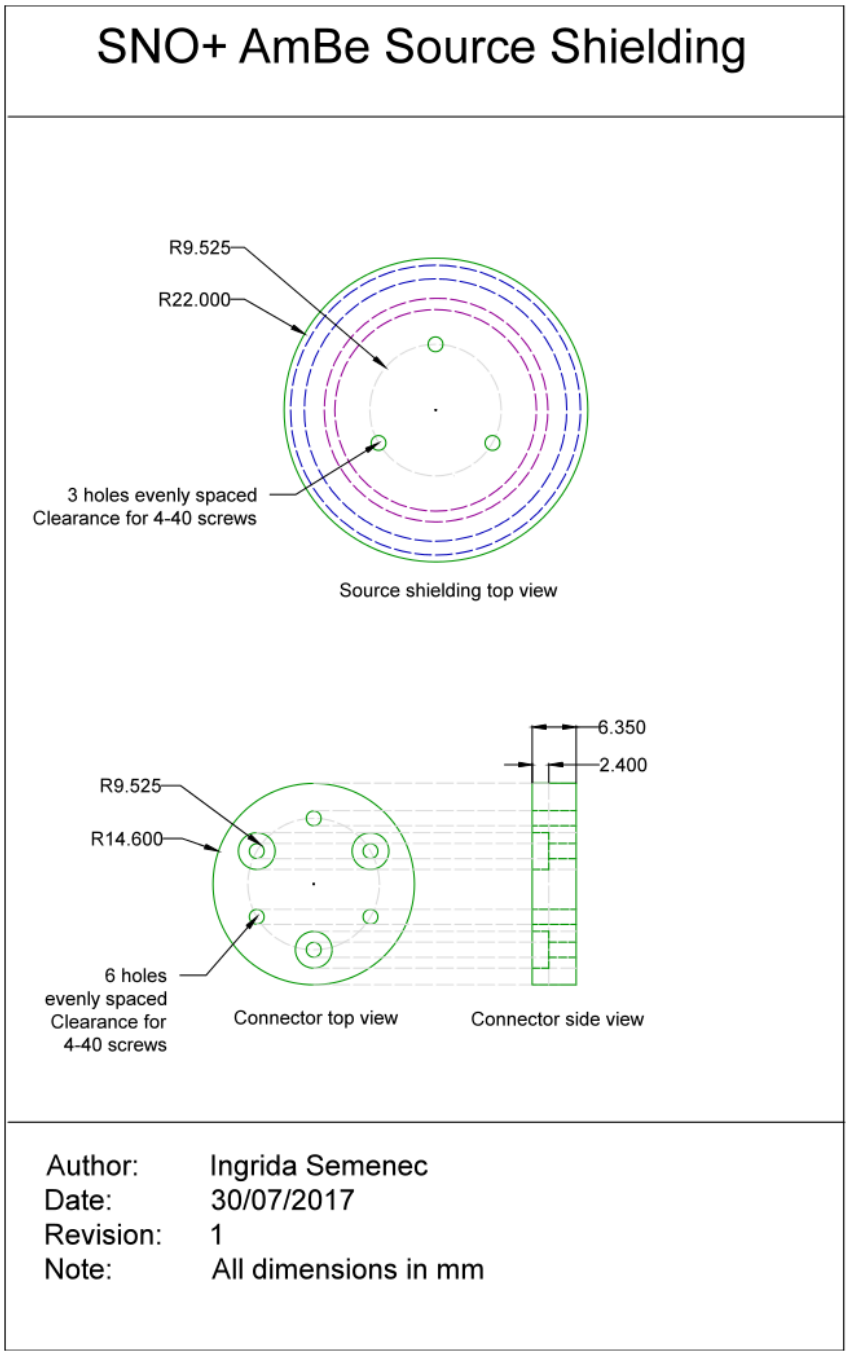

Figure 4.14: The finalised schematic of the AmBe source connector geometry.

Chapter 5

Neutron Source Analysis

5.1 Scintillator Fitter

The scintillator fitter "energy fit" was used in some parts of the analysis to see if the AmBe spectrum peaks lay at the expected energies. To compare the true energy to the reconstructed energy provided by the scintillator fitter, the plot of the MC true energy versus the reconstructed energy is shown in Figure 5.1. Here,"true spectra" indicates the true neutron energy distributions of the MC events. As it has been shown in Figure 4.1 there is correlation between the neutron energies and the produced gamma energies. Therefore it is important to have a accurate reconstruction of the neutron energy.

The reconstructed energy provided by the EV branch is the summed deposited energy for all particles in a single event (it does not provide the deposited energy of each individual particle). Therefore, to make a valid comparison, it was necessary to obtain the total true deposited energy in MC, summing over all particles that were reconstructed.

The variation between the true and reconstructed data is very small. The reason for the two outlier events is unknown. However, it was reported to the people responsible for the development of the fitter and it will be resolved. The fractional error of the energy fit is calculated by Equation 5.1 shown in Figure 5.2.

$$E_{\text{err}} = \frac{E_{\text{reconstructed}} - E_{\text{true}}}{E_{\text{true}}} \tag{5.1}$$

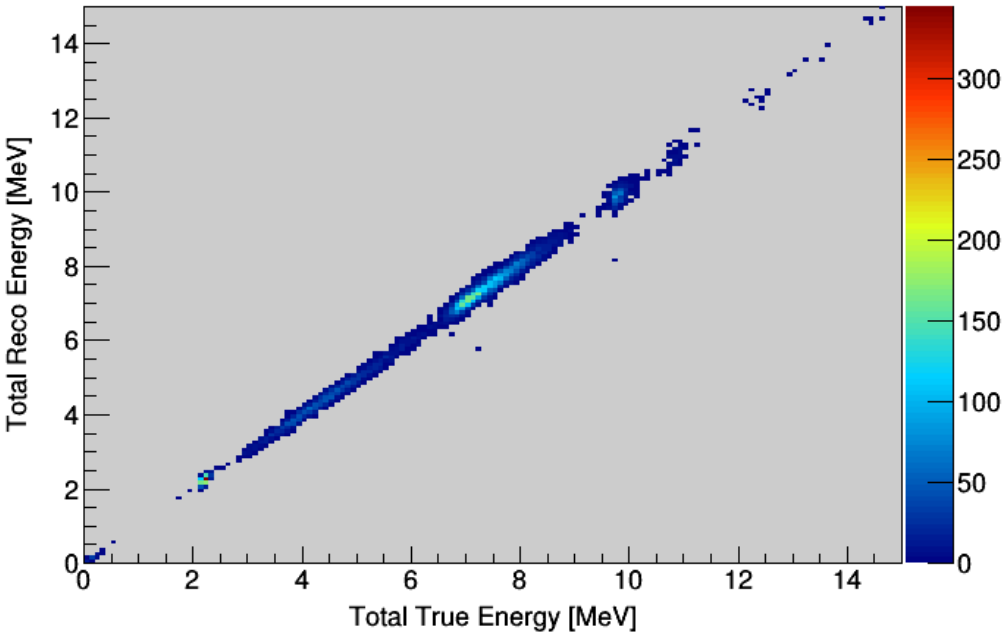

Figure 5.1: The MC true versus EV reconstructed energy from the scintillator fitter for total deposited energy within a simulated event. The narrow linear trend shows strong correlation between the true and reconstructed energy.

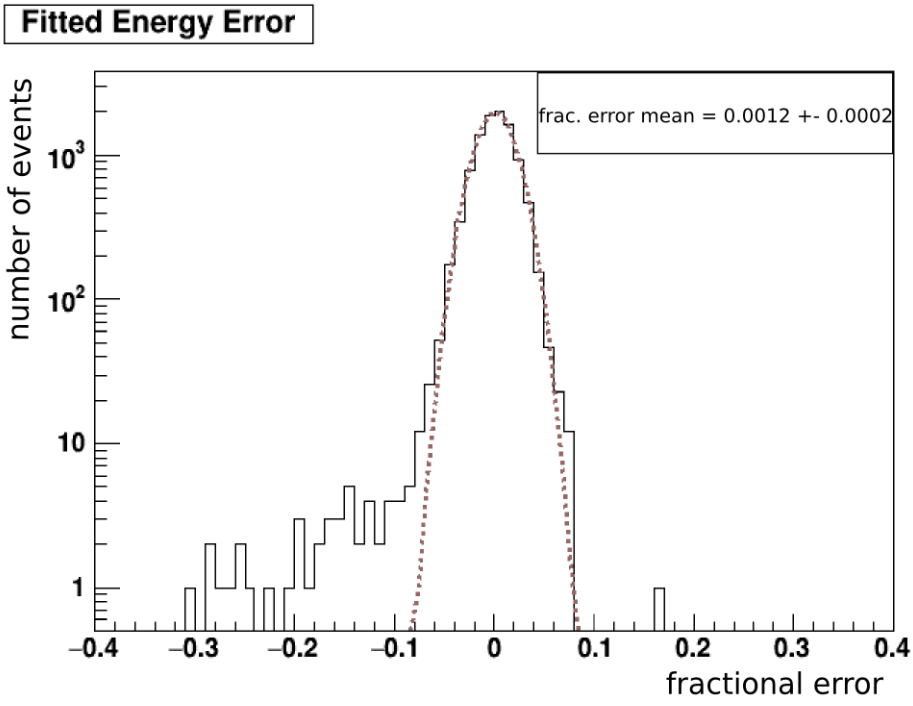

Figure 5.2: The fractional error of MC true versus the EV reconstructed energy. Slight bias to the negative values shows that reconstructed energy tends to be lower than true.

The fractional error plot shows the slight bias towards the reconstructed energy tending to be lower than the true MC energy deposited by the event. However, the error is small and the scintfitter energy reconstruction seems to be substantially accurate. The mean pf the fractional error is $(1.2\pm0.2)^{-3}$ which is very small. The algorithms for the fitter are susceptible to be modified once the scintillator properties within the detector are known better, the tests done so far indicate an unbiased energy reconstruction with a resolution of 3% [52] . Even though the energy fit seems to be reliable, since the scintillator fitter is still being developed, it is only used as a reference for some energies within this thesis.

5.2 Energy peak dependence on source position

The AmBe source will be deployed in various positions inside the detector. Taking calibration data at varying positions will give an understanding of the event position dependency in detector response. Therefore, the MC simulations with different positions have to be investigated before the deployment of the source.

The AmBe source was simulated along the X, Y and Z axes at ±1, ±2, ±3, ±4, and ±5 meters away from the center of the detector. The center position was simulated as well.

A comparison was also made of the 2.2 MeV neutron capture peak position in NHit (at different X, Y, and Z positions) between the "perfect" configuration of PMTs (i.e. all PMTs being online) and the detector PMT status taken from run 15060 (see Figure 5.5, Figure 5.6, Figure 5.4). Run 15060 has 591 offline PMTs. The AmBe spectrum generated at different Z positions is shown in Figure 5.3. The main neutron capture peak was then fitted using gaussian fit.

As expected the peak NHit value increases with larger distance from the detector center. The Nhits follows approximately a $\frac{1}{r^2}$ trend as you go further from the photo detection surface, clearly visible in Figure 5.5, Figure 5.6, Figure 5.4. The PMTs that are at shorter distances from the event have a larger probability to trigger because the photons have lesser probability to be absorbed by the LAB. However, when the event happens too close to the PMTs the smaller region of PMTs gets oversaturated, hence the overall Nhit drops at ±5 meters away from the center. Also there is a bigger probability for gammas to leave the detector before depositing the full energy, which also affects the NHits (Figure 5.3).

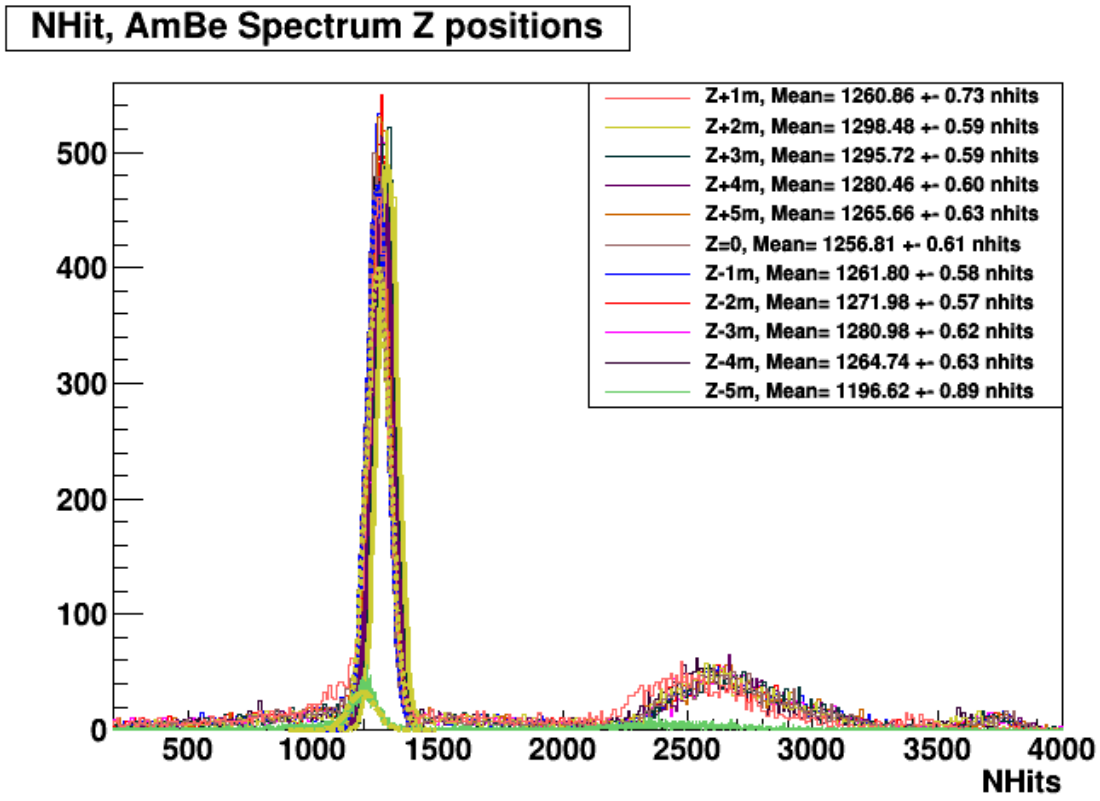

Figure 5.3: NHit plot of the AmBe source spectrum, source simulated at different Z positions inside the detector with 0 offline PMTs. The plot shows the neutron capture peaks between 1000 to 1500 NHit and the 4.4 MeV gamma peak around 2200 to 1400 NHit. The plot illustrates the way sharp neutron capture peak was fitted to get the mean number of hits. (5000 events simulated)

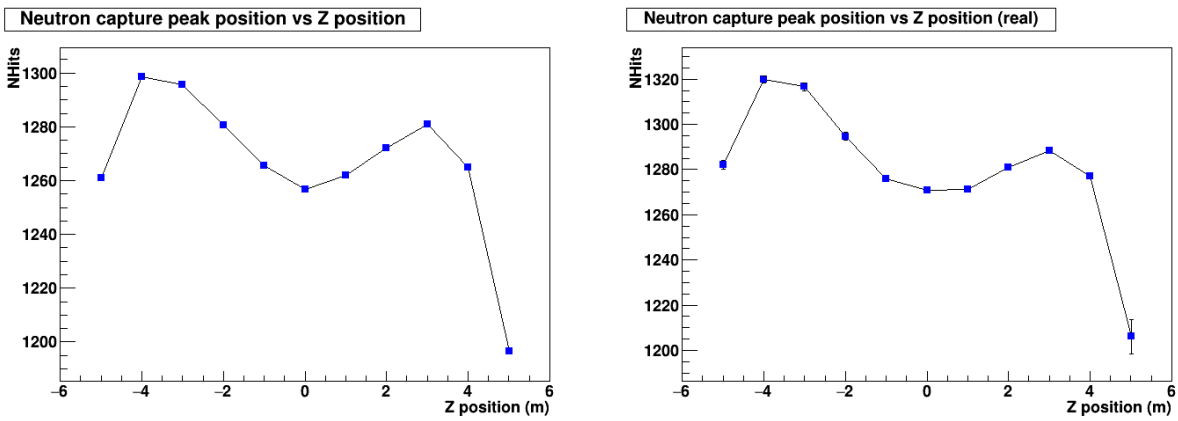

(a) "Perfect" PMTs

(b) run 15060 PMTs

Figure 5.4: Neutron capture peak values in Nhit relative to the Z axis source positions inside of the detector.

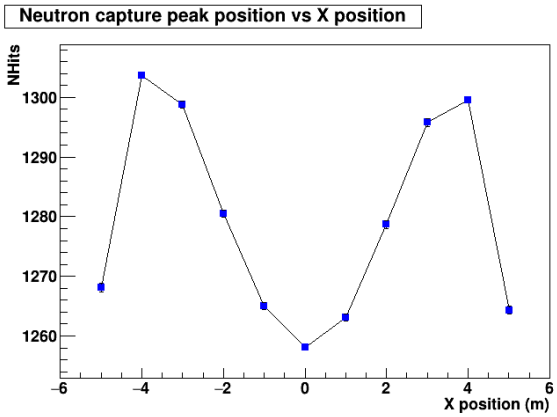

(a) "Perfect" PMTs

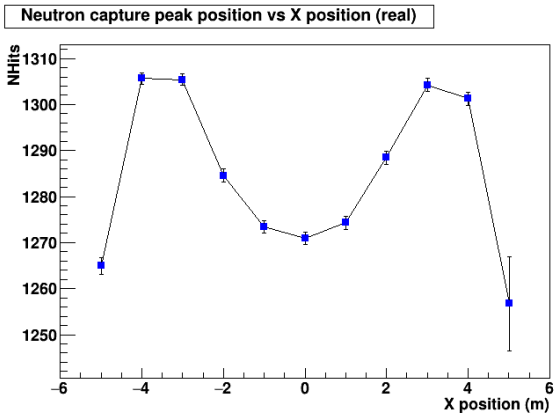

(b) run 15060 PMTs

Figure 5.5: Neutron capture peak values in Nhit relative to the X axis source positions inside of the detector.

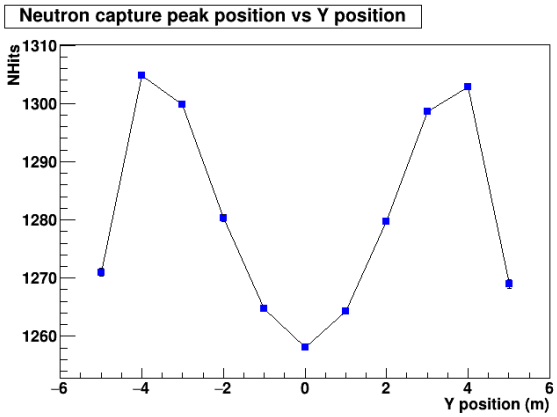

(a) "Perfect" PMTs

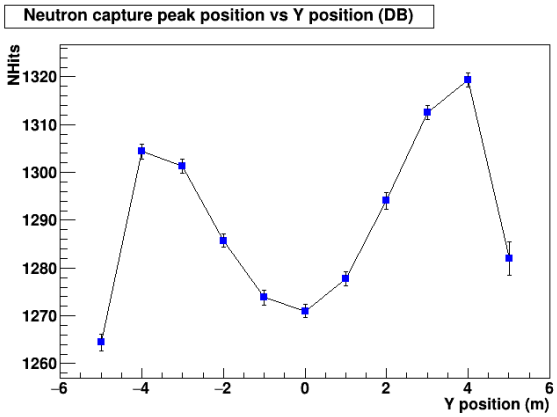

(b) run 15060 PMTs

Figure 5.6: Neutron capture peak values in Nhit relative to the Y axis source positions inside of the detector.

The peak position shifts along the X and Y axes are symmetric with the respect to the center, Figure 5.5b and Figure 5.6b. The difference along Z axis is asymmetrical. Due to the Neck of the detector having less PMTs the peak position in NHits is smaller at the positive Z axis positions. Comparing the overall Nhits for "perfect" PMT configuration to the one taken from run 15060 we can see that the Nhits are larger for the run 15060. This is counter-intuitive as less PMTs should mean we see less Nhits. The larger number of hits could be due to the possible overcompensation by a correction applied within MC simulation. However, solving this issue is out of the scope of this thesis and does not affect the results demonstrated.

5.3 Shadowing

The scintillation light produced by γ's coming from the source scatters in all directions and some of it can be absorbed by the source container or other source components. This effect is called shadowing and it contributes to some loss in Nhits. Therefore, when adding extra layers of shielding and changing the geometry of the calibration source, it is important to consider the shadowing effects of the components.

Different combinations of the source components were simulated to find out the shadowing effects of the existing AmBe container, the new added shielding, and the stem.

AmBe scenario	Neutron peak position (Nhit)	FWHM (Nhit)
Point source	1227.93 ± 0.70	49.16 ± 0.50
Old container	1215.78 ± 0.75	53.96 ± 0.69
Old container (no stem)	1224.04 ± 0.71	50.99 ± 0.57
With shielding	1214.50 ± 0.76	54.13 ± 0.72
With shielding (no stem)	1223.69 ± 0.71	51.39 ± 0.58

Table 5.1: The shadowing effects of the AmBe source container components on the neutron capture peak in AmBe source spectrum.

The comparison of the AmBe source 2.2 MeV neutron capture and 4.4 MeV γ peaks in different scenarios is summarised in Table 5.1 and Table 5.2. The peaks were fitted with a gaussian as shown in Figure 5.7. From the fit, the peak position in Nhit and the FWHM (full width half maximum) were taken to indicate the change in the loss of Nhit due to shadowing and any changes in the spread of the peak. For both neutron and gamma peaks, the Nhit is highest with the simulation

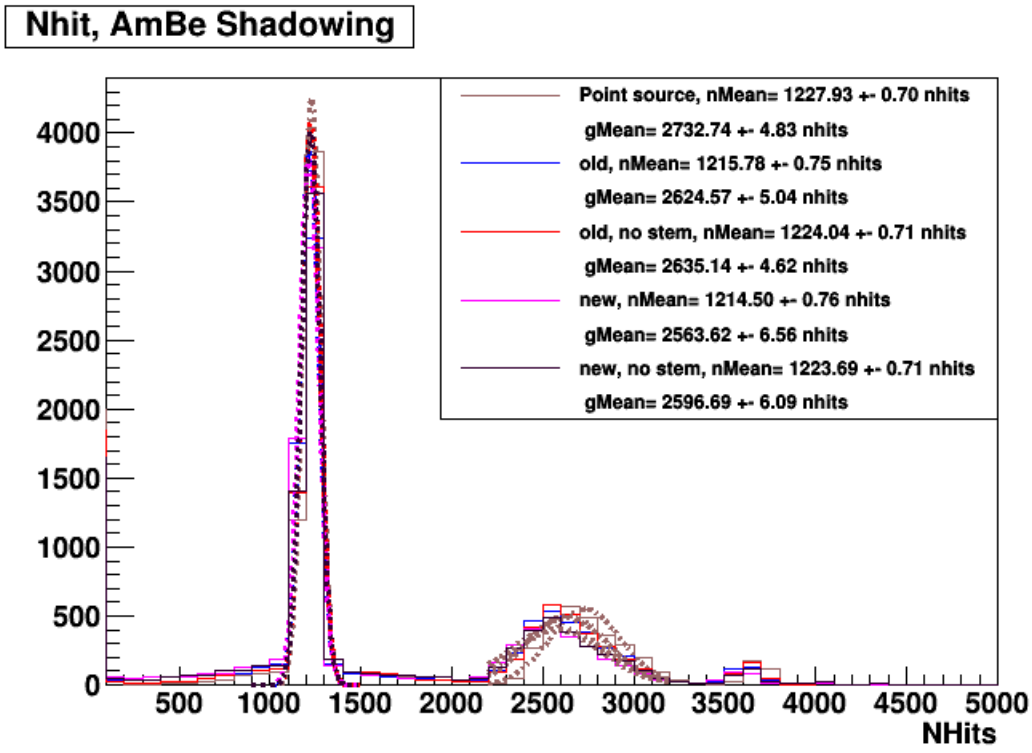

Figure 5.7: The Nhit distributions of AmBe spectrum with different shielding scenarios. 5000 events were simulated for each case. The neutron capture and 4.4 MeV γ peaks are fitted with gaussian functions to get the peak positions in Nhit shown in the legend.

AmBe scenario	4.4 MeV γ peak position (Nhit)	FWHM (Nhit)
Point source	2732.74 ± 4.83	195.26 ± 3.32
Old container	2624.57 ± 5.04	235.84 ± 4.84
Old container (no stem)	2635.14 ± 4.62	219.17 ± 4.44
With shielding	2563.62 ± 6.56	256.19 ± 6.84
With shielding (no stem)	2596.69 ± 6.09	254.39 ± 6.17

Table 5.2: The shadowing effects of the AmBe source container components on the 4.4 MeV γ peak in the AmBe source spectrum.

of AmBe as a point source with no container. In this case, there are no components to absorb neutrons or scintillation light.

For the neutron peak position in Nhit, the difference between the point source scenario and two scenarios with container (no stem) is that the Nhit drops by approximately 0.32%. With the stem, the difference is approximately 0.98%. The difference between the old containment of AmBe and the addition of 2 mm of lead surrounded by 1 mm of stainless steel is very small. The additional shielding drops the Nhit by approximately 0.03%, which is within statistical uncertainty in the peak positions given in Table 5.1. Thus, the added shielding effects are not significantly large.

For the 4.4 MeV gamma peak positions in Nhit, the uncertainties are larger due to the peak having a larger spread, as shown in Table 5.2. The difference in Nhit between the point source scenario and the old container scenario (no stem) is 3.57% lower, whereas the difference to the container with shielding is 4.97% lower. The larger shift in Nhit can also be explained by the effect of γ losing more energy while going through additional shielding unlike the neutron capture peak, which requires neutrons to thermalise after leaving the shielding to be captured to produce a much sharper peak. Therefore, the spread of the γ peak also increases, with gammas losing more energy and extra light being absorbed by the source components.

5.4 Tagged event efficiency

The understanding of the neutron capture efficiency within the detector will lead to an estimated efficiency of the detection of anti-neutrino events. As discussed before in Section 1.5, the anti-neutrino events are detected via inverse beta decay, which produces a positron and a neutron. Detecting the neutron coming from this event allows the anti-neutrino event tagging and energy reconstruction. The AmBe neutron source deployment will give insight into the detector response to neutron capture events.

The measured activity of the AmBe source is 68.7 n/s [46]. The 30 minutes of an AmBe calibration run would give approximately 10^5 neutron events. However, using γ as a tag for the neutron reduces the efficiency of tagged neutron events because a 4.4 MeV gamma is only created 60% of the time with the neutron. Therefore, the rate of tagged neutron events becomes 41.44 n/s. With the added shielding, the number of neutrons that can be tagged is less due to the loss of

4.4 MeV γ tags. With 2 mm of lead plus 1 mm of stainless steel shielding, approximately 19.66% of 4.4 MeV γ are lost, shown in Table 4.2. This leaves the tagged neutron event efficiency to be around 33.30 n/s. The estimated number of events to get the precision of 1% is 10000 this equates to approximately 5 minute of a source deployment run.

The neutron capture efficiency is the ratio of observed neutron capture events after selection cuts to the total number of true neutron capture events in which a 4.4 MeV gamma was also tagged (Equation 5.2).

$$\epsilon = \frac{\text{\# of n-captures observed in detector}}{\text{\# of true n-captures with the 4.4 MeV tag}} \tag{5.2}$$

The logic flow for the selection of the true number of the neutron capture events within the detector is shown in Figure 5.9. The script checks if the neutron was generated with 4.4 MeV gamma and if the neutron was captured inside the inner AV volume. For the observed number of neutron capture events from the reconstructed MC data, the script checks the number of NHits that would equate to 4.4 MeV gamma in the generated AmBe spectrum and then checks for the number of NHits for the neutron capture peak which is 2.2 MeV gamma peak in the AmBe spectrum (Figure 5.7, as shown in Figure 5.10. Then for the selection of the event, the time and order of both events has to be compared. When producing neutron and gamma in coincidence, the generator technically produces the gamma particle first. The time of the neutron capture event minus the time of the gamma tag event must then be positive. Also, the events must be within a reasonable time for neutron capture event to happen and they must come from the same generated entry.

Out of 9349 events simulated, 5528 neutrons came with 4.4 MeV gamma tag and was captured inside the inner AV volume. To do the time selection cut, the MC truth neutron capture time was compared to the true capture time, shown in Figure 5.8. The reconstructed neutron capture time was fitted to function $N(t) = N_0 e^{-t/\tau}$, where τ is the neutron capture mean time. The capture mean time from the fit is $204.95 \pm 3.30 \mu$s. With the time selection cut being approximately three times the neutron capture mean time ($\approx 620 \mu$s), the neutron capture efficiency is 74.22%. The time cut can be later optimised, while considering all of the backgrounds. The possible backgrounds for AmBe neutron capture events are the neutrons coming from external sources, such as cosmic

muons. Neutrons can also be produced by the decay of ^{210}Po leached from the AV, which leads to $\alpha + {}^{13}\mathrm{C} \rightarrow {}^{16}\mathrm{O} + \mathrm{n}$ reaction. However, these backgrounds are negligible compared to the signal produced by the source. The average rate of cosmic muons is 3 events per hour and the estimated number of events from ^{13}C(α,n) reactions is only 13 events over 6 months of data taking in the liquid scintillator [53].

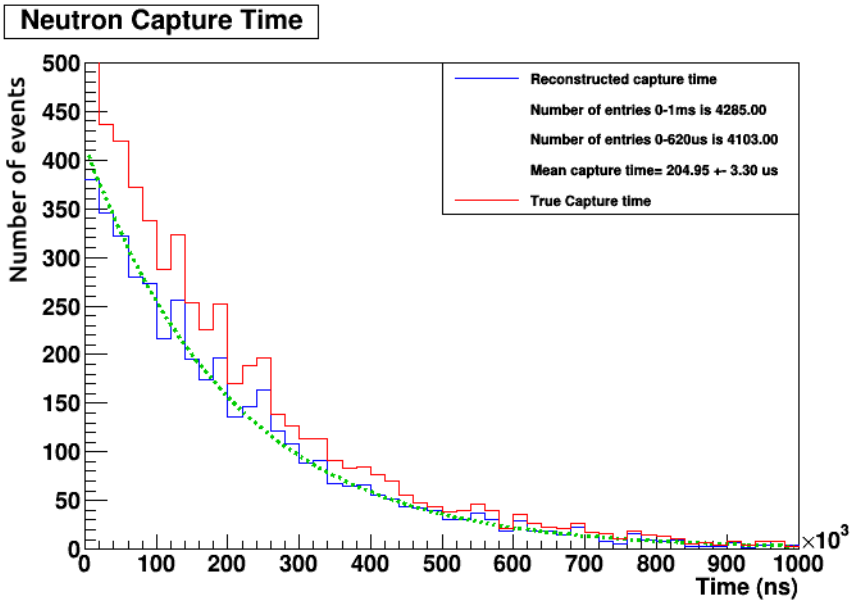

Figure 5.8: The neutron capture time comparison between the MC truth versus reconstructed time. The reconstructed time was fitted with an inverse exponential to find the mean neutron capture time (dotted green line).

For proper reconstructed neutron capture event selection, the ΔR cut should also be applied. Radial cut is important for the rejection of the background events that would be out of realistic range for neutron capture event. The Figure 5.11 shows the distance of the neutron capture event inside the inner AV from the generated 4.4 MeV gamma tag using the MC truth information. The reconstructed capture distance can be seen while using the reconstruction fitter information and getting the fitted position of the neutron capture vertex. However, the current fitter is not complete and is being further developed, therefore the radial cut was not used in this thesis. Once the vertex fitter can be trusted, the truth and reconstructed information should be compared for the optimal cut on the neutron capture event distance from the source.

The neutron capture efficiency after the time cut is 74.22%. For the actual calibration, the additional distance cut should be applied. Both of these cuts should then be optimised in accordance

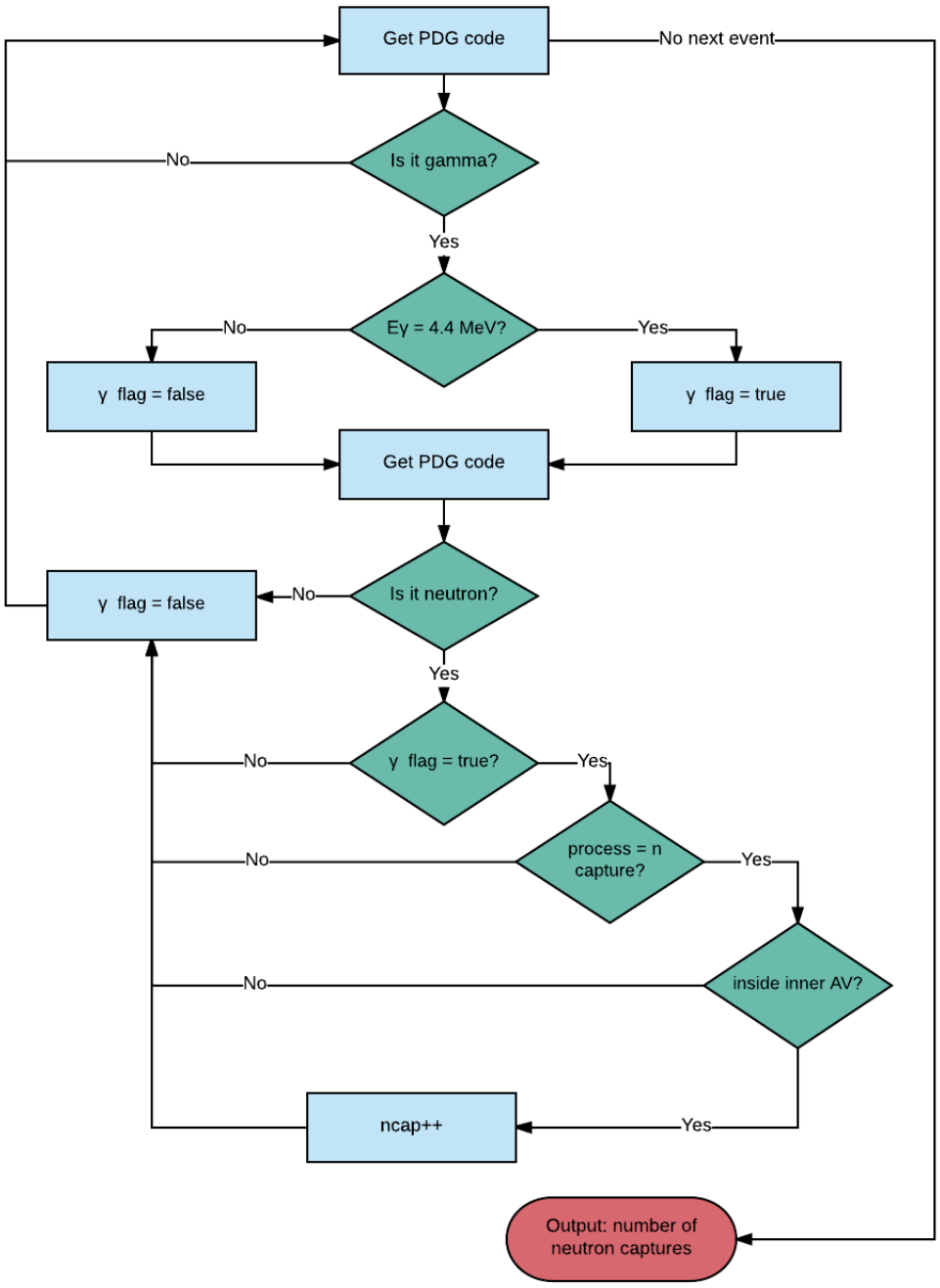

Figure 5.9: The neutron capture event selection using MC truth information.

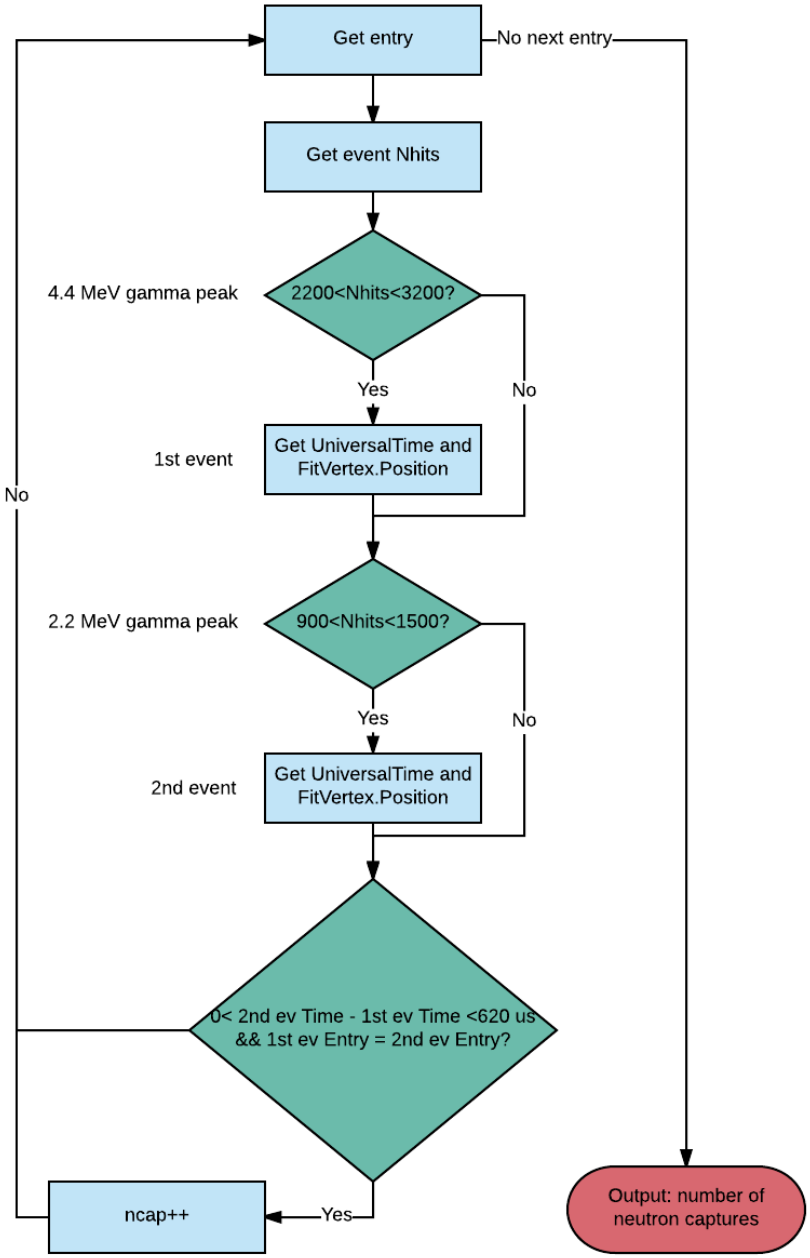

Figure 5.10: The neutron capture event selection using reconstructed event information.

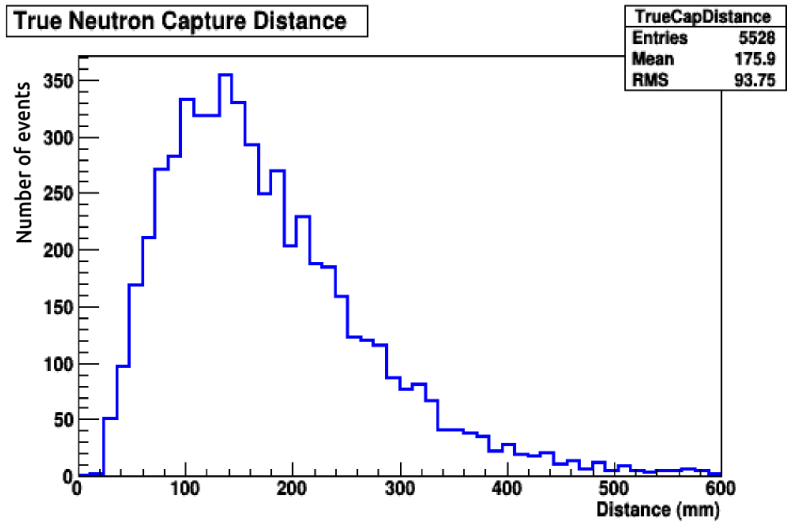

Figure 5.11: The neutron capture event distance from the source using MC truth information.

to the backgrounds that are seen in the detector. The estimation of backgrounds and the cuts using the simulated backgrouns were out of scope for this thesis. The neutron capture event detection efficiency is crucial for the computation of the anti-neutrino event detection efficiency for SNO+.

Chapter 6

Conclusions

The SNO+ experiment provides a great opportunity to study low energy solar neutrinos, reactor anti-neutrinos, geo anti-neutrinos, and supernova neutrinos. These studies will provide a valuable insight into several different topics of neutrino, astro and geo physics. The tellurium-loaded scintillator phase will be able to search for neutrinoless double beta decay. This would provide an insight to the Dirac or Majorana nature of the neutrino, which is one of the most sought after answers in neutrino physics at the current time.

The AmBe calibration source is an esential part of the scintillator phase calibration of neutron capture efficiency. The original AmBe source had to be refurbished with additional shielding, given the wider energy resolution range of the scintillator. The new source design (Figure 4.12) includes 2 mm of lead as a shielding material against 59.5 keV x-rays produced by the α decays from ^{241}Am (Section 4.2). Additionally, the source and lead are encapsulated in a layer of stainless steel, to make the source compatible and safe to use inside the detector. Alongside neutrons, the AmBe source produces 4.4 MeV gammas used as a neutron event tag. With the new encapsulation, only one of the 10^6 simulated 59.5 keV γ events escapes the source. This makes the probabilty of the low energy gamma event to coincide with the neutron event only approximately 0.4×10^{-4}, which is very low. With this new encapsulation, 19.66% of 4.4 MeV γ are lost. This can be compensated by leaving the source inside the detector for longer periods of time. Even though the activity of the AmBe source is 68.7 n/s, with all the additional shielding, the tagged neutron event efficiency is estimated to be 33.30 n/s. To get the precision of 1% the estimated number of events is 10000 neutrons, which equates to approximately 5 minute source deployment run for every position inside

the detector. The short amount of time per position inside the detector allows the source to be deployed in multiple positions during an assigned calibration shift.

The AmBe source will be deployed in various positions inside the detector. The dependence of neutron capture and 4.4 MeV gamma peak positions (in Nhit) to the source deployement positions were studied in Section 5.2. The peak NHit values increases with larger distance from the detector center. The peak position shifts along the X and Y axes are symmetric, relatively to detector's center, Figure 5.5b and Figure 5.6b. The difference along Z axis is asymmetrical. Due to the Neck of the detector having less PMTs, the peak position in Nhits is smaller at the positive Z axis positions as expected.

Since parts made out of dense materials were added to the calibration source, the shadowing effects were also inspected. It was found that the added shielding effects are not significantly large as shown in Section 5.3. The new shielding and encapsulation drops the fitted Nhit value of the neutron capture peak in the AmBe spectrum by approximatelly 0.03%.

From the MC simulations of the AmBe source the estimated neutron capture event detection efficiency is 74.22%. Only the time cut was applied to estimate this number, the additional radial selection cut and the optimisation of cuts in accordance to the observed background rates is needed for more accurate computation of the neutron capture detection efficiency. The ^{210}Po coming from ^{210}Pb decays via alpha emmision and can create a 2.2 MeV gamma background for the neutron capture events coming from the AmBe source. However, the estimated rate of possible background events is negligible compared to the event rate coming from the AmBe source.

The design of the new AmBe neutron source is finalised and ready to be used for the source refurbishment. A basic run plan was developed and demonstrated in this thesis. The deployement of the AmBe source will provide information about neutron event reconstruction and energy reconstruction important to SNO+ physics objectives.

Appendix A

Matter Oscillations

To derive the neutrino oscillations in matter for electrons, first we need to define the Hamiltonian we have previously used in a vacuum, to then incorporate the the V_{CC} term. Expressing the Schrödinger equation in matrix form:

$$i\frac{\mathrm{d}}{\mathrm{d}t}\begin{pmatrix}\nu_1\\ \nu_2\end{pmatrix} = H\begin{pmatrix}\nu_1\\ \nu_2\end{pmatrix} = \frac{1}{2E}\begin{pmatrix}m_1^2 & 0\\ 0 & m_2^2\end{pmatrix}\begin{pmatrix}\nu_1\\ \nu_2\end{pmatrix} \tag{A.1}$$

Then for expressing Equation A.1 in terms of flavour states we use Equation A.2.

$$\begin{pmatrix}\nu_1\\ \nu_2\end{pmatrix} = U^{\dagger}\begin{pmatrix}\nu_e\\ \nu_\mu\end{pmatrix} \tag{A.2}$$

Then the Equation A.1 becomes:

$$i\frac{\mathrm{d}}{\mathrm{d}t}\begin{pmatrix}\nu_1\\ \nu_2\end{pmatrix} = H\begin{pmatrix}\nu_1\\ \nu_2\end{pmatrix} \tag{A.3}$$

$$\implies U^\dagger i\frac{\mathrm{d}}{\mathrm{d}t}\begin{pmatrix}\nu_e\\ \nu_\mu\end{pmatrix} = HU^\dagger\begin{pmatrix}\nu_e\\ \nu_\mu\end{pmatrix} \tag{A.4}$$

$$\implies i\frac{\mathrm{d}}{\mathrm{d}t}\begin{pmatrix}\nu_e\\ \nu_\mu\end{pmatrix} = UHU^\dagger\begin{pmatrix}\nu_e\\ \nu_\mu\end{pmatrix} \tag{A.5}$$

Then we can write the Hamiltonian for the flavour oscillations in vaccum as Equation A.6.

$$H_{\text{vac}} = UHU^\dagger = \frac{m_1^2+m_2^2}{4E}\begin{pmatrix}1 & 0\\ 0 & 1\end{pmatrix} + \frac{\Delta m^2}{4E}\begin{pmatrix}-\cos 2\theta & \sin 2\theta\\ \sin 2\theta & \cos 2\theta\end{pmatrix} \tag{A.6}$$

The first term of the Hamiltonian is constant (no mixing), therefore it can be neglected, giving the vacuum Hamiltonian to be:

$$\implies H_{\text{vac}} = \frac{\Delta m^2}{4E}\begin{pmatrix}-\cos 2\theta & \sin 2\theta\\ \sin 2\theta & \cos 2\theta\end{pmatrix} \tag{A.7}$$

Now to derive the oscillation probability in matter, we inlcude the V_{CC} term to the Schrödinger

equation.

$$i\frac{\mathrm{d}}{\mathrm{d}t}\begin{pmatrix}\nu_e\\ \nu_\mu\end{pmatrix} = (H_{\text{vac}} + V_{CC})\begin{pmatrix}\nu_e\\ \nu_\mu\end{pmatrix} \tag{A.8}$$

$$= \left(\frac{\Delta m^2}{4E}\begin{pmatrix}-\cos 2\theta & \sin 2\theta\\ \sin 2\theta & \cos 2\theta\end{pmatrix} + V_{CC}\begin{pmatrix}1 & 0\\ 0 & 0\end{pmatrix}\right)\begin{pmatrix}\nu_e\\ \nu_\mu\end{pmatrix} \tag{A.9}$$

$$= \left(\frac{\Delta m^2}{4E}\begin{pmatrix}-\cos 2\theta & \sin 2\theta\\ \sin 2\theta & \cos 2\theta\end{pmatrix} + V_{CC}\begin{pmatrix}1 & 0\\ 0 & -1\end{pmatrix} + V_{CC}\begin{pmatrix}1 & 0\\ 0 & 1\end{pmatrix}\right)\begin{pmatrix}\nu_e\\ \nu_\mu\end{pmatrix} \tag{A.10}$$

$$\implies H_M = \frac{\Delta m^2}{4E}\begin{pmatrix}-(\cos 2\theta - A_{CC}) & \sin 1\theta\\ \sin 1\theta & (\cos 2\theta - A_{CC})\end{pmatrix} \tag{A.11}$$

Equation A.11 shows the Hamiltonian for the 2 flavour matter oscilations, where $A_{CC} = 2\sqrt{2}G_F N_e E/\Delta m^2_{21}$. To write H_M in the same form of H_{vac} we define the parameters Δm^2_M and $\sin^2 2\theta_M$ as shown in Equation A.12 and Equation A.13 respectively.

$$\Delta m^2_M \equiv \Delta m^2_{21}\sqrt{\sin^2 2\theta + (\cos 2\theta - A_{CC})^2} \tag{A.12}$$

$$\sin^2 2\theta_M \equiv \frac{\sin^2 2\theta}{\sin^2 2\theta + (\cos 2\theta - A_{CC})^2} \tag{A.13}$$

Now the Equation A.11 becomes:

$$H_M = \frac{\Delta m^2_M}{4E}\begin{pmatrix}-\cos 2\theta_M & \sin 2\theta_M\\ \sin 2\theta_M & \cos 2\theta_M\end{pmatrix} \tag{A.14}$$

Hence the oscillation probability in matter is:

$$P^M_{\nu_\alpha \to \nu_\beta} = \sin^2 2\theta_M \sin^2\left(\frac{\Delta m^2_M}{4E}L\right) \tag{A.15}$$

A.1 Schematics

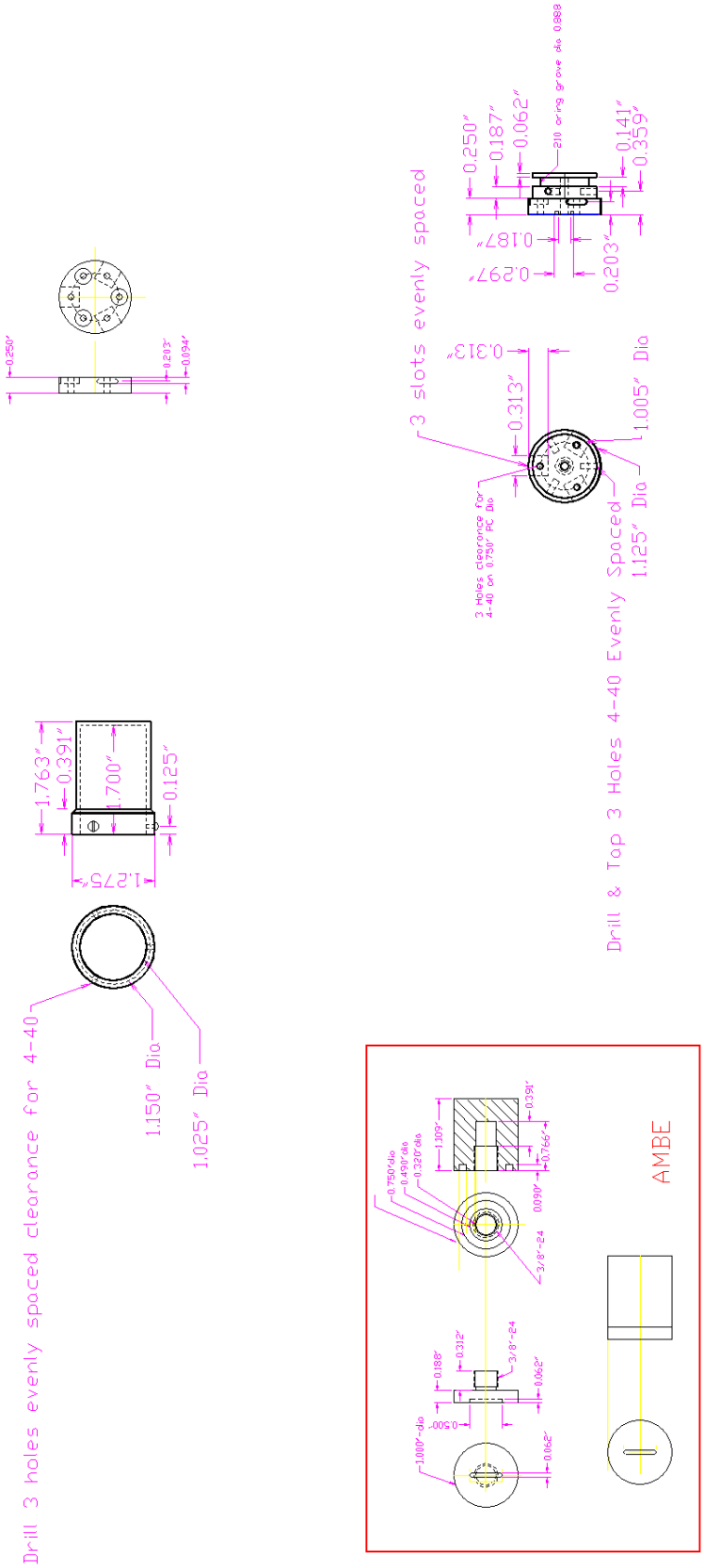

Figure A.1: The SNO AmBe schematics

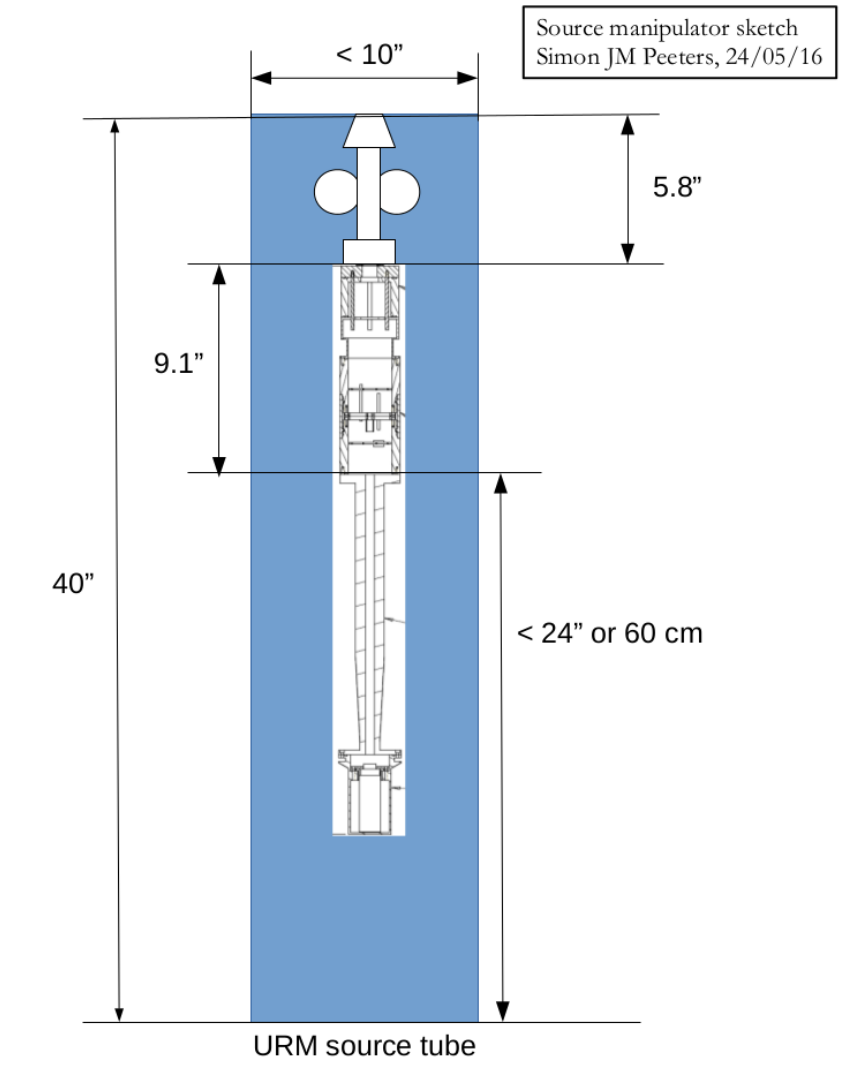

Figure A.2: The SNO+ source manipulator schematic.

Appendix B

Source Shielding plots

The simulations performed for AmBe source with additional Stainless Steel (SS), Lead (Pb) and Hevimet (hevi) shielding in scintillator. The "NHits" plots shows the number of hits we get per event simulated. There were 10000 4.4MeV and 59.5keV events simulated in the center of the detector separately.

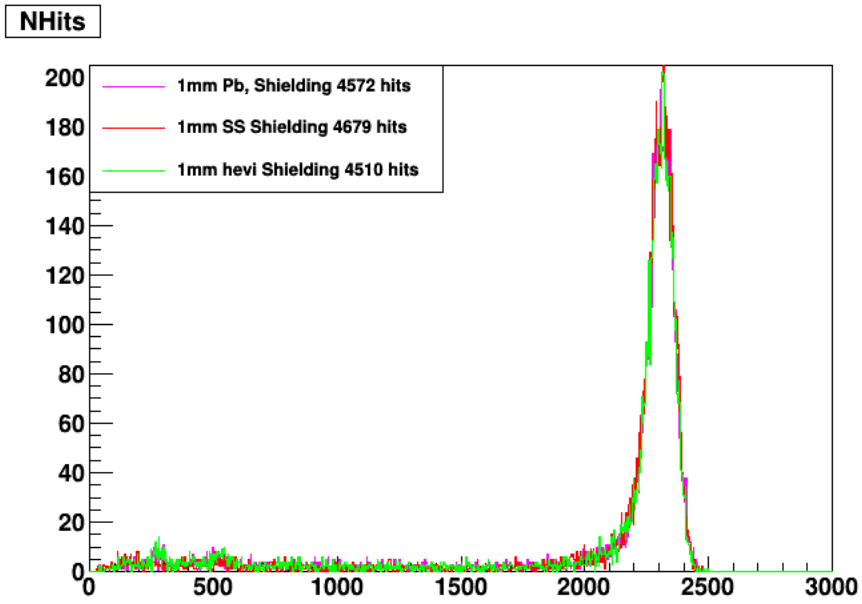

Figure B.1: The NHit distribution for 10000 4.4MeV γ events going through 1mm of lead, stainless steel and hevimet.

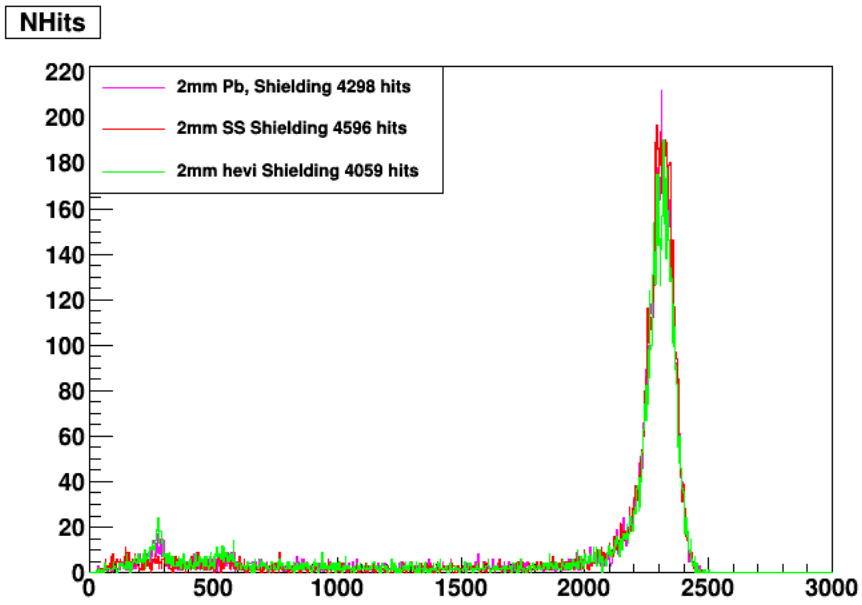

Figure B.2: The NHit distribution for 10000 4.4MeV γ events going through 2mm of lead, stainless steel and hevimet.

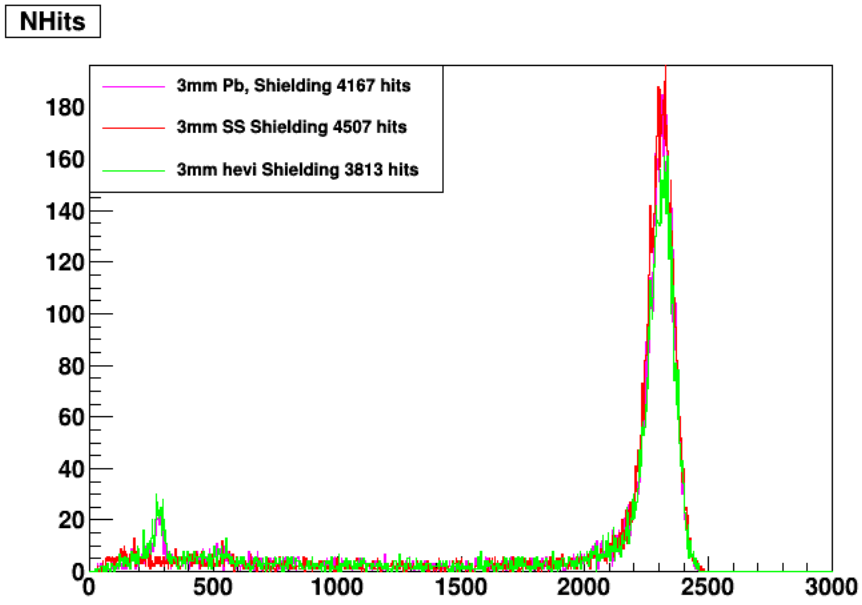

Figure B.3: The NHit distribution for 10000 4.4MeV γ events going through 3mm of lead, stainless steel and hevimet.

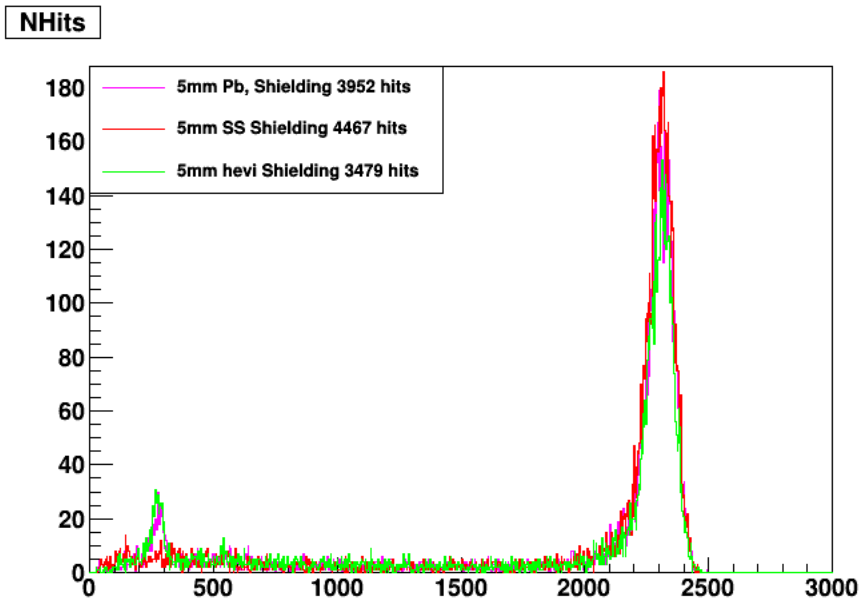

Figure B.4: The NHit distribution for 10000 4.4MeV γ events going through 5mm of lead, stainless steel and hevimet.

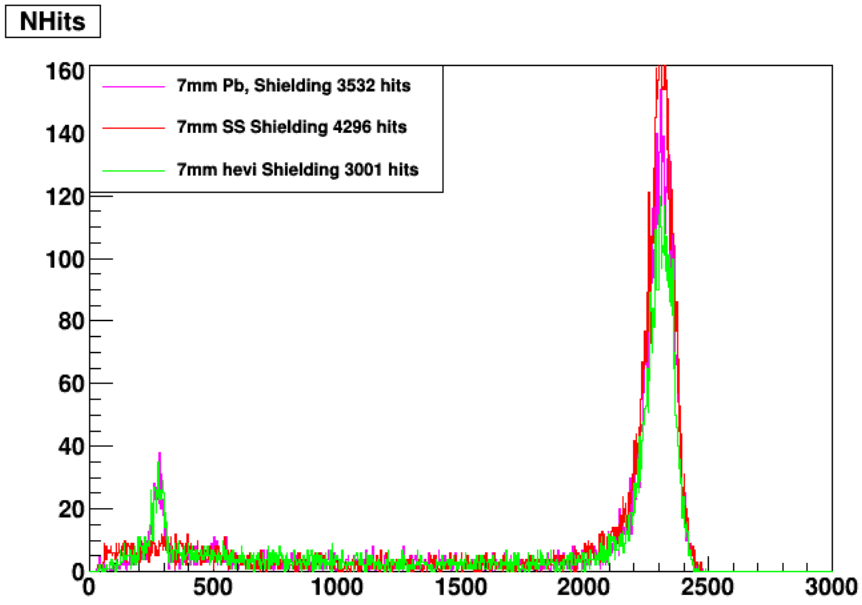

Figure B.5: The NHit distribution for 10000 4.4MeV γ events going through 7mm of lead, stainless steel and hevimet.

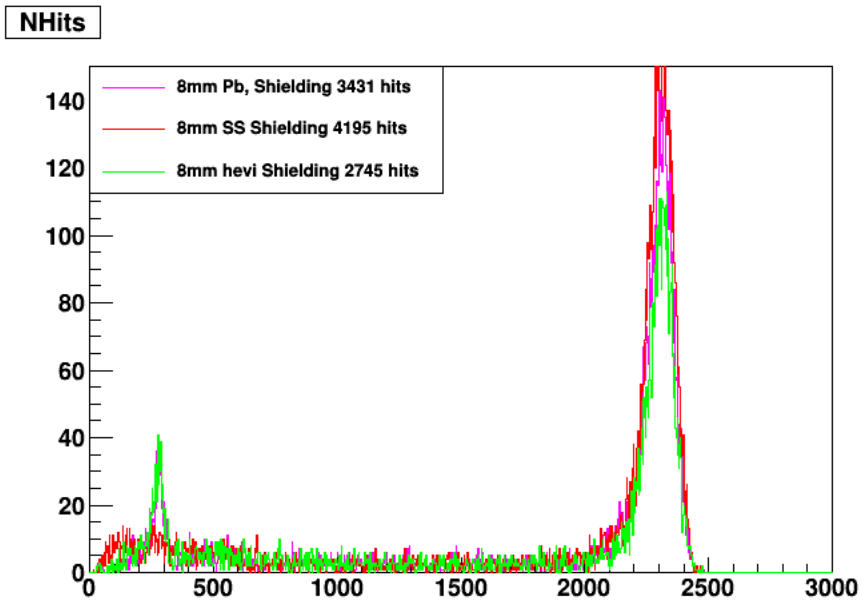

Figure B.6: The NHit distribution for 10000 4.4MeV γ events going through 8mm of lead, stainless steel and hevimet.

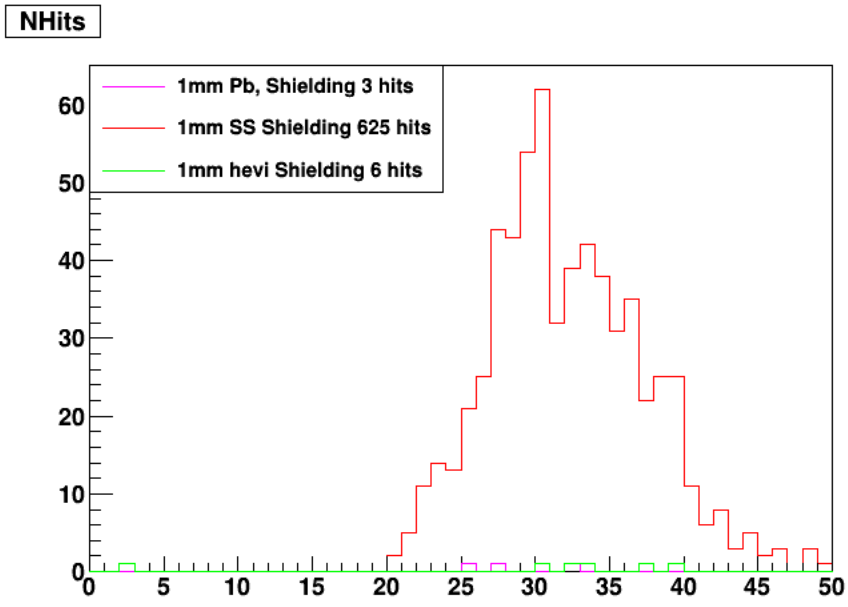

Figure B.7: The NHit distribution for 10000 59.5keV γ events going through 1mm of lead, stainless steel and hevimet.

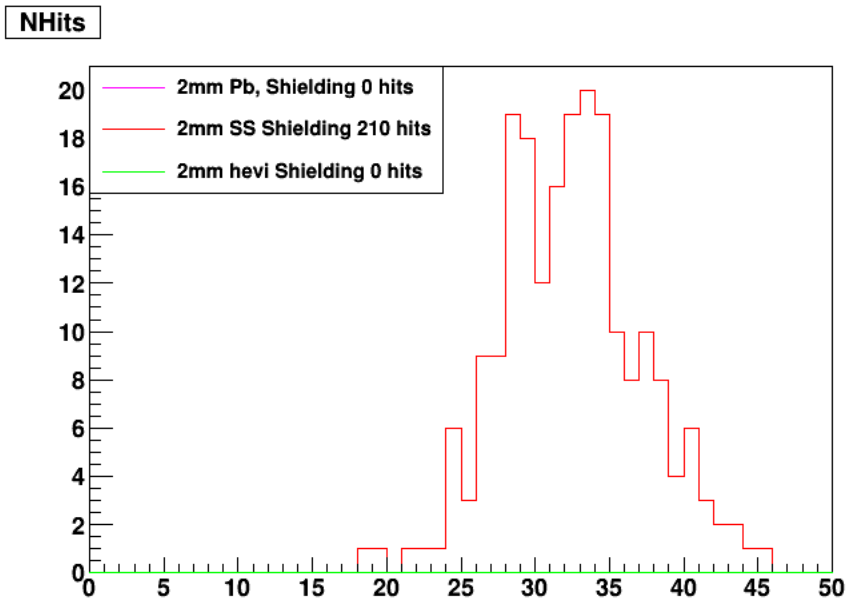

Figure B.8: The NHit distribution for 10000 59.5keV γ events going through 2mm of lead, stainless steel and hevimet.

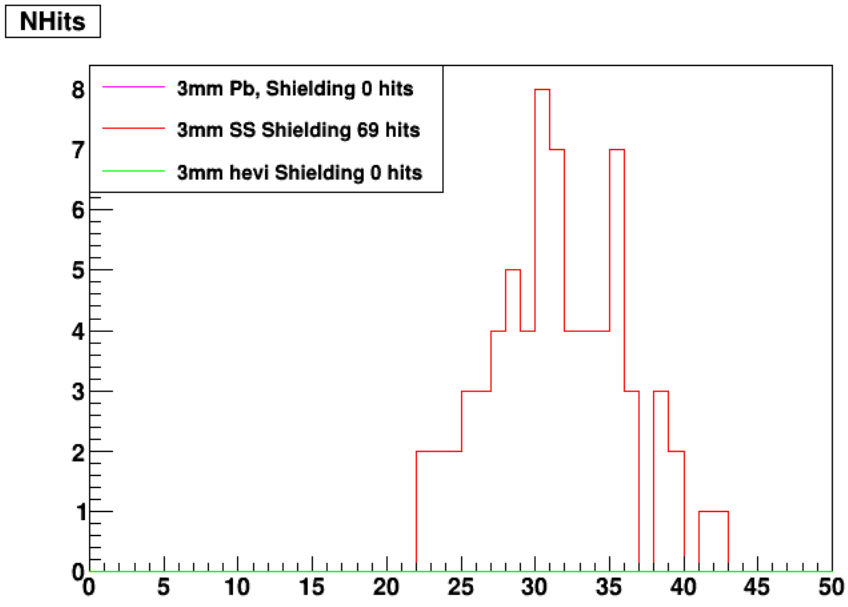

Figure B.9: The NHit distribution for 10000 59.5keV γ events going through 3mm of lead, stainless steel and hevimet.

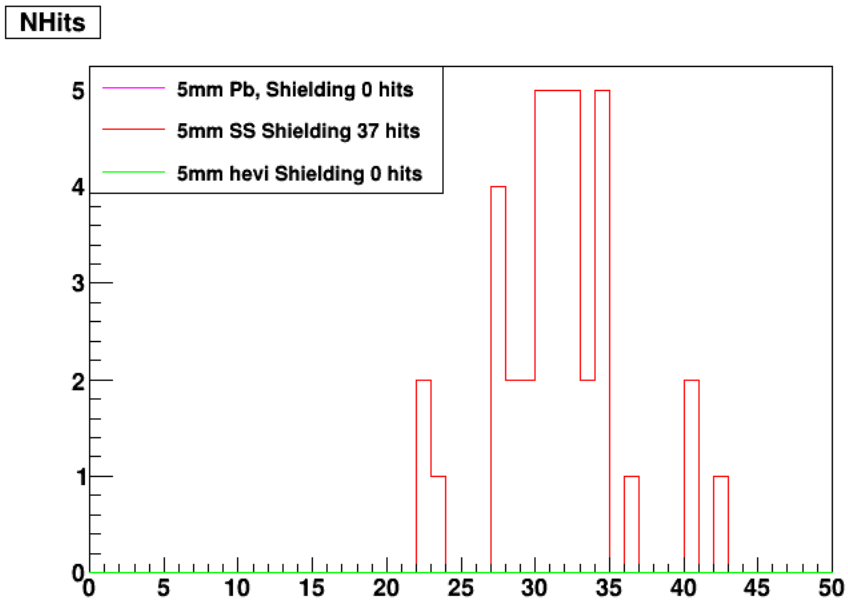

Figure B.10: The NHit distribution for 10000 59.5keV γ events going through 5mm of lead, stainless steel and hevimet.

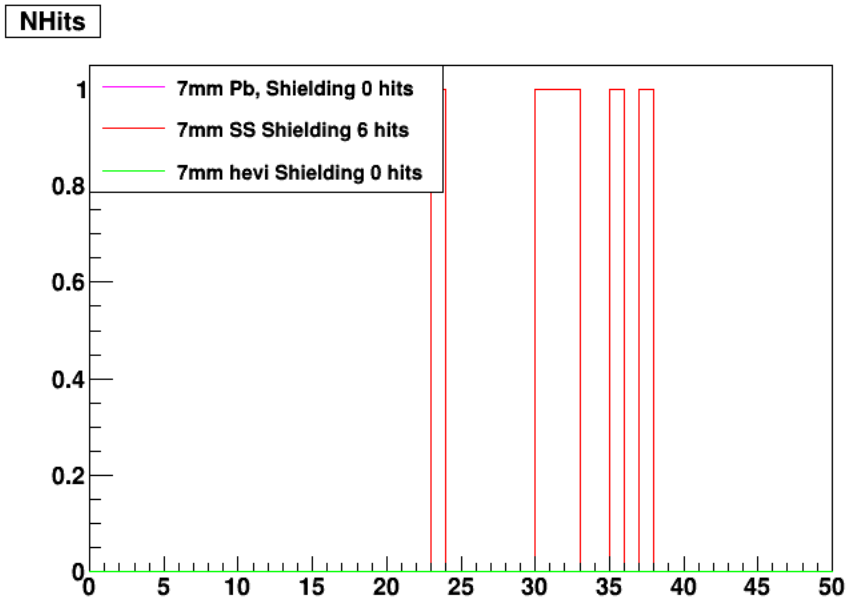

Figure B.11: The NHit distribution for 10000 59.5keV γ events going through 7mm of lead, stainless steel and hevimet.

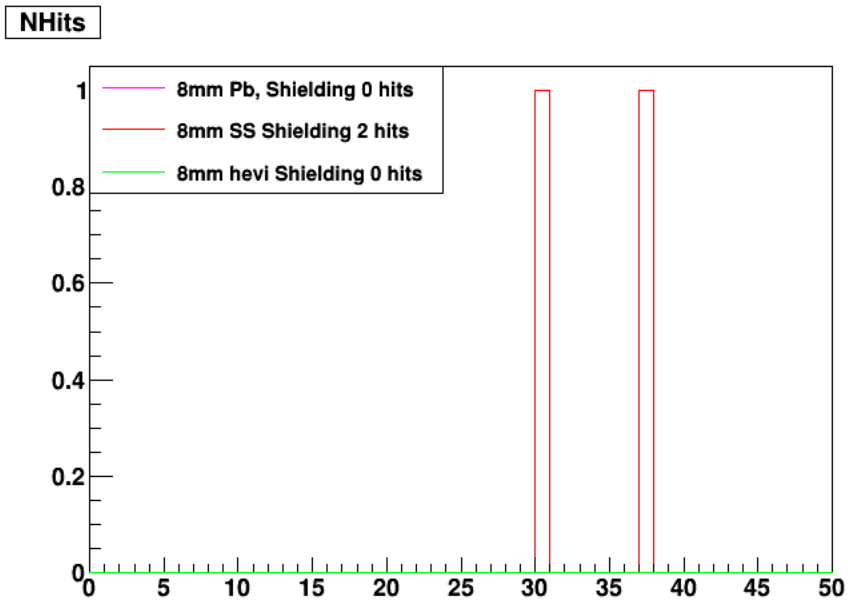

Figure B.12: The NHit distribution for 10000 59.5keV γ events going through 8mm of lead, stainless steel and hevimet.

Bibliography

[1] W. Pauli. Dear radioactive ladies and gentlemen. *Phys. Today*, 31N9:27, 1978.

[2] Fred L. Wilson. Fermi's theory of beta decay. *American Journal of Physics*, 36(12):1150–1160, 1968.

[3] C. L. Cowan, Jr., F. Reines, F. B. Harrison, H. W. Kruse, and A. D. McGuire. Detection of the Free Neutrino: A Confirmation. *Science*, 124:103–104, July 1956.

[4] The nobel prize in physics 1995. Nobelprize.org. Nobel Media AB 2014. Web. 21 Nov 2017.

[5] Frederick Reines and Clyde L Cowan. The neutrino. *Nature*, 178(4531):446–449, 1956.

[6] MissMJ. Standard model of elementary particles, 2006. By MissMJ [CC BY 3.0 (http://creativecommons.org/licenses/by/3.0) or Public domain], via Wikimedia Commons.

[7] G. Danby, J-M. Gaillard, K. Goulianos, L. M. Lederman, N. Mistry, M. Schwartz, and J. Steinberger. Observation of high-energy neutrino reactions and the existence of two kinds of neutrinos. *Phys. Rev. Lett.*, 9:36–44, Jul 1962.

[8] K. Kodama et al. Observation of tau neutrino interactions. *Phys. Lett.*, B504:218–224, 2001.

[9] Frank T. Avignone, III, Steven R. Elliott, and Jonathan Engel. Double Beta Decay, Majorana Neutrinos, and Neutrino Mass. *Rev. Mod. Phys.*, 80:481–516, 2008.

[10] M. Goeppert-Mayer. Double beta-disintegration. *Phys. Rev.*, 48:512–516, 1935.

[11] Ettore Majorana. Teoria simmetrica dell'elettrone e del positrone. *Il Nuovo Cimento (1924-1942)*, 14(4):171, 2008.

[12] W. H. Furry. On transition probabilities in double beta-disintegration. *Phys. Rev.*, 56:1184–1193, 1939.

[13] Manfred Lindner, Tommy Ohlsson, and Gerhart Seidl. Seesaw mechanisms for Dirac and Majorana neutrino masses. *Phys. Rev.*, D65:053014, 2002.

[14] S. M. Bilenky and C. Giunti. Neutrinoless Double-Beta Decay: a Probe of Physics Beyond the Standard Model. *Int. J. Mod. Phys.*, A30(04n05):1530001, 2015.

[15] B. T. Cleveland, Timothy Daily, Raymond Davis, Jr., James R. Distel, Kenneth Lande, C. K. Lee, Paul S. Wildenhain, and Jack Ullman. Measurement of the solar electron neutrino flux with the Homestake chlorine detector. *Astrophys. J.*, 496:505–526, 1998.

[16] John N Bahcall and Raymond Davis Jr. Solar neutrinos: a scientific puzzle. *Science*, 191:264–267, 1976.

[17] Kohji S Hirata, Takaaki Kajita, T Kifune, K Kihara, Masayuki Nakahata, K Nakamura, S Ohara, Y Oyama, N Sato, M Takita, et al. Observation of b 8 solar neutrinos in the kamiokande-ii detector. *Physical Review Letters*, 63(1):16, 1989.

[18] W. Hampel et al. GALLEX solar neutrino observations: Results for GALLEX III. *Phys. Lett.*, B388:384–396, 1996.

[19] John N. Bahcall. Solar models and solar neutrinos: Current status. *Phys. Scripta*, T121:46–50, 2005.

[20] B. Pontecorvo. Neutrino Experiments and the Problem of Conservation of Leptonic Charge. *Sov. Phys. JETP*, 26:984–988, 1968. [Zh. Eksp. Teor. Fiz.53,1717(1967)].

[21] Robert Ehrlich. Possible Evidence for Neutrino Oscillations in the Brookhaven Solar Neutrino Experiment. *Phys. Rev.*, D18:2323, 1978.

[22] Q. R. Ahmad and *et al* Allen. Measurement of the rate of $\nu_e + d \rightarrow p + p + e^-$ interactions produced by ^8b solar neutrinos at the sudbury neutrino observatory. *Phys. Rev. Lett.*, 87:071301, Jul 2001.

[23] B Aharmim, SN Ahmed, JF Amsbaugh, AE Anthony, J Banar, N Barros, EW Beier, A Bellerive, B Beltran, M Bergevin, et al. Independent measurement of the total active b 8 solar neutrino flux using an array of he 3 proportional counters at the sudbury neutrino observatory. *Physical Review Letters*, 101(11):111301, 2008.

[24] K Abe, Y Haga, Y Hayato, M Ikeda, K Iyogi, J Kameda, Y Kishimoto, Ll Marti, M Miura, S Moriyama, et al. Solar neutrino measurements in super-kamiokande-iv. *Physical Review D*, 94(5):052010, 2016.

[25] S. Andringa et al. Current Status and Future Prospects of the SNO+ Experiment. *Adv. High Energy Phys.*, 2016:6194250, 2016.

[26] R. N. Cahn, D. A. Dwyer, S. J. Freedman, W. C. Haxton, R. W. Kadel, Yu. G. Kolomensky, K. B. Luk, P. McDonald, G. D. Orebi Gann, and A. W. P. Poon. White Paper: Measuring the Neutrino Mass Hierarchy. In *Proceedings, 2013 Community Summer Study on the Future of U.S. Particle Physics: Snowmass on the Mississippi (CSS2013): Minneapolis, MN, USA, July 29-August 6, 2013*, 2013.

[27] P. Vogel and John F. Beacom. Angular distribution of neutron inverse beta decay, $\overline{\nu}_e + \mathrm{p} \rightarrow {}^1\mathrm{n} + \mathrm{e}^+$. *Phys. Rev.*, D60:053003, 1999.

[28] Z Djurcic, J A Detwiler, A Piepke, V R Foster, L Miller, and G Gratta. Uncertainties in the anti-neutrino production at nuclear reactors. *Journal of Physics G: Nuclear and Particle Physics*, 36(4):045002, 2009.

[29] Eugene Guillian. The Sensitivity of SNO+ to Δm^2_{12} Using Reactor Anti-neutrino Data. 2008.

[30] Shawn M Usman, Glenn R Jocher, Stephen T Dye, William F McDonough, and John G Learned. Agm2015: Antineutrino global map 2015. *Scientific reports*, 5, 2015.

[31] Yu Huang, Viacheslav Chubakov, Fabio Mantovani, Roberta L. Rudnick, and William F. McDonough. A reference earth model for the heat-producing elements and associated geoneutrino flux. *Geochemistry, Geophysics, Geosystems*, 14(6):2003–2029, 2013.

[32] G Bellini, A Ianni, L Ludhova, F Mantovani, and WF McDonough. Geo-neutrinos. *Progress in Particle and Nuclear Physics*, 73:1–34, 2013.

[33] I. V. KRIVOSHEINA. Sn 1987a — historical view about registration of the neutrino signal with baksan, kamiokande ii and imb detectors. *International Journal of Modern Physics D*, 13(10):2085–2105, 2004.

[34] Snews. http://snews.bnl.gov/ , Accessed: 2017-10-11.

[35] Billy Liggins. SNO+ Commissioning Status. In *Prospects in Neutrino Physics (NuPhys2016) London, London, United Kingdom, December 12-14, 2016*.

[36] Nobelprize.org. The 2015 nobel prize in physics - press release. 2015.

[37] Koushik Ghosh K. Mofazzal Hossain, Dipendra N. Ghosh and Tapas Saha. Application of Signal Processing to Investigate the Total Active 8B Solar Neutrino Flux Signal from Sudbury Neutrino Observatory (SNO). *International Journal of Electronic Engineering Research*, 2:303–324, 2010.

[38] A. Bialek, M. Chen, B. Cleveland, P. Gorel, A. Hallin, P.J. Harvey, J. Heise, C. Kraus, C.B. Krauss, I. Lawson, C.J. Ng, B. Pinkney, D.M. Rogowsky, L. Sibley, R. Soluk, J. Soukup, and E. Vázquez-Jáuregui. A rope-net support system for the liquid scintillator detector for the sno+ experiment. *Nuclear Instruments and Methods in Physics Research Section A: Accelerators, Spectrometers, Detectors and Associated Equipment*, 827:152 – 160, 2016.

[39] J Brack, B Delgado, J Dhooghe, J Felde, B Gookin, S Grullon, JR Klein, R Knapik, A La-Torre, S Seibert, et al. Characterization of the hamamatsu r11780 12 in. photomultiplier tube. *Nuclear Instruments and Methods in Physics Research Section A: Accelerators, Spectrometers, Detectors and Associated Equipment*, 712:162–173, 2013.

[40] T Araki, S Enomoto, K Furuno, Y Gando, K Ichimura, H Ikeda, K Inoue, Y Kishimoto, M Koga, Y Koseki, et al. Search for the invisible decay of neutrons with kamland. *Physical review letters*, 96(10):101802, 2006.

[41] SN Ahmed, AE Anthony, EW Beier, A Bellerive, SD Biller, J Boger, MG Boulay, MG Bowler, TJ Bowles, SJ Brice, et al. Constraints on nucleon decay via invisible modes from the sudbury neutrino observatory. *Physical review letters*, 92(10):102004, 2004.

[42] R. Alves et al. The calibration system for the photomultiplier array of the SNO+ experiment. *JINST*, 10(03):P03002, 2015.

[43] Alexandra Huss. Measurements of photon scattering lengths in scintillator and a test of the linearity of light yield as a function of electron energy. *Bulletin of the American Physical Society*, 58, 2013.

[44] M. Chernykh, H. Feldmeier, T. Neff, P. von Neumann-Cosel, and A. Richter. Pair decay width of the Hoyle state and carbon production in stars. *Phys. Rev. Lett.*, 105:022501, 2010.

[45] Ali Asghar Mowlavi and Rahim Koohi-Fayegh. Determination of 4.438mev γ-ray to neutron emission ratio from a 241am–9be neutron source. *Applied Radiation and Isotopes*, 60(6):959 – 962, 2004.

[46] James Chilton Loach. *Measurement of the Flux of* 8^B *Solar Neutrinos at the Sudbury Neutrino Observatory*. PhD thesis, Lincoln College, University of Oxford, 2008.

[47] S. Agostinelli, J. Allison, et al. Geant4—a simulation toolkit. *Nuclear Instruments and Methods in Physics Research Section A: Accelerators, Spectrometers, Detectors and Associated Equipment*, 506(3):250 – 303, 2003.

[48] J. Allison, K. Amako, et al. Geant4 developments and applications. *IEEE Transactions on Nuclear Science*, 53(1):270–278, Feb 2006.

[49] J. Allison, K. Amako, J. Apostolakis, et al. Recent developments in geant4. *Nuclear Instruments and Methods in Physics Research Section A: Accelerators, Spectrometers, Detectors and Associated Equipment*, 835:186 – 225, 2016.

[50] M.-M. Bé, V. Chisté, C. Dulieu, X. Mougeot, E. Browne, V. Chechev, N. Kuzmenko, F. Kondev, A. Luca, M. Galán, A.L. Nichols, A. Arinc, and X. Huang. *Table of Radionuclides*, volume 5 of *Monographie BIPM-5*. Bureau International des Poids et Mesures, Pavillon de Breteuil, F-92310 Sèvres, France, 2010.

[51] Mi-Tech Metals Inc. *Shielding Materials and Neutron Energy Spectra*. Mi-Tech Metals Inc.Indianapolis, Indiana, 2001.

[52] Nuno Barros, 2017-10-04. Personal communication.

[53] Valentina Lozza. Background summary document. Technical report, Technische Universität Dresden 01069 Dresden, Germany, 02 2017. Internal SNO+ report.